

Université catholique de Louvain
Faculté des bioingénieurs
Earth and Life institute

Towards consistent inland water body mapping across space and time from optical Earth observation systems

Raphaël d'Andrimont

Mai 2017

Thèse présentée en vue de l'obtention
du grade de docteur en sciences agronomiques
et ingénierie biologique

Promoteur: Pierre Defourny

Composition du jury:

Président:	Pr Bruno Delvaux (UCL, Belgique)
Promoteur:	Pr Pierre Defourny (UCL, Belgique)
Lecteurs:	Pr Marnik Vanclooster (UCL, Belgique)
	Dr Laurent Kergoat (GET, France)
	Dr Olivier Arino (ESA, Italie)
	Mr Chris Steenmans (EEA, Danemark)

L'Eau claire a cette Beauté alchimique
Débarrassée de tout Zézaiement
Que l'on respire dans l'Air et le Vent
Lorsqu'on sait boire l'Espace cosmique

Gérald Sédrati-Dinet

Acknowledgements

Après près de 7 ans dans les murs du Mendel, 3 bureaux, 5 ordis, 700 litres de café Puro, 600 étudiants initiés avec bienveillance à la pratique de la géomatique, une bonne cinquantaine de boarding pass, 4 continents visités, 5 projets européens FP7 (Geoland2, MOCCCASIN, ImagineS, GIO GL et SIGMA), 2 projets régions wallonnes (ORTHOWATCH et THEO) et 2 sujets de thèse, me voilà à l'accouchement de ma thèse qui fut une belle aventure semée de joies et d'embuches, et qui m'a appris énormément tant sur le monde que sur moi-même.

Avant tout, je voudrais adresser un merci particulier à Pierre, mon promoteur. Merci de m'avoir fait confiance comme chercheur et comme assistant. J'ai adoré pouvoir combiner ces deux aspects qui sont pour moi indissociables, à savoir, la recherche scientifique et la transmission des savoirs. Merci Pierre pour ton enthousiasme indéfectible, ta force de travail, ta passion et tes métaphores. Un cheminement de thèse est unique et le bateau, bien que parti des champs de blé, est arrivé à l'eau avec succès.

Je voudrais aussi remercier les membres de mon jury pour leurs précieux conseils et pour le temps qu'ils ont consacré à améliorer ce manuscrit. Merci à Bruno Delvaux d'avoir accepté d'en être président malgré les contraintes d'agenda, merci à Marnik Vanclooster pour ses conseils précieux et son apport hydrologique, merci à Laurent Kergoat pour la pertinence de ses remarques concernant la télédétection, merci à Olivier Arino de m'avoir aidé à mettre mon travail en perspective et, enfin merci à Chris Steenmans pour les précieux conseils pour améliorer ce manuscrit.

Je voudrais ensuite remercier mes collègues au sein du groupe de recherche ENGE qui ont partagé mon quotidien tout au long de ces années. Quel plaisir d'être parmi des gens inspirants et motivés, toujours partants pour partager des discussions scientifiques palpitantes.

Merci aux chercheurs qui sont déjà partis. En particulier, ceux de mon premier bureau avec qui je garde des souvenirs incroyables : Greg (What the hell is in a pixel ?), Astrid (avec qui on a appris à dompter le serpent), Céline E. (pout ton immense rire communicatif) et Sophie (quand tu veux pour une nuit blanche pour un futur launch !). Merci à JPK (pour ces casques bleus dont on s'est occupés dans la nuit avant de passer ton permis), merci à Amaury (pour son hyper gentillesse et kinésie). Merci à Aline (pour les ragots qui nous manquent), à Emilie, Yannick, Nico M., Manu (toujours disponible pour aider),

Agung, Antoine L., Ol Ska, Céline D., Kevin, Alexandre, Mayo, Christophe, Quentin, Renaud, Nico N. et tous les autres.

Merci aussi à ceux qui sont toujours mes collègues. Merci à Patrick et Emmanuel, les ACA, pour les contributions tant sociales que scientifiques. Merci à Pascale, Marie-Christine et Aurélie sans qui le labo et l'institut de ne pourraient pas tourner. Merci à Éric, maître Yoda de tout apprenti geek en puissance. Merci Thomas d'être toujours disponible malgré tes attributions multi-thread. Merci à Julien, mon assistant qui m'a initié, merci pour ton immense compétence, ta disponibilité et d'être le garant des traditions ENGE. Merci à Doriane (pour les papotes de fin de thèse), merci à Inès (pour les tuyaux de fin de thèse), merci à Cindy (vive le LAI), merci à Xbox (pour l'initiation au macchiato et au SAR qui se fait toujours attendre). Merci à Céline L. pour les innombrables discussions tant scientifiques que fondamentales. Merci pour notre collaboration « validation », j'ai appris beaucoup de choses. C'est un plaisir de travailler avec toi. Merci à Catherine d'être si humaine, merci pour notre super travail d'équipe sur les plans d'eau wallons. Merci à Guillaume pour son activisme. Merci à maman MJ qui pense toujours à tout et à tous, à Flo pour ses blagues qui sont pires (mieux ?) que les miennes. Merci à Julie (pour ton peps, pour notre collaboration hyperspectrale et pour ta patience face à mes disponibilités limitées). Merci à Nico B. (pour le café matinal). Merci aux équipes sportives ENGE pour nos incroyables matchs (foot, volley et badminton) même si j'en étais absent ces derniers temps.

Je voudrais aussi remercier très spécialement les deux énergumènes avec qui je partage mon bureau, les Globcroppers : François et Damien. La pendaison de bureau avait donné le *la*, la suite n'a été que montées en octaves tant humaines qu'intellectuelles. Aucun wall of sh(f)ame n'est suffisant pour décrire cet incubateur d'idées, de travails, de conneries, d'ambitions, mais aussi de réalisations bien concrètes et tangibles qui ont fait de nous, entre autres, des NASA galactic problem solvers, des hackers de malade, des disciples de shiva, des entrepreneurs, des imposteurs, des passionnés de sciences, des challengers du D4D qui raflent des prix au MIT, des blogueurs guru-gis, mais surtout, au final, des amis. Merci les b***ouilles! Des nouveaux challenges nous attendent tous les trois, mais RDV est déjà pris pour notre futur défi commun car l'aventure des globcroppers n'est pas terminée!

Je voudrais aussi souligner que durant cette thèse, j'ai eu l'occasion de faire de nombreuses collaborations scientifiques. Que ce soit lors de séjour à l'étranger comme à l'INRA à Avignon, chez Fred Baret et Marie Weiss, que je voudrais remercier pour l'accueil et l'initiation aux réseaux de neurones ainsi qu'à l'ascension cycliste du mont Ventoux, ou encore, à Moscou, avec Allard de Wit où nous avons pu organiser une incroyable campagne de terrain de trois ans. Enfin, je remercie les chercheurs du labo pour les collaborations scientifiques internes comme, par exemple, pour le papier S2 qui contribue d'ailleurs à ce manuscrit.

Merci à Céline L., François S. et Gaetan B. pour les années de covoiturage. On s'est bien marré!

Je voudrais aussi remercier la faculté et tout son staff pour leur travail formidable. Je voudrais aussi remercier tous les étudiants qui ont dû me subir et

qui m'ont tellement appris. Merci à tous les assistants pour toute cette énergie qui fait vivre la faculté Agro et aussi pour l'énergie déployée dans nos activités au sein de l'A-cube. Un merci spécial à Nico F., frère d'arme, à François C., Jolan, JB, Sarah et Antoine avec qui j'ai partagé certains cours.

Je voudrais aussi remercier mes amis toujours à mes côtés pendant cette aventure. D'abord les cramos, qui, comme Parker Lewis, ne perdent jamais! Merci à mich, mon fidèle ami (nous sommes fidèles, et vous ?), à Fredo (le coach), à Bougon (pour l'écoute, 1160 Forever!), à Gigs (le chevalier du grand Nord), à Raphiot (le GO) et à PN (qui propose de relire mes articles, il est fou !). Merci spécial aussi à Oli pour les thesis trips sur les mobile phone data. Je voudrais aussi remercier mes amis de la quinzième (Baghé, Raph, Palo et le malgache) toujours partants pour des défis sportifs, que ce soit le tour du lac express à midi, les crêtes de Spa ou un marathon à Amsterdam. Sans oublier, le BUHC, mon éminente équipe de hockey que je quitte au sommet de sa gloire, de sa forme sportive et festive! Je voudrais aussi remercier la famille Buko, mes voiz', pour leur amitié au fil des années. Un clin d'œil particulier pour Kik et Elo pour l'initiation aux neurosciences et les discussions de thésards for the sake of Science!

Je voudrais aussi remercier ma géniale belle-famille pour leur soutien dans ma quête, tant moral que logistique : Non(n)a, Don Bruno, Pauline (PRL), Alex et Nouch. Merci aussi à mon frère et ma sœur que j'adore et qui rigolent bien en m'imaginant donnant cours comme un marchand de tapis. Merci spécial à vous, papa et maman, de m'avoir permis d'étudier, de m'avoir transmis l'amour du travail et de la rigueur, ainsi que la passion. Merci aussi de m'avoir toujours soutenu et de continuer à me soutenir dans mes projets. Un merci aussi pour mes grand-mères et le reste de ma famille.

Enfin, s'il y a une personne que je voudrais remercier en particulier, c'est toi Lolo. Merci d'avoir cru en moi, de m'avoir soutenu, de m'avoir coaché, d'avoir participé à cette thèse par tes relectures et suggestions. Quelle chance j'ai de pouvoir passer tous ces moments avec une magnifique jeune femme pétillante d'intelligence et d'idées. Merci pour ces centaines d'heures de discussions scientifiques passionnantes, merci pour tous les projets incroyables déjà réalisés et tous ceux qui arrivent. Fruits de cet amour, je voudrais exprimer mon immense amour à mes deux petites chéries, Lily et Zoé, qui nous ont rejoints au cours de cette thèse. Leurs émerveillements, leurs incroyables curiosités, leurs absences de préjugés m'inspirent quotidiennement dans ma démarche scientifique. J'espère que cette thèse contribuera (très modestement) à offrir un monde plus durable dans lequel vous pourrez grandir et vous épanouir.

Louvain-la-Neuve, Avril 2017

Contents

Acknowledgements . . . iii
Table of Content . . . vii
List of Figures . . . xi
List of Tables . . . xiii
List of Acronyms . . . xv

Introduction **1**
Mapping inland water is crucial to monitor global dynamic processes . 1
National and international initiatives . . . 3
Mapping water bodies with remote sensing . . . 3
Water detection from passive remote sensing . . . 4
Water detection from active remote sensing . . . 7
Optical sensors suited for inland water mapping . . . 8
Limitations of optical remote sensing for inland water mapping 10
Scale issues . . . 13

Scope and objectives **15**
Novelty and outline of the thesis . . . 17

1 Sub-metric water detection handling data heterogeneity **21**
1.1 Introduction . . . 22
1.2 Conceptual framework . . . 25
1.3 Study area . . . 28
1.3.1 Study region . . . 28
1.3.2 Historical water body vector map . . . 30
1.4 Framework application . . . 30
1.4.1 Mapping observation conditions and dataset heterogeneity 31
1.4.2 Decreasing local target feature heterogeneity . . . 35
1.4.3 Classification and signal processing . . . 38
1.4.4 Combination and map update . . . 40
1.4.5 Validation . . . 42
1.5 Results . . . 43
1.5.1 Mapping observation conditions: homogeneous groupings of data acquisition . . . 43
1.5.2 Local heterogeneity removal . . . 46
1.5.3 Handling intrinsic variability of the target . . . 47
1.5.4 Combinations and update of the water body map . . . 50

1.5.5 Quality evaluation 51
1.6 Discussion 54
1.7 Conclusions 58

2 Water body sub-decametric detection potential of Sentinel-2 59
2.1 Introduction 60
2.2 Methodology and study area 62
2.3 Results 68
2.3.1 On the spectral resolution 68
2.3.2 On the spatial resolution 69
2.3.3 On the potential for object detection 70
2.4 Application of Sentinel-2 potential to detect small water bodies . 71
2.4.1 Method 71
2.4.2 Results 71
2.5 Discussion 75

3 Sub-kilometric water body monitoring from twice-daily observation 77
3.1 Introduction 78
3.2 Data and study area 80
3.3 Methodology 80
3.3.1 Water detection 80
3.3.2 Temporal analysis 82
3.3.3 Quality assessment of the temporal analysis 85
3.4 Results 88
3.4.1 Valid data availability for water body detection 88
3.4.2 Temporal analysis 89
3.4.3 Quality assessment of the temporal analysis 92
3.5 Discussion 95
3.6 Conclusions 98

4 Validation of a 150-m permanent inland water global map 99
4.1 Introduction 100
4.2 Methodology 105
4.2.1 Sampling scheme 105
4.2.2 Generation of the validation database 106
4.2.3 Accuracy assessment 106
4.3 Results 108
4.4 Discussion 110
4.4.1 Confidence-based stratification 110
4.4.2 Permanent versus temporary water bodies 112
4.5 Conclusions 112

Conclusions and perspectives 115
Synthesis 115
Perspectives 121
Data availability and usability 121
Improving synergies 121

Scientific communities 122
Seasonal water validation 123
New processing capacities 123
Towards operational applications 124
Epilogue 124

References **127**

List of publications **151**

List of Figures

1 Wavelength ranges 4
2 Absorption characteristics of pure water 5
3 Sun to sensor radiation paths 6
4 Water body diversity 11

5 Spatial and temporal resolutions of the 4 chapters 17
6 Spatial extent relevance of the 4 chapters 18

1.1 Conceptual framework to handle the heterogeneity 27
1.2 Different origins and types of water bodies 29
1.3 Historical water body vector map 30
1.4 Aerial acquisition date, camera, time and sun vertical angle . . 32
1.5 LiDAR acquisition 33
1.6 LiDAR LAS 34
1.7 Trimming labelling data 37
1.8 Combination of the two data sources 41
1.9 Validation dataset 42
1.10 Spatial stratification for the aerial photos 44
1.11 Effects of the camera, the date and the time of acquisitions . . 45
1.12 Shadow estimation 46
1.13 Drawing of the validation random sampling 47
1.14 Classification results of the aerial photos 48
1.15 Retrieval of water bodies from LiDAR 49
1.16 Results of the method combination 50
1.17 Illustration of the method performance 53
1.18 Boxplot of the red, green, blue, near infrared, NDVI and NDWI values 55

2.1 Snapshots of an orthophoto (25 cm), Sentinel-2A (10 m), SPOT-5 (Take 5) (10 m) and Landsat-8 (30 m) 63
2.2 Edge spread function 66
2.3 Line spread function estimates 67
2.4 Shapes of interest: linear center, linear border and center . . . 68
2.5 Discriminating power of spectral bands and indices 69
2.6 Sentinel-2 image classification success rate 72
2.7 Effect of the PSF on three types of water bodies 74

3.1 Building water thematic indicators 83
3.2 Distribution of 500 points randomly drawn 86
3.3 Valid observations over a year from MODIS instruments 88
3.4 Annual Water Occurrence 89
3.5 Intra-annual water variation examples 90
3.6 Mean Annual Occurrence 91
3.7 Permanent water body map 92

4.1 The CCI global map of open water bodies 103
4.2 Complementarities of the constitutive sources of the CCI WB 104
4.3 Global permanent water maps assessment 105
4.4 Location of the 2110 samples 109

List of Tables

1 Water detection indices from visible, NIR and SWIR channels . 6
2 Optical sensors mentioned in the thesis 9

1.1 Statistics of the strata and the clusters 48
1.2 LiDAR processing sequences 50
1.3 Detection efficiency and detection cost 52

2.1 Sentinel-2 MSI, Landsat-8 OLI and SPOT-5 HRG band specifications 61
2.2 Full width half maximum values (FWHM) and signal-to-noise ratio (SNR) 70
2.3 Minimum water body width (m) detectable 70

3.1 Commission error of water maximum extent 92
3.2 Discrepancy matrix between the *permanent water body map* and MOD44W 93
3.3 Comparison of water body monitoring by SPOT-VGT SWB and MODIS-based products 94
3.4 Water surface distribution according their persistence for each Köppen-Geiger climate class 95

4.1 Available global or near-global water body products 101
4.2 Mathematical formulation of the error matrix. 107
4.3 Accuracy estimates 109
4.4 Accuracy results for the error-prone stratum 110
4.5 Probability to sample correctly and incorrectly 111

4.6 Thesis results summary 116

List of Acronyms

ACF	Action Contre la Faim
ASAR	Envisat Advanced SAR
CAP	Common Agricultural Policy
CCI	Climate Change Initiative
CDOM	Colored Dissolved Organic Matter
CEOS	Committee on Earth Observation Satellites
CGIAR	Consortium of International Agricultural Research Centers
DIAS	Data and Information Access Services Operations
DSM	Digital Surface Model
DTM	Digital Terrain Model
ECV	Essential Climate Variables
EO	Earth Observation
ESA	European Space Agency
ESF	Edge Spread Function
EU	European Union
ESDR	Earth Science Data Record
FAO	Food and Agriculture Organization
FWHM	Full Width Half Maximum
G3WBM	Global 3-second Water Body Map
GCOS	Global Climate Observing System
GEO	Group on Earth Observation
GEOSS	Global Earth Observation System of Systems
GFC	Global Forest Change
GIS	Geographic Information System
GIO WB	GMES Initial Operations (Copernicus) Water Body
GIW	Global Inland Water
GLS	Global Land Survey
GLOWABO	GLObal WAter BOdies database
GLWD	Global Lakes and Wetlands Database
GMES	Global Monitoring for Environment and Security
GSD	Ground Sampling Distance
HR	High Resolution
HRG	High Resolution Geometric
HSV	Hue Saturation Value

H-V	Hue-Value
IPCC	Intergovernmental Panel on Climate Change
LAI	Leaf Area Index
LAS	LASer file format exchange
LC	Land Cover
LCCS	Land Cover Classification System
LiDAR	Light Detection And Ranging
LP DAAC	Land Processes Distributed Active Archive Center
LST	Land Surface Temperature
LU	Land Use
MNDWI	Modified Normalized Difference Water Index
MOD44W	MODIS 250 m land-water mask
MODIS	Moderate Resolution Imaging Spectroradiometer
MR	Medium Resolution
MSI	MultiSpectral Imager
MTG	Meteosat Third Generation
NDPI	Normalized Difference Pond Index
NDVI	Normalised Difference Vegetation Index
NDWI	Normalized Water Index
NHI	Normalized Humidity Index
NIR	Near-InfraRed
NRT	Near Real Time
OA	Overall Accuracy
OAD	Overall Allocation Disagreement
OLI	Operational Land Imager
OQD	Overall Quantity Disagreement
OTB	Orféo ToolBox
PA	Producer Accuracy
ppm	parts per million
PSF	Point Spread Function
RGB	Red, Green, Blue
RMSE	Root-Mean-Square Error
SAR	Synthetic Aperture Radar
SAR-WBI	SAR-based WB Indicator
SD	Standard Deviation
SDG	Sustainable Development Goals
SEEA	System of Environmental-Economic Accounting
SNR	Signal-to-Noise Ratio
SPOT	Satellite Pour l'Observation de la Terre
SRTM	Shuttle Radar Topography Mission
SWB	Small Water Body
SWBD	Shuttle Radar Topography Mission Water Body Dataset
SWIR	Short-Wave InfraRed
SWOT	Surface Water Ocean Topography
SZA	Sun Zenithal Angle
TDS	Total Dissolved Solids

TIRS	Thermal Infrared Sensor
TSWB	Temporal Small Water Bodies
UA	User Accuracy
UAV	Unmanned Aerial Vehicle
UNDP	United Nations Development Programme
UNFCCC	United Nations Framework Convention on Climate Change
VGT	Vegetation
VHR	Very High Resolution
VIS	Visible
VRT	Virtual GDAL dataset
VZA	View Zenithal Angle
WB	Water Body
WSM	Wide Swath Mode

Introduction

Mapping inland water is crucial to monitor global dynamic processes

Although inland waters represent less than 4% of the Earth surface, their mappings are crucial as they are affected by climate and human activity and conversely, they affect many global dynamic processes including biogeochemical cycles, biodiversity support, climate change and economical services. Water body is considered as a land cover by the remote sensing community. The term includes running waters like rivers, streams or canals as well as standing water such as oceans, seas, lakes, reservoirs, ponds, swamps, wetlands or even snow and ice fields. Inland waters refer to water bodies embedded in terrestrial areas, thus obviously excluding oceans and seas. As coastal areas are bordering lands, they are included in the inland surface waters. This section reviews the crucial importance of mapping inland waters from a scientific and social perspective.

Carbon and nutrient cycles. Inland water is recognized as a carbon source and plays an important role in natural and anthropogenic greenhouse gas budgets (Raymond *et al.*, 2013). Many studies have shown the importance of mapping water bodies to quantify global carbon fluxes. Tranvik *et al.* (2009) show that the magnitude of CO_2 emissions from inland waters equals the CO_2 uptake by the oceans and Borges *et al.* (2015) highlight the importance of including wetlands and inland waters in the global carbon budget. Holgerson and Raymond (2016) bring to light the large contribution from very small ponds of less than 0.001 km^2 to inland water CO_2 and CH_4 emissions. As the global distribution of those very small ponds is uncertain because of the difficulty to map them globally, they are excluded from carbon budget. However, CO_2 and CH_4 concentrations were found greatest in small ponds and decreased with increasing lake size. In another study, Marton *et al.* (2015) show the importance of geographically isolated ponds in the biogeochemical equilibrium. Additionally, ponds play an important role in nitrogen attenuation in agricultural landscape (Hefting *et al.*, 2013). In the other hand, denitrification, which occurs in oxygenated water, produces NO_2 which is also a greenhouse gas.

To conclude, inland waters such as lakes, wetlands and small and isolated ponds are playing a key, but complex, role in both the carbon and the nutrient cycle. Their adequate mapping is thus critical.

Biodiversity. Fresh waters are experiencing declines in biodiversity far greater than those in the most affected terrestrial ecosystems (Sala *et al.*, 2000). Collen *et al.* (2014) confirmed that there is a higher risk of extinction for freshwater species than for terrestrial. If trends in human demands for water remain unaltered and species losses continue at current rates, the opportunity to conserve much of the remaining biodiversity in fresh water will vanish (Dudgeon *et al.*, 2006). Various threats are dramatically and rapidly affecting the rich biodiversity of inland waters (Brönmark and Hansson, 2002) thus reinforcing the need for close monitoring of inland surfaces. Water body mapping is particularly important as they structure the ecological network. In particular, normally free of reproducing fish populations, very small water bodies are capital breeding habitats for numerous amphibians and reptiles adapted to reproduction in fishless habitats (Wu *et al.*, 2014).

Climate change and floods. The Intergovernmental Panel on Climate Change (IPCC) Working Group 2 (Jiménez Cisneros *et al.*, 2014) summarizes scientific evidences for adaptation, climate change impacts and vulnerability linked to water. Inland waters are affected by climate change. Lakes and reservoirs' contribution to the global carbon cycle has significantly changed because of human activities, and they will continue to change in response to future climate change causing modification in lake abundance (Tranvik *et al.* (2009).

Global flood risk will increase in the future partly due to climate change (Jiménez Cisneros *et al.*, 2014). Milly *et al.* (2002) investigated the flood risk change in a changing climate and conclude in a statistically significant positive trend in risk of great floods consistent with results from climate model. In an other study, Oki and Kanae (2006) demonstrated that the water cycle acceleration caused by climate change will result in changes in seasonal patterns and in the increasing probability of extreme events including floods and droughts.

Moreover, Subin *et al.* (2012) demonstrate that better lake characterization could improve general climate circulation model.

In conclusion, long term systematically mapping of inland waters and floods are needed to better understand the effects of climate change locally and globally along with their associate feedback to climate.

Economical resources Humans benefit from various ecosystem services offered by inland water bodies (Carpenter *et al.*, 2011). Water extraction serves for drinking water, irrigation and watering livestock. Moreover, water bodies are used for energy production, transportation, fishery and recreational purpose which make them particularly important to monitor (Vörösmarty *et al.*, 2010; Stendera *et al.*, 2012; Carvalho *et al.*, 2013).

Water mask for remote sensing and meteorologists. Global water bodies mapping is also important for remote sensing itself and its related disciplines as global water masks are used in various algorithms to retrieve biophysical variables and to correct the acquisition atmospherically in particular aerosols loading. Accurate depiction of the land and water is critical for the production

of land surface variables from remote sensing data (Carroll *et al.*, 2009) such as cloud mask (Frey *et al.*, 2008), land surface temperature (Wan *et al.*, 2002), active fires (Justice *et al.*, 2002), surface reflectance (Vermote *et al.*, 2002), and Leaf Area Index (LAI) (Chen, 1999). In a similar way, accurate mapping of the water bodies is relevant for meteorologists as it is used to improve weather forecast including the evaporation estimation.

National and international inland surface water mapping directives and initiatives

Many national and international directives such as the European Union Water Framework Directive, the US Clean Water Act, the South African National Water Act, the Australia and New Zealand Water Act, the Canada Water Act aim to improve water quality by identifying stressors and by implementing sustainable management strategies and are supported by monitoring. In addition, the Sustainable Development Goals (SDG) from United Nations Development Programme (UNDP) acknowledge water as a key issue in the fight to end poverty. Goal 6 calls for universal access to safe water by 2030. Part of this includes a focus on preserving our freshwater resources. However, remote sensing, despite its synoptic capacity and cost effective potential is often underused (Dörnhöfer and Oppelt, 2016).

Although current satellite remote sensing techniques can produce seamless global land cover maps and distinguish many terrestrial environments, they still struggle to generate accurate high-spatial resolution* representations of surface water extent (Prigent *et al.*, 2015). However, recently a lot of international, national and regional directives, projects and initiatives are focusing on inland surface water. The area of water bodies is also identified as an Essential Climate Variable (ECV) by the Global Climate Observing System (GCOS).

Additionally and specific to remote sensing, the Group on Earth Observation (GEO) coordinates the actions to establish the Global Earth Observation System of Systems (GEOSS) which identified water as a key social benefits. Moreover, the Committee on Earth Observation Satellites (CEOS) ensuring international coordination of civil space-based Earth observation programs has its own water components.

Mapping water bodies with remote sensing

Mapping inland water is quite important to scientists and policy makers. Whereas conventional mapping approaches tend to be limited in terms of spatial coverage and temporal frequency, airborne and satellite remote sensing has shown the potential to provide an invaluable complementary source of data at local to global scales (Alsdorf and Lettenmaier, 2003; Alsdorf *et al.*, 2007; Famiglietti *et al.*, 2015). Furthermore, as sensors, methodologies, data availability and the network of researchers and engaged stakeholders in this

**Spatial resolution* is a term that can lead to confusion. The common meaning in this thesis is, namely the spacing between pixel samples on the earth's surface.

field develop, increasingly widespread use of remote sensing for operational monitoring of inland waters can be envisaged (Palmer *et al.*, 2015).

Beside surface delineation, remote sensing can assist various disciplines providing indicators or variables on water bodies such as variables specific to rivers: turbidity, depth, in-stream habitats, substrate size, algae and wood (Marcus and Fonstad (2008)) or for lakes: water transparency, biota, hydrology, temperature and ice phenology (Dörnhöfer and Oppelt (2016)).

Remote sensing is the acquisition of information about an object or phenomenon without making physical contact with the object and makes use of the electromagnetic spectrum. There are two types of remote sensing: passive and active. Passive remote sensing such as a camera or radiometer detects natural radiation that is reflected or emitted by the object or its surrounding, with sunlight being the most common source of this natural radiation. Active remote sensors such as Light Detection And Ranging (LiDAR), Synthetic Aperture Radar (SAR), Altimeter and sonar emit their own source of radiation to scan an object and utilize the reflected energy or backscatter from the object to obtain the desired measurement. Remote sensing instrumentation used to gain information about the surface water operates at frequencies from tens of kHz, in the case of sonar, to optical, infrared, and microwave frequencies (Shuchman and Leshkevich, 2013). The remote sensors can be deployed on land, ship or autonomous underwater vehicle, manned and unmanned aircraft, and satellite-based platforms.

This thesis will focus on remote sensing to delineate surface waters and propose method using mainly aircraft and satellite optical remote sensing sensors, *i.e.* acquiring in the visible, in the near-infrared (NIR) and in the short-wave infrared (SWIR) domain. However, other wavelength (Figure 1) and sensor types could be used for water mapping and will thus be briefly described hereafter.

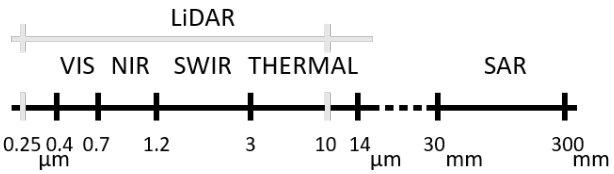

Figure 1: Wavelength ranges suited for water remote sensing.

Water detection from passive remote sensing

Visible ($0.4 - 0.7\mu m$), NIR ($0.7 - 1.2\mu m$) and SWIR ($1.2 - 3\mu m$)

In this section, the water optical properties will first be described. Afterwards the different radiation paths from sun to sensor will be depicted. Finally, the main principles used to map water in those wavelength with passive sensors are described.

The absorptance of water at the surface increases with wavelength starting with a minimum absorptance at 420 nm (Figure 2) reaching its maximum (90%) in the infrared portion of the spectrum (McCloy, 2005). Pure water thus reflects about 10% or less in the Blue (B) and Green (G) range as the absorptance is weaker, a smaller percentage in the Red (R) and certainly no energy in the infrared range (Richards, 2013). However, the water of inland surface is rarely pure and reflectance increases with the chlorophyll and suspended soil sediment content. The energy absorbed by suspended particles further depends on the density of the particles and the depth of the particle layer. Additionally, the surface roughness of water is another physical property of the water body having a major impact on the reflectance. The surface roughness corresponds to the deviations of the surface in the direction of the normal vector of an ideal flat surface. In conclusion, the content of water and the surface roughness are the major drivers for water optical properties.

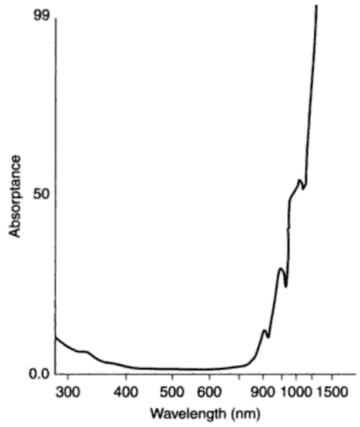

Figure 2: Absorption characteristics of pure water. Most of the light is absorbed by water from the infrared part of the spectrum (McCloy (2005)).

In addition, many interactions between sunlight and optically active substances in the water and the atmosphere influence the remotely sensed signal over a water body. Most of these interactions involve scattering and absorption processes, although fluorescence and reflectance (by macrophytes or the substrate) may play a role (Laanen, 2007). The radiance reaching a passive remote sensing detector can follow a number of routes described at Figure 3: (i) Absorption and scattering by substances in the water, (ii) Reflection by the air-water interface, (iii) Reflection by the lake bottom and (iv) Absorption and scattering by substances in the atmosphere.

As the water absorptance is maximum in the infrared, the NIR and SWIR channels are thus the most used for water detection. Commonly used methods are based on index combining bands from visible (R and G) and NIR/SWIR. The most used indices for water delineation are $NDVI$, $NDWI_1$, $NDWI_2$, NHI and $NDPI$ and are summarized in the Table 1. The bands used are the

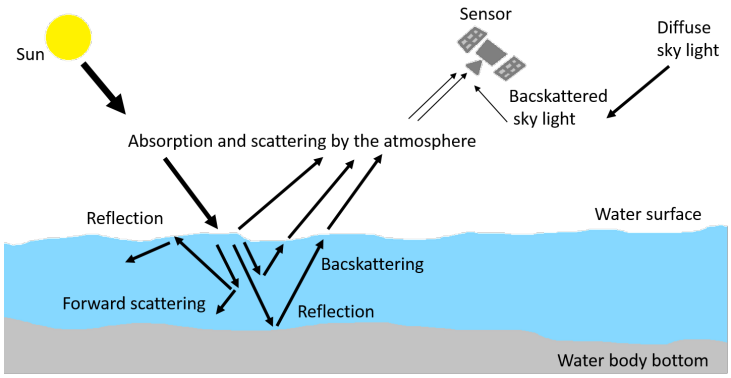

Figure 3: Sun to sensor radiation paths involve multiple scatterings and reflections determined by physical and chemical compositions of water and atmosphere along the paths.

G (560 μm), the R (665 μm), the NIR (842 μm) and the SWIR (1610 μm). The water detection is then obtained by thresholding the chosen index.

Table 1: Most used water detection indices from visible R (665 μm) and G (560 μm), NIR (842 μm) and SWIR (1610 μm) channels with their band ratios and references.

Indices	Band ratios	References
$NDVI$ = Normalized Difference Vegetation Index	$(NIR - R)/(NIR + R)$	Tucker (1979), Townshend and Justice (1986)
$NDWI_1$ = Normalized Difference Water Index	$(NIR - SWIR)/(NIR + SWIR)$	Gao (1996), Hardisky *et al.* (1983)
$NDWI_2$= Normalized Difference Water Index	$(G - NIR)/(G + NIR)$	McFeeters (1996)
$MNDWI$= Modified Normalized Difference Water Index	$(G - SWIR)/(G + SWIR)$	Xu (2006)
NHI = Normalized Humidity Index, $NDPI$ = Normalized Difference Pond Index	$(SWIR - G)/(SWIR + G)$	Clandillon *et al.* (1995), Lacaux *et al.* (2007)

The choice of the appropriate threshold could be tricky because of three major issues (Crétaux *et al.*, 2016): (1) band ratios are calculated from spectral bands which have different values for the same features according to the sensor bandwith, (2) the optical properties of the surface vary in time due to the sun-target satellite geometry, atmospheric and soil conditions, water turbidity, sediment load and sensor degradation, (3) the band ratio threshold varies depending on the sub-pixel water components. Several of these caveats are discussed in the thesis as well as the indices suited for water detection.

Thermal sensors ($3 - 14\mu m$)

In thermal imagery, there are two interesting ranges for water: 3.4-4.2 μm and 8-13.3 μm (McCloy, 2005). Changes in tone in a thermal image are due to variations in the temperature, emissivity and roughness of a surface. Beside of the artifacts linked to this three variables, water mapping by thermal imagery use the thermal inertia difference between water and soil, and between the night and the day. Thermal imagery was used for pollution mapping such as thermal discharge into water bodies, seasonal changes over ocean to study climate phenomenon such as El Niño or emitted energy from algae and for delineating lakes (Ritchie *et al.* (2003).

Water detection from active remote sensing

Light Detection And Ranging (LiDAR) ($0.25 - 10\mu m$)

Standard LiDAR sensors emit laser pulses which are mostly absorbed by the water and hence are scattered and reflected at the water surface. Most of the energy is absorbed in the water column or reflected specularly away from the field of view of the receiver (Hofle *et al.*, 2009). High-resolution LiDAR was already used to delineate water bodies in different studies (Lichvar *et al.*, 2006; Brzank and Heipke, 2006; Hofle *et al.*, 2009). LiDAR data can facilitate the detection of wetlands that are normally difficult to identify with passive sensors, such as vernal (*i.e.* temporary) pools (Wu *et al.*, 2014).

Synthetic Aperture Radar (SAR) ($30 - 300mm$)

SAR synthesizes a large virtual receiving antenna by processing the phase of the reflected radar return. The along-track resolution, corresponding to the resolution along the flight direction of the spacecraft, is obtained by timing the radar return. The cross-track resolution, corresponding to the resolution perpendicular to the flight direction of the spacecraft, is obtained by processing the Doppler phase of the radar return.

Undisturbed water surface acts as specular reflector for incident microwaves and thus open water areas yield no or very low return signal (low back-scattering values below $-20dB$), and can therefore be distinguished from other land surface (Zhou *et al.*, 2000). However, as for optical, the sediment load, the wind leading to waves and hence increasing surface roughness, as well as the vegetative components, in or covering the water, can have major impacts on the signal. Moreover, other surfaces such as very dry terrain (sand), smooth surface or road have also very low backscatter values and could thus be confused with water. The spectral bands most used for water are L-Band ($15 - 30cm$), C-Band ($3.75 - 7.5cm$) and X-Band ($2.5 - 3.75cm$).

Various methodologies were developed to map water with SAR providing observations independently of the weather conditions. Matgen *et al.* (2011) proposed radiometric thresholding with region-growing approaches. Pulvirenti *et al.* (2011) developed a fuzzy-logic approach considering three scattering models. Martinis *et al.* (2011) used a near real time split-based histogram

thresholding and segmentation-based classification. Other studies used the multitemporal observation of SAR to filter the speckle noise (Geldsetzer *et al.*, 2010; Bartsch *et al.*, 2012; Kuenzer *et al.*, 2013; Santoro and Wegmuller, 2014; Santoro *et al.*, 2015a). Because of the limited SAR data availability, as well as the noise and confusion specific to water, SAR could be used as a complement to optical sensor, much constrained by atmospheric perturbations and clean coverage.

Although SAR has shown a good potential for inland water body mapping, systematic global coverage with free available data has only recently became a reality thanks to the launches of Sentinel-1 A and B (respectively the 3 April 2014 and the 25 April 2016). This is the reason why this thesis focuses on optical methods even if the SAR contribution will be discussed throughout the manuscript.

Optical sensors suited for inland water mapping

Table 2 summarizes a selection of current and future optical sensors mentioned in the thesis and suited for inland water body mapping at different spatial resolution and addressed in the thesis. First, the Very High Resolution (VHR) sensors have a spatial resolution close to 1 m and include airborne aerial photography and commercial satellites such as World-View. VHR acquisitions are always on demand and data is limited. Second, the High Resolution (HR) sensors such as LANDSAT 5;7;8, SPOT 5;6;7 and SENTINEL-2 A;B have a spatial resolution ranging from about 5 m to 30 m and provide a global coverage. Access to the data is limited for SPOT but are free for LANDSAT and SENTINEL-2. Thanks to the recent success launches of Sentinel-2, the HR observation capacity has improved substantially reducing the revisit interval from 16 days for LANDSAT to 5 days. Finally, Medium Resolution (MR) sensors such as SPOT-VEGETATION 1;2, MODIS Terra;Aqua, PROBA-V and Sentinel-3 A;B, provide a daily global revisit at resolution ranging from 250 m to 1 km.

Note that geostationary satellites used for meteorology have a more frequent coverage but a lower spatial resolution (up to 1 km for the future Meteosat Third Generation (MTG) to come in 2018) and are thus not well suited for water body mapping.

Table 2: Selection of optical sensors mentioned in the thesis and suited for inland water mapping along with their specifications.

	Mission/satellite	Years of operation	Ground resolution (m)	Revisit interval (days)	Acquisition	Cover-age	Access
VHR	Airborne	On demand	<1	On demand	On demand	Local	Limited
	World-View 2; 3	2009, 2014	1.84; 1.24	1.1	On demand	Global	Limited
HR	LANDSAT 5; 7; 8	1984–2013, 1999, 2013	30	16	Systematic	Global	Free
	SPOT-HR 5; 6; 7	2002-2015, 2012, 2014	10; 6; 6	26–5 (1 with SPOT 6–7 in constellation)	On demand	Global	Limited
	SENTINEL-2 A; B	2015, 2017	10 (20)	10 (5 in constellation)	Systematic	Global	Free
MR	SPOT-VEGETATION 1;2	1998-2013, 2002-2015	1000	1	Systematic	Global	Free
	MODIS (AQUA; TERRA)	1999, 2002	250 (500)	0.5	Systematic	Global	Free
	PROBA-V	2013	333	1	Systematic	Global	Free
	SENTINEL-3 A; B	2016, 2017	300	3 (1 in constellation)	Systematic	Global	Free

***VHR**: Very High Resolution; **HR**: High Resolution; **MR**: Medium Resolution.*

Limitations of optical remote sensing for inland water mapping

Accurate estimation of surface water using satellite imagery remains a challenging task due to the sensor limitations, complex land cover, topography and atmospheric conditions (Donchyts *et al.*, 2016). The limitations of optical remote sensing for inland water mapping are here listed and described hereafter: water diversity, atmospheric perturbations, sun glint, adjacency effect and confusion with dark area such as shadows, dark lava and basalt.

Water diversity. The optical properties of water are conventionally divided into two classes (Devred *et al.*, 2013): (1) the *inherent optical properties* depending only on the medium (*i.e.* water) and independent of the ambient light field within the medium, and, (2) the *apparent optical properties* depending on the medium as well as the geometric structure of the ambient light field within the medium. The fluctuation of the inherent optical properties depends on organic matter types and contents (Colored Dissolved Organic Matter (CDOM), phytoplankton, viruses, bacteria) and non-living (mineral). Moreover they can fluctuate with temperature and salinity (Sathyendranath *et al.*, 2004). On the other hand, the apparent optical properties vary according to the morphology of the water body, to the illumination conditions and to the geometry of the observation. In addition, the bottom material of the water body and the water surface conditions driven by the wind and the water stream modify the aspect of the water. As illustrated in the Figure 4, the aspect of water bodies varies substantially according to their contents and their morphologies making them challenging to map. These true-color composites show water diversity looking, white, blue, green, black and cyan. This diversity is a main challenge to develop robust mapping method using optical remote sensing.

Another scientific community has interested in water diversity as they are studying the ocean color. These researchers are usually using coarser spatial resolutions unsuitable for remote sensing applications over most rivers, lakes and reservoirs (Palmer *et al.*, 2015).

Atmospheric perturbations. A major uncertainty in remote sensing of inland water remains the atmospheric correction. Under most circumstances, over 90% of the light reaching a satellite over an aquatic target derives from the atmosphere and not from the water surface (Wang, 2010). Indeed, the Top Of Atmosphere (TOA) radiance measured by a satellite sensor should be converted integrating information from the sensor and the atmosphere to retrieve reflectance of the water surface. The radiance is thus first converted into reflectance by normalizing the radiance to the band averaged irradiance and using thus the sun zenith angle and the sun-earth distance. Second, the TOA reflectance consists in three components to separate: (1) the aerosol reflectance, (2) the Rayleigh reflectance and (3) the water leaving radiance above the surface water multiplied by the two-way diffuse atmospheric transmittance. The Rayleigh reflectance could be simply estimated using sun and sensor geometry. For the aerosol component, it is much more complex particularly on water.

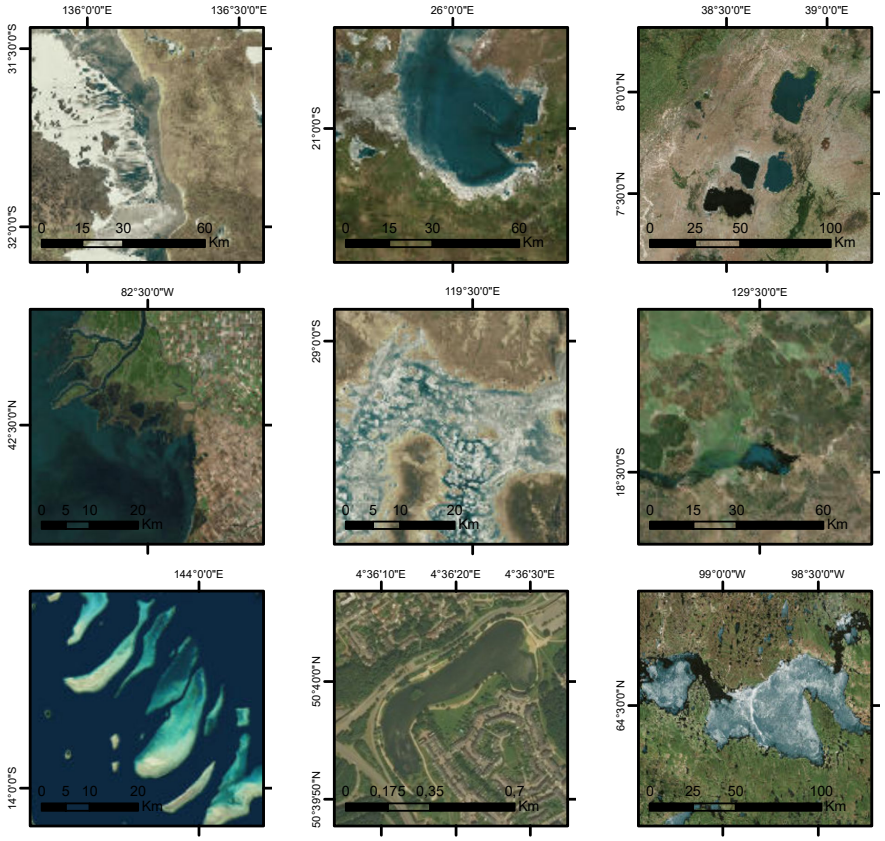

Figure 4: True color composites showing the diversity of water body aspects varying according to their inherent and apparent optical properties making them challenging to map.

Various techniques have been developed by researchers especially for ocean. The open ocean atmospheric correction schemes typically use NIR bands where the signal from water is assumed to be zero (Gordon and Wang, 1994). For clear water, this is a valid assumption, as the water absorption is very high in the NIR, and there is almost no contribution from suspended particles (Mouw *et al.*, 2015). The NIR signal received at the sensor is thus assumed to be entirely atmospheric and is used to determine the aerosol model. With the aerosol model, the aerosol reflectance could be extrapolated to the visible bands. However, inland surface water typically contains suspended matters or has a turbid behavior yielding in a not negligible NIR band. To overpass those limitations, researchers have developed two approaches (Vanhellemont and Ruddick, 2015): (1) modeling the contribution of the water components to the NIR and (2) using the SWIR bands instead of the NIR which is less impacted by suspended matters. While those approaches were developed for turbid water in the oceans, some studies designed

for inland water have recently shown interesting results (Sterckx *et al.*, 2015; Vanhellemont and Ruddick, 2015) but further developments are still needed.

Sun glint. Sun glint occurs in imagery when the water surface orientation is such that the sun is directly reflected in a specular way towards the sensor, and hence is a function of water surface state, sun position and viewing angle. Kay *et al.* (2009) reviewed the correction methods for the sun glint for ocean and coastal scenes. The authors divided the methods into two groups: (1) statistical methods using sun and sensor position data, as well as wind information to predict sun glint, and (2) methods using the NIR signal. Unfortunately, while those methods have been successfully developed and are increasing the proportion of data that can be retrieved from ocean and coastal areas, they are not well suited for inland water surface and sun glint still hamper water body mapping substantially.

Adjacency effect. High reflectance from nearby land or clouds is affecting the reflectance of water bodies. Indeed, the scattering of stray light from land into the sensors field of view is known to be a significant source of error in the NIR bands (Giardino *et al.*, 2007). These environmental effects hamper the correct retrieval of water quality and aerosol parameters from remotely sensed imagery. The problem has been observed many times in medium or low resolution ocean color imagery (Simis *et al.*, 2006; Feng *et al.*, 2011; Potes *et al.*, 2012) and will be even more pronounced when Earth Observation (EO) monitoring efforts will address small inland water bodies, estuaries and coastal waters with recent satellite missions such as Sentinel-2 (Sterckx *et al.*, 2015).

Dark surfaces. Water detection is hampered by the presence of other dark surface in the image (Bochow *et al.*, 2012). Indeed, the dark aspect of water and its low reflectance are shared with other surfaces such as dark rocks (*e.g.* lava or basalt), burnt areas, bitumous roofing materials or roads, and especially with pixels covered by shadows. The shadow is an important problem for water remote sensing and is related to landscape feature (house, tree), topography (mountain, slopes), dynamic elements (clouds, cars, boats), as well as sun elevation and azimuth angles which are changing over time. Most of the cloud shadow detection algorithms use the thermal band to estimate clouds' height (Khlopenkov and Trishchenko, 2007; Masek *et al.*, 2006; Zhu and Woodcock, 2012; Huang *et al.*, 2010). However, recent researches develop methods using the cirrus band (Zhu *et al.*, 2015). This could be more used in the future, as there is a cirrus band on Landsat-8 and Sentinel-2 instrument. Alternatively, to estimate the shadow of objects (house, tree...), the surface elevation of the object, as well as the sun and azimuth angles can be used to calculate the geometric shadow cast (Radoux *et al.*, 2010). Other methods detecting shadow have been developed such as morphological shadow index (Huang and Zhang, 2012; Huang *et al.*, 2015) or neighborhood counting using a growing kernel filter (Bochow *et al.*, 2012). In conclusion, dark surface confusion along with shadow estimation for both clouds and features still remain a challenge for water remote sensing.

Scale issues

In the previous section, the remote sensing capability and issues for inland surface water mapping was summarized. However, the mapping scale often induces the use of different sensors, methods and even properties of the observed surface waters. This section aims to review some aspects related to the scale in remote sensing.

Land cover and land use modeling use representation of phenomena at a multiplicity of spatial scales. 'Scale' is used to refer both to the magnitude of a study (e.g., its geographic extent) and also to the degree of detail (e.g., its level of geographic resolution). It is used in the context of space (geographic scale), time (temporal scale), and many other dimensions of research (Goodchild and Quattrochi, 1997). The notion of scale specific to remote sensing was studied by many authors. At the end of the 80's, Woodcock and Strahler (1987) found that the local variance of the image is related to the objects' size in the scene and the sensor spatial resolution. Focusing on crop area estimation, Ozdogan and Woodcock (2006) have studied the behavior of errors resulting from the distribution of sub-pixel proportions. Based on the spatial structure of the land cover class of interest in a given region, they indicate that the use of variogram could help to choose the adequate spatial resolution for area estimation.

Beside those studies linking spatial resolution with the landscape structure, the effect of spatial scale on classification accuracy was also studied by many authors (Markham and Townshend, 1981; Irons *et al.*, 1985; Marceau *et al.*, 1994; Raptis *et al.*, 2003).

Although generalization to other land cover thematic classes is sometimes possible, few studies have addressed specific issues related to the scale on water bodies mapping. Some studies have attempted to estimate small water bodies that could not be mapped because of limited spatial resolution by estimation of their distribution in number and size. The relationship between the number of water bodies larger than a surface and its water body surface area was found to follow a Paretian distribution by some studies and was thus used to estimate smaller water bodies that could not be mapped (Hamilton *et al.*, 1992; Lehner and Döll, 2004; Downing *et al.*, 2006; Grosse *et al.*, 2008). Other studies invalidate this assumption suggesting that this Paretian behavior is limited to flat areas or was linked to the lack of smaller ponds integration for distribution estimation (Seekell *et al.*, 2013; Muster *et al.*, 2013). Those studies suggest more complex relation to be investigated by scientists. In conclusion, scientists are trying to estimate the distribution of water according to their size, number and resolution but this relation is not yet well defined leading to underestimation of the smaller water bodies. The notion of scale is central in this thesis and will be addressed by providing multiple scales of study for water mapping with their corresponding sensors, methods and landscape spatial structure.

Scope and objectives

Despite remarkable advances in optical remote sensing technologies over the past decades, consistent mapping of the inland water remains an important challenge as illustrated by global inland surface water estimation which still varies from simple to double according to authors (2.2 % of the Earth surface according to Raymond *et al.* (2013) and 3.6 % according to Verpoorter *et al.* (2014)). The major obstacles to map water are the spectral heterogeneity of the water and the diversity of the sensors along with their observation conditions. Indeed, water body is intrinsically a dynamic land cover varying in time, size and physical properties, embedded in heterogeneous landscapes, which can be observed at different spatial resolution and temporal frequency using various sensors. However, the importance of providing accurate water body maps, enabling better management of this precious natural resource, is increasingly accepted, and even requested by scientists and policy makers.

In this context, we aimed at mapping consistently inland water bodies with optical remote sensing at different spatial and temporal resolutions. The consistency is defined as the quality of achieving a level of performance which does not vary greatly in quality over time (Oxford Dictionary, 2016). In this thesis, we expand the consistency definition through space, instrument and context. Such consistent mapping is achieved by developing appropriate methods taking into account temporal frequency, environment and observation sources. In this context, the overall research question of this thesis is formulated as follows: *Can surface water mapping be consistent across spatial and temporal scales independently of the environmental context and the observation system?*

This objective is more specifically structured into three research questions formulated below.

How to map surface water consistently across time and spatial scales? Due to inherent spatial and temporal scale constraints and despite recent efforts to harmonize land cover class systems such as the Land Cover Classification System (LCCS) (Di Gregorio, 2005), most of the studies use their own water body definition based on their observation capacities which limits the method transposition and generalization across scales and sensors. By mapping and

monitoring water bodies with different sensors, time and spatial scales, this thesis addresses the inland surface water definition with the objective of reducing inherent limitations coming from specific scales and sensors.

Can water body mapping be consistent using different Earth observation sources? Traditionally, ground survey is used to map surface water. However, remote sensing provides an invaluable cost effective synoptic tool able to map land cover classes. A major challenge is to dispose of quality remote sensing information with a sufficient revisit frequency and spatial resolution. Despite the recent availability improvement of optical remote sensing time series at finer spatial resolution (250 m, 30 m and 10 m), heterogeneity between sensor sensitivity and technical specifications could hamper multi-source water mapping by not providing consistent water delineation. To overpass those constraints, this thesis proposes appropriate methods mobilized according to sensor types. In addition to sensor diversity, handling the variability in the observation conditions is a major challenge to map surface water on large extents. This is the reason why, despite the proven success of several proposed water detection methods, few methods appear to work operationally over large areas. This thesis will address the heterogeneity of observation conditions by suggesting methods to limit its impact.

Can we map all the water bodies with similar performance despite their large optical properties diversity? The chemical components and the morphology of the water body vary according to their environment, resulting in high spectral diversity of the surface water. Although empirically efficient specific water body mapping methods have already been developed, no generic approach providing a consensus among researchers and stakeholders offers an accurate mapping without local fine-tuning. Consequently, the challenge of developing methodologies able to handle water body diversity persists. This thesis contributes to the development of several remote sensing mapping methods dealing with the diversity of water bodies due to their inherent and apparent optical properties.

Novelty and outline of the thesis

The core of this thesis is based on scientific papers which are at different levels of publications. The four chapters address water mapping at different spatio-temporal resolution trade-offs represented by the dashed line in Figure 5. The current and future sensor availability trend shows a resolution trade-off shift represented by the arrow in Figure 5.

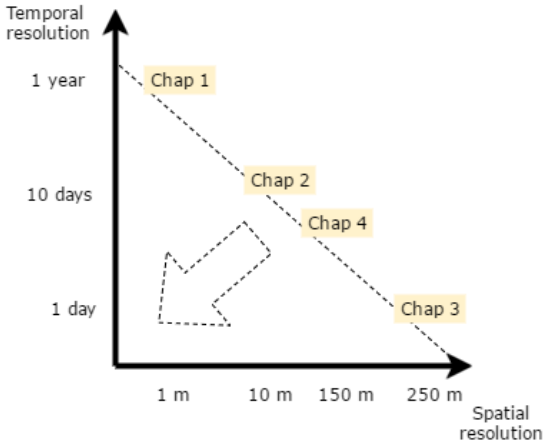

Figure 5: The four chapters address water body mapping at different spatial and temporal resolutions. The arrow represent the potential Earth sensor improvements.

In addition to addressing the surface water mapping at different scales, this thesis design and experiment new methods to match EO Big Data challenges. EO data are growing in size and variety at an exceptionally fast rate. New satellite, airborne and ground-based remote sensing systems characterized by high spatial, temporal and radiometric resolution are available. The term Big Data is one of the current major trends in data science and information technology. However the Big Data concept itself is elusive, bringing to many possible definitions according the different aspects the focus is put on (Nativi *et al.*, 2015). Build on the definition of Beyer and Laney (2012), a consensus definition of Big Data is now accepted as characterized by the 5 "V"s: volume, variety, velocity, veracity and value (Guo *et al.*, 2017). These "V"s are a unifying thread in this thesis:

- Volume: The amount of remote sensing data produced by airborne and spaceborne sensors is increasing at a rate of several Terabytes (Tb) per day. By end of 2016, 6 Tb of EO data are received each day from the Sentinel fleet (Bargellini, 2016). The volume of EO data continues to multiply exponentially due to the launch of new flying platforms, hosting more powerful, multispectral, and accurate sensors. Similarly, due to their very resolution, aerial photos , such as in chapter 1 (25 cm), represent a large volume of data (totaling 593 billion of 25-cm pixels for a regional

acquisition). In this thesis, several methods were developed to handle this large volume of data.

- Variety: EO data is characterized by a significant heterogeneity due to historical and technological reasons, including: different acquisition sensors, diverse methodology to describe the real world phenomena (*e.g.* field or coverage view and feature or boundary view), different encoding formats (Nativi *et al.*, 2015). Along this thesis, specific frameworks were developed to handle this data heterogeneity in particular for various platforms (satellite and aircraft), different instrument types (spectrometer, LiDAR, multispectral camera) and different wavelengths (visible, NIR, SWIR).

- Velocity: Data to be delivered timely to users requiring fast responses. As to velocity, near real-time analytics is important to generate high-level products (*e.g.* physical parameters) from low level remotely sensed data. For EO applications, velocity is also about linking heterogeneous datasets that are coming with different speeds, *e.g.* remotely-sensed and in-situ spatial and temporal series. This thesis contributes to the set-up of near real time methods thanks to fully automate processing but also combines dataset acquired at different time scale.

- Veracity: Decision making and operations require reliable sources thus meaning the need of documenting quality and uncertainty of the data. This thesis provides methodologies to validate the mapping product and thus improving the qualification of the data.

- Value: Information to be provided has to be clear and useful pointing out the need of filtering data for valuable information (Guo *et al.*, 2017). This thesis contributes to provide pragmatic solution for water mapping usable by stakeholders and decision makers.

In addition to this Big Data common features shared by the chapters of the thesis, different extents are considered going from local to global along the chapters (Figure 6).

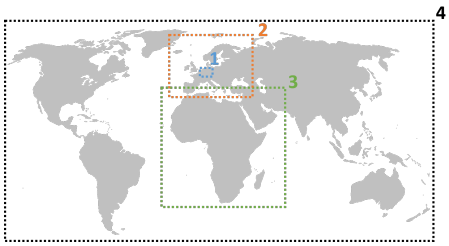

Figure 6: Different sizes of the study area are considered ranging from local to global scale: regional (chapter1), regional-continental (chapter 2), continental-global (chapter 3) and global (chapter 4).

In the **first chapter** of this thesis, we develop a framework to update hyper-spatial (<**1m**) water body map over large areas by handling multi-source remote sensing data (LiDAR and visible-NIR aerial photos) with very heterogeneous observation conditions and various environmental contexts in order to improve the delineation of water bodies.

The **second chapter** combines a spectral separability analysis and an empirical estimation of point spread function to assess the minimum size of water body that could be mapped at sub-pixel level from decametric sensors (**10m**). In particular, we are interested to assess Sentinel-2 potential for water sub-pixel detection in comparison with other HR sensors. In addition, Sentinel-2 water sub-pixel mapping is compared with maps obtained using the framework developed in chapter 1.

Building upon the availability of high temporal frequency Earth Observation datasets at MR, the **third chapter** investigates the feasibility of mapping and monitoring water bodies at continental scale from MODIS. A seven year time series of twice-daily observation covering the whole African continent is systematically processed using a surface water detection method to produce maps and 10-day indicators describing the location, the intra-annual and the inter-annual behavior of the inland water bodies at a **250-m** spatial resolution.

Map validation is challenging, especially for underrepresented dynamic land cover classes such as inland water representing a small fraction (∼3%) with regards to land surface (∼97%). In the **fourth chapter**, we address water body map validation challenge by proposing an original validation strategy specific for permanent water at global scale. This validation is applied on a **150-m** global surface water product.

The main findings with regards to the objectives and future perspectives are summarized and discussed in the **last chapter** of this document.

Chapter 1

Sub-metric water detection handling data heterogeneity

Abstract. Recent advances in remote sensing technologies and the cost reduction of surveying, along with importance of natural resources management, bring new opportunities to mapping land cover at very high resolution over large areas. This chapter proposes and applies a framework to update hyperspatial resolution (<1 m) land thematic mapping over large areas by handling multi-source and heterogeneous data. This framework deals with heterogeneity both from observation and from the targeted features. First, observation diversity comes from the different platform and sensor types (25-cm passive optical and 1-m LiDAR) as well as the different instruments (3 cameras and 2 LiDARs) used in heterogeneous observation conditions (date, time and sun angle). Second, the local heterogeneity of the targeted features results from their within-type diversity and neighborhood effects. This framework is applied to surface-water bodies in the southern part of Belgium (17,000 km^2). It makes it possible to handle both observation and landscape contextual heterogeneity by mapping observation conditions, stratifying spatially and applying ad hoc classification procedures. The proposed framework detects 83% of the water bodies – if swimming pools are not taken into account – and more than 98% of those water bodies greater than 100 m^2, with an edge accuracy below 1 m over large areas.
The proposed framework and its application developed in this chapter is modified version of a published article*. My contribution was on the design, development and application of the framework.

*d'Andrimont, R., Marlier, C. & Defourny, P. 2017. Hyperspatial and Multi-Source Water Body Mapping: a Framework to Handle Heterogeneities from Observations and Targets over Large Areas, in *Remote Sensing*, 9(3), p. 211.

1.1 Introduction

Many organizations require very high resolution land cover information for various applications, including environmental modeling, land-use planning, policy impact assessment and spatial patterns of biodiversity understanding.

Thanks to recent technology developments, reduced remote sensing costs and the acceptance of their importance among land cover managers, organizations in charge of land management now have higher spatial-resolution data at their disposal. Hyperspatial resolution (<1 m) (Greenberg *et al.*, 2005) data brings a number of challenges for the remote sensing community in terms of processing capacity but especially in terms of scale. Hyperspatial resolution does indeed enable more precise landscape feature delineation and detects a new set of features, thus opening up new fields of research. However, in some circumstances this high resolution actually confuses the issue by increasing the level of intra-class variation and by introducing spatial heterogeneity resulting from in-shadow pixels (Rocchini *et al.*, 2010).

Acquiring hyperspatial data on a regional scale needs multiple data acquisitions resulting in heterogeneity of the observation conditions. Handling this heterogeneity is a pre-requisite operation to upscaling detection methods over larger areas for different types of thematic mapping such as water surfaces.

Inland surface water is of paramount importance for land use planning, environmental monitoring, industrial and agricultural production, natural disasters and transportation. Moreover, inland water ecosystems are involved in many processes such as carbon and nutrient cycles, biodiversity, climate change and ecosystem services upon which human society relies. Therefore, their protection and rehabilitation is supported by various international treaties and organizations such as the Ramsar Convention (Davis, 1994), the European Union (EU) Common Agricultural Policy and the EU Water framework directive (Directive 2000/60/EC), as well as by national and sub-national legislation for nature (Verhoeven, 2014).

In addition to the fact that sub-meter water delineation provides a more precise landscape feature delineation that is always desirable for researchers as well for policy makers, it also improves the ability to detect very small water bodies which is crucial for two domains: the nutrient cycle and the biodiversity.

First, Holgerson and Raymond (2016) have recently brought to light the major contribution of very small ponds (less than 1000 m^2) to CO_2 and CH_4 emissions. As the global distribution of these ponds is uncertain because of the difficulty in mapping them globally, they are excluded from carbon budgets. However, CO_2 and CH_4 concentrations are greatest in small ponds and decrease with increasing lake size. This may be due to the changing perimeter-to-surface ratio leading to a higher load of terrestrial carbon relative to the water volume. Moreover, Marton *et al.* (2015) show the importance of geographically isolated ponds in the biogeochemical equilibrium. Indeed, wetlands across the landscape reduce the amount of C, N, P, and sediments reaching downstream aquatic systems. Additionally, wetlands and ponds in agricultural landscapes play a key role in nitrogen attenuation (Hefting *et al.*, 2013). To conclude, inland waters such as lakes, wetlands and also small and isolated ponds play a key,

but complex, role in both the carbon and the nutrient cycles. Their accurate mapping at the finest scale is thus critical.

Second, water surfaces are crucial to supporting biodiversity. Inland freshwater supports at least 100,000 species out of approximately 1.8 million, representing almost 6% of all described species (Dudgeon *et al.*, 2006). Fresh waters are experiencing declines in biodiversity far greater than those in the most affected terrestrial ecosystems (Sala *et al.*, 2000). This is partly explained by the fact that inland waters as a habitat for plants and animal are far richer than are terrestrial ecosystems. Collen *et al.* (2014) confirmed that there is a higher risk of extinction for freshwater species than for terrestrial. If trends in the human demand for water remain unaltered and species losses continue at current rates, the opportunity to conserve much of the remaining biodiversity in fresh water will vanish (Dudgeon *et al.*, 2006). Various threats are dramatically and rapidly affecting the rich biodiversity of inland waters (Brönmark and Hansson, 2002) thus reinforcing the need for close monitoring of inland surfaces. In terms of biodiversity, it is particularly important to monitor small water bodies as they structure the ecological network. Normally free of reproducing fish populations, very small water bodies are capital breeding habitats for numerous amphibians and reptiles adapted to reproduction in fishless habitats (Wu *et al.*, 2014).

Mapping the physical, chemical and biological status of global inland waters is immensely important to scientists and policy makers alike. Whereas conventional monitoring approaches tend to be limited in terms of spatial coverage and temporal frequency, remote sensing has shown the potential to provide an invaluable complementary source of data at local to larger scales (Alsdorf *et al.*, 2007; Alsdorf and Lettenmaier, 2003; Famiglietti *et al.*, 2015). Furthermore, as sensors, methodologies, data availability and the network of researchers and engaged stakeholders in this field develop, the increasingly widespread use of remote sensing for operational monitoring of inland waters can be envisaged (Palmer *et al.*, 2015). Beside surfaces delineation, remote sensing can assist various disciplines providing indicators or variables on water bodies such as parameters specific to rivers: turbidity, depth, in-stream habitats, substrate size, algae and wood (Marcus and Fonstad, 2008); or for lakes: water transparency, biota, hydrology, temperature and ice phenology (Dörnhöfer and Oppelt, 2016). Nevertheless, few studies have addressed the delineation of water bodies at sub-metric resolution. However, among the river scientist community, sub-meter method to retrieve specific river features such as depth (Marcus *et al.*, 2003; Lejot *et al.*, 2007), in-stream habitat (Marcus *et al.*, 2003; Goovaerts, 2002), substrate size (Carbonneau *et al.*, 2004; Carbonneau and Lane, 2006), algae (Marcus *et al.*, 2000) and wood (Marcus *et al.*, 2003) have been developed but do not provide water detection and delineation approaches.

Hyperspatial water mapping has also been proposed using other methods such as sub-pixel or super resolution at a larger scale (Marcus and Fonstad, 2008; Li *et al.*, 2015; Manakos *et al.*, 2014; Sakthivel *et al.*, 2014; Foody *et al.*, 2005; Muster *et al.*, 2013) but the concept is different as they use coarser resolution pixels and try to map and estimate water coverage inside the pixel.

A significant amount of research has been conducted to extract water body information from various electromagnetic remote sensing measurements at

different temporal and spatial scales. Among those, passive optical multispectral imagery, active optical Light Detection And Ranging (LiDAR), active Synthetic Aperture Radar (SAR) and passive Thermal Infrared are the most widely used. This study focuses on passive optical multispectral imagery and LiDAR as the data were available at a sub-metric resolution on the study area under consideration.

Passive optical multispectral imagery records reflected sunlight in the visible and shortwave infrared spectra. The optical environment of a water surface is complex and dynamic through both space and time. As the water reflectance in the visible near-infrared wavelength is always lower than other landscape features, the radiance range is small compared to most of land cover features (Marcus and Fonstad, 2008). This limited range could lead to confusion between water and other low radiance features such as shadows or buildings. Marcus and Fonstad (2008) described the details of the optical constraints. (1) The obstruction of the water surface by extrusions, such as trees, bridges and woods, prevent the use of optical remote sensing to map water bodies. (2) The second major constraint is the shadow on the water. (3) The third constraint is a result of the sun-target-sensor geometry; the water surface looks very different depending on the time of the day because of the specular effect. The sun angle could lead to sun glint which can blind the sensor (Dörnhöfer and Oppelt, 2016). Wind and water turbidity could lead to riffle, which could reflect the light very differently according to the angle. (4) Fourth, the water appearance is linked to the morphology of the water bodies, which is dynamic over time. The water depth, the sediment type and load also play key roles in the reflected light. Additionally, variations in irradiance and reflectance across images lead to problems when mosaicking a huge number of scenes. All those constraints could be addressed individually but are difficult to take into account when working over large areas. Aerial photos offer the high spatial resolution desirable for detecting many wetlands and water bodies features, but typically involve time- and experience-intensive visual interpretation or manipulation (Gallant, 2015). This paper proposes a framework that handles those four constraints while limiting human effort.

LiDAR sends out a laser signal pulse and records the timing and intensity of its return (Campbell and Wynne, 2011). High-resolution LiDAR has already been used to delineate water bodies in different studies (Lang *et al.*, 2010; Hofle *et al.*, 2009; Brzank and Heipke, 2006; Lichvar *et al.*, 2006). LiDAR data can facilitate the detection of wetlands that are normally difficult to identify, such as vernal pools (Wu *et al.*, 2014). Standard LiDAR sensors emit short-wave near-infrared laser pulses which are mostly absorbed by the water and hence are scattered and reflected at the water surface. Most of the energy is absorbed in the water column or reflected specularly away from the field of view of the receiver (Hofle *et al.*, 2009). The major constraints of LiDAR for water mapping are thus: (1) other surfaces than the water bodies absorb the LiDAR pulses and are thus confused with water; (2) when the pulse is specularly reflected, the pulse could be reflected directly towards the sensors, so blinding the sensor.

The combination of high resolution imagery and LiDAR can counterbalance the specific constraints of each technique and is thus suited to retrieving

information on land cover features. Researchers have used this combination to map specific thematic classes such as urban areas (Hodgson *et al.*, 2003; Chen *et al.*, 2009), rangeland vegetation (Bork and Su, 2007), woodland vernal pools (Wu *et al.*, 2014), swimming pools (Rodríguez-Cuenca and Alonso, 2014), wetlands (Maxa and Bolstad, 2009), inundations (Lang and McCarty, 2009) and coastal areas (Elaksher, 2008). Additionally, data fusion methods combining imagery and LiDAR have been used for land classification (Bigdeli, 2014) and for complex heterogeneous regions (Zhu *et al.*, 2010) (for a review of remote sensing multi-source data fusion, see Zhang (2010)).

No method has been proposed so far to map inland surface water and able to handle hyperspatial multi-source data over large areas taking into account observations and targets heterogeneity. The objective of this paper is to propose and apply a framework to map water bodies dealing with heterogeneity from the observations due to the use of different platforms (aircraft, satellite, UAV), sensor types (optical, LiDAR, SAR) and instruments used in heterogeneous observation conditions (date, time and sun angle). Additionally, the aim of the proposed method is to take into account the local heterogeneity of targeted features resulting from their *within-type diversities* and *neighborhood effects*.

After the conceptual framework definition and presentation (section 1.2), the study region and the vector dataset to update is presented (section 1.3). The description and application of the framework to surface water bodies is then presented (section 1.4), followed by its results and evaluation (section 1.5) over an area of 17,000 km^2 using sub-metric data.

1.2 Conceptual framework

The framework rationale is based on the idea of reducing the heterogeneity of both observations and target land features. The underlying assumption is that feature detection is improved by reducing observational and target heterogeneity. First, observational heterogeneity depends on the platform used (UAV, airborne, satellite), the sensor type (optical, LiDAR, SAR), the pre-processing level and the recorded variables (instrument model, spectral band, resolution) (Figure 1.1 upper left). Additionally, observational heterogeneity depends on the acquisition conditions such as the season and time of the day characterized by the View Zenithal Angle (VZA), the Sun Zenithal Angle (SZA) and the date. Second, the target landscape feature itself is also heterogeneous by nature (Figure 1.1, top right). Specifically, the target features have a *within-type diversity* defined as the specific spectral heterogeneity of a given water body compared to other water bodies and is determined by the water components (chemical, organic) and the water body morphology (water depth, sediment type). It is independent of its observation and its neighborhood. In addition, the target features are affected by the *neighborhood effects* which consist in the effects altering water reflectance caused by local features such as shadows coming from bridges, trees and buildings.

The framework proposed in this paper is applied to update a pre-existing historical water body vector map (Figure 1.1, lower half). First, the mapping

of the instrument and data type along with the observation conditions provides a stratification used to split the data into homogeneous sets to process. In a second step, the proposed framework addresses the heterogeneity of the targeted feature itself and reduces local heterogeneity by mapping the neighborhood effects of shadows on water. A third step consists in a multi-source classification that handles the within-type diversity of the targeted landscape features; this results in water maps from aerial photos and LiDAR. Those two results are finally combined in a fourth step to update the pre-existing water map.

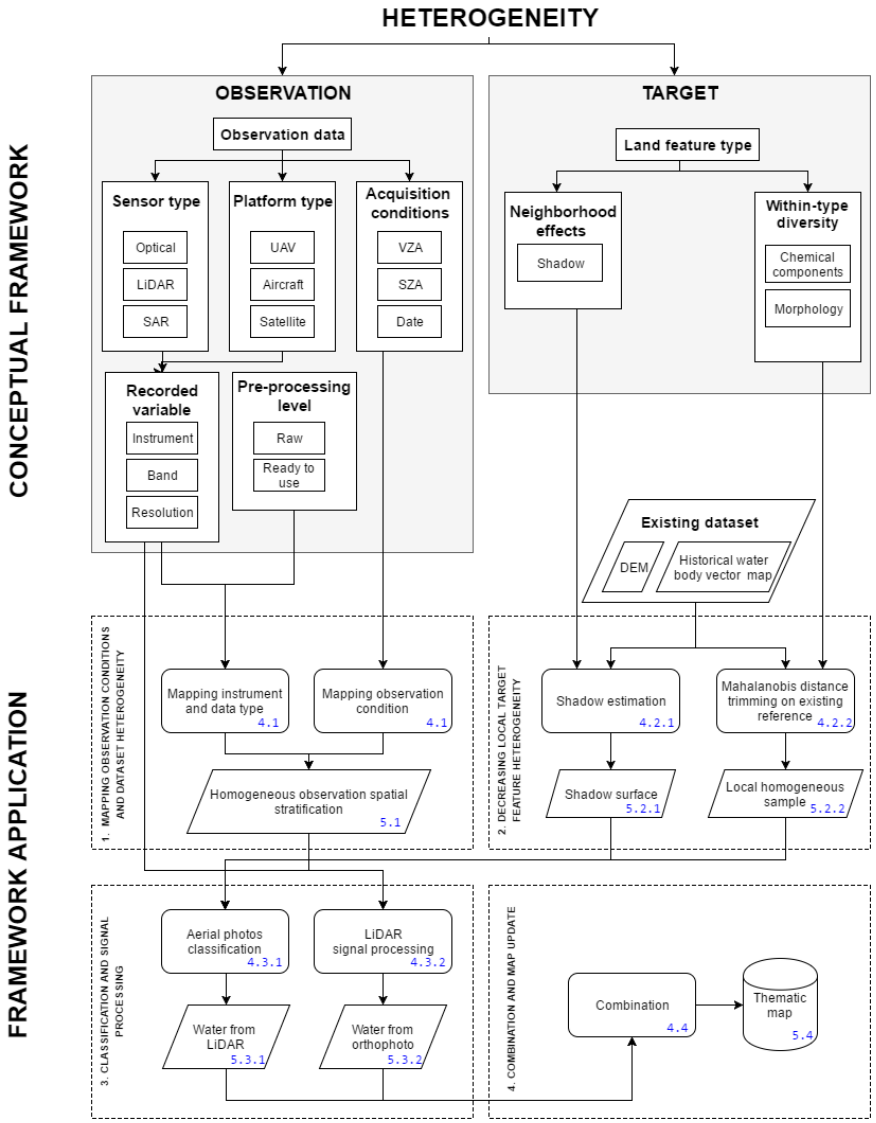

Figure 1.1: Conceptual framework to handle the heterogeneity of the observation and of the targeted land feature (top) and its application (bottom). The heterogeneity of the data observation comes from the sensor and platform-type of acquisition as well as from the observation conditions. The landscape feature within-type diversity and neighborhood effects are addressed by dedicated methods. Application of the framework is performed in 4 steps allowing the update of the hyperspatial thematic map. The corresponding section numbers of the framework application and of the results for each step are indicated in blue.

1.3 Study area

This section describes the study area with a focus on water bodies' heterogeneity and illustrates the heterogeneity of the target feature (figure 1.1 upper right). Additionally, the historical water body vector map to update is detailed.

1.3.1 Study region

The Walloon Region (Wallonia) forms the southern part of Belgium and covers about 17,000 km^2 (55% of Belgium). Altitude ranges from 25 m to 694 m. The Walloon Region has a climate influenced by the Gulf Stream and ocean disturbances. The weather is characterized by moderate temperatures, high cloudiness and frequent but sparse rainfall. It rains on between 160 and 200 days per year in Wallonia for a mean annual precipitation ranging from 700 mm to 1400 mm, representing a water intake of about 15-16 billion cubic meters per year.

A surface water body[†] is defined as a natural or artificial depression filled with water continuously or intermittently. The variety uses, the morphology and the composition of water bodies are linked to human activities and history. Rivers and streams are categorized into navigable or non-navigable and may have a natural or an anthropogenic origin. There are about 12,000 rivers located on four major river watersheds. The total surface of water bodies is 0.7% of the land surface. Apart from anthropic reservoirs and hydraulic power plant dams, there is no large lake in Wallonia. Ponds are frequently found and most of them have an anthropic origin. Ponds were created in arable land to water livestock (Figure 1.2-a), to raise ducks and geese, for flax and hemp retting, to nurture fish and frogs, for watercress and for game hunting. Ponds were also unwittingly created due to mineral extraction (Figure 1.2-b) (Graitson, 2009). There are also many ponds that have been created for biodiversity conservation, water management, and flood risk management (Figure 1.2-c-d-e-f-g). Recently, financial incentives from the European Common Agricultural Policy (CAP) have been given to farmers to preserve the small ponds in arable land (Kristensen and Globevnik, 2014). Some ponds may also have a natural origin (Figure 1.2-h). In particular, there are natural water bodies as a result of the water network evolution in floodplains such as backwaters. Some ponds in peat bogs – the 'lithalse' or the 'palse' have an ice age origin. Others, the 'mardelles', are formed by dissolution of the limestone in the marl. Due to their origin and their use, the water bodies thus have a large morphological and compositional heterogeneity. This heterogeneity in water bodies means that any successful mapping technique needs to be able to take into account all of these conditions.

[†]Referred as "Body of surface water" in the EU Water framework directive (Directive 2000/60/EC) and defined as a discrete and significant element of surface water such as a lake, a reservoir, a stream, river or canal, part of a stream, river or canal, a transitional water or a stretch of coastal water (Wallin *et al.*, 2003).

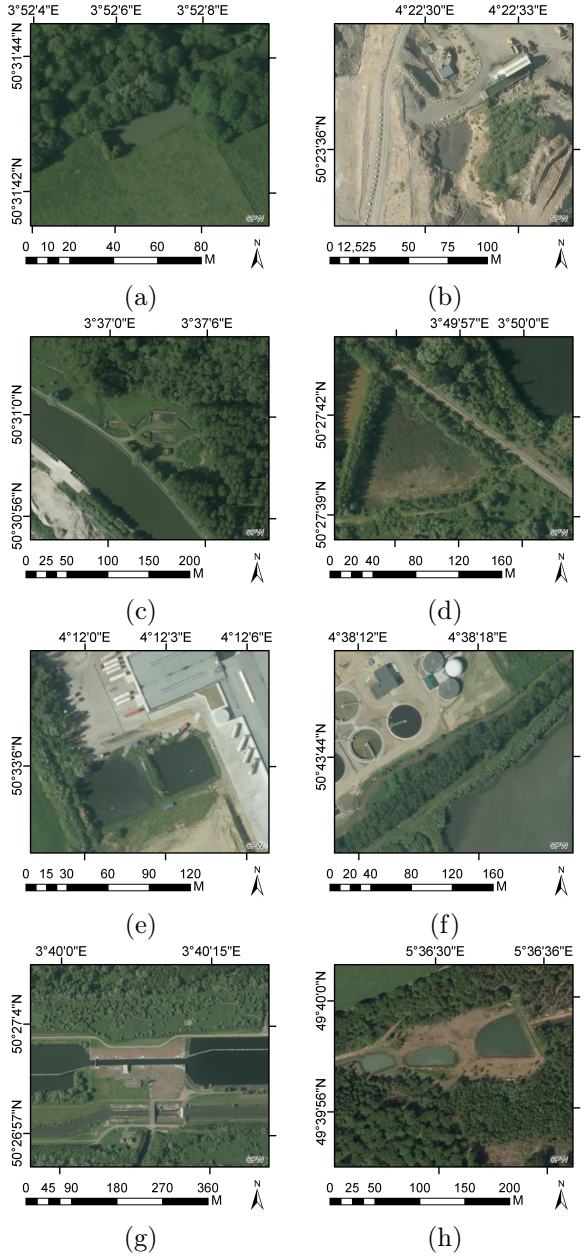

Figure 1.2: Water bodies may be of different origins and types: (a) pond in permanent pasture, (b) in a quarry, (c) pool and river, (d) ponds with temporal fluctuation, (e) in anthropic rural areas, (f) a waste-water treatment plant with basins, (g) in sluice, and (h) pond in forest zone. Their morphology, composition and thus their aspect are very heterogeneous.

1.3.2 Historical water body vector map

The proposed framework is applied on an outdated water body dataset (Figure 1.3) created in 2005. This database contains water bodies excluding rivers and is the result of the merging of various databases (Ernst *et al.*, 2008). The vector database (SPW, 2006) contains 36,335 water bodies with a geometric accuracy ranging from 0.25 to 1 m. Since 2005, the database has been updated by visual interpretation of aerial photos: in 2006-2007 (1% of the features updated), 2009-2010 (6% of the features updated) and 2012-2013 (1% of the features updated). Due to resource limitations, the update cannot cover the whole extent, so resulting in only a partly updated dataset. Moreover, the operator focus on updating water body delineation but not on adding new water bodies resulting in an incomplete dataset.

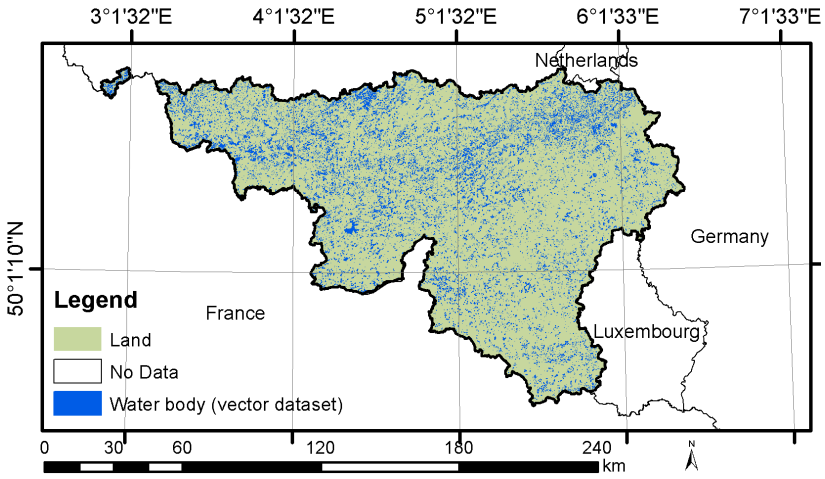

Figure 1.3: The historical water body vector map (SPW, 2006) contains natural or artificial depressions filled with water continuously or intermittently with a geometric accuracy ranging from 0.25 to 1 m. This 36,335 polygons dataset is not up to date although it is visually locally updated occasionally by an operator.

1.4 Framework application

The conceptual framework is applied in a 4-step workflow (sections 1.4.1, 1.4.2, 1.4.3 and 4.4) described at the bottom of Figure 1.1. The first step (1.4.1) uses metadata about the different data acquisitions to separate the products into groupings with consistent characteristics. The observation conditions mapping of the aerial photos and the LiDAR results in spatial stratification with homogeneous set of data. The second step (1.4.2) uses the pre-existing historical water body vector map to produce labelling data from which the outliers are removed through an iterative trimming of the data. Aerial photos are then cleaned by removing shadows via shadow projection estimation. The

third step (1.4.3) consists in aerial photo classification dealing with the water body within-type diversity and LiDAR signal processing handling the data sources specificities. The last step (1.4.4) of the workflow combines the results to update the initial dataset. Finally, the last section (1.4.5), not represented on Figure 1.1, presents the validation methodology.

1.4.1 Mapping observation conditions and dataset heterogeneity

Because the quality of the observations varies so much as a function of instruments and other characteristics not related to the target land feature, aerial photos classification and LiDAR signal processing were applied separately by tuning the methods for each set of data sharing acquisition characteristics. First, the aerial photos are split according to the cameras used, the date of the acquisition and the hours of acquisition used as a proxy of the SZA. Second, the LiDAR dataset is split according to the instrument and the date of acquisition. This produces an homogeneous observation spatial stratification (Figure 1.1 lower half, box 1) with different strata then processed separately.

Aerial photos

The aerial photos were taken on 9 separate days for 2012-2013 (Figure 1.4 a) using 3 UltraCam cameras (Figure 1.4 b) with 4 channels: red, green, blue, near infrared. The acquisition time varies from 7 AM to 3 PM (Figure 1.4 c) and the vertical sun angle varies from 34.2° to 63.2° (Figure 1.4 d). The flying altitude ranged from 4181 to 4617 m. The images were first radiometrically corrected. Automatic homologous points were generated and the Bundle Adjustment algorithm (Triggs *et al.*, 2000) was used to correct the distortion and to obtain an orthophoto mosaic. Verification acceptance provides a maximum RMSE of 0.856 m in X and 0.861 m in Y for 2012, and 0.977 m in X and 0.71 m in Y for 2013 (SPW, 2013).

The result is an aerial orthophoto mosaic composed of 5,872 irregularly shaped tiles (Figure 1.4 e). The image has a Ground Sampling Distance (GSD) of 25 cm and is 1,012,021 pixels in X and 586,567 pixels in Y, thus totaling 593 billion of pixels. To give some idea of comparative orders of magnitude, the conterminous U.S. Landsat WELD mosaic (Roy *et al.*, 2010) corresponding to 459 Landsat scenes contains in total 11 billion pixels. Consequently, the orthophoto data volume of the current study corresponds to the equivalent of more than 50 conterminous U.S Landsat mosaics in terms of pixels. In other words, in one 30-m Landsat pixel, there are 14,400 25-cm pixels. For processing and storage, the image is stored as a virtual GDAL dataset (VRT) (OGC, 2015).

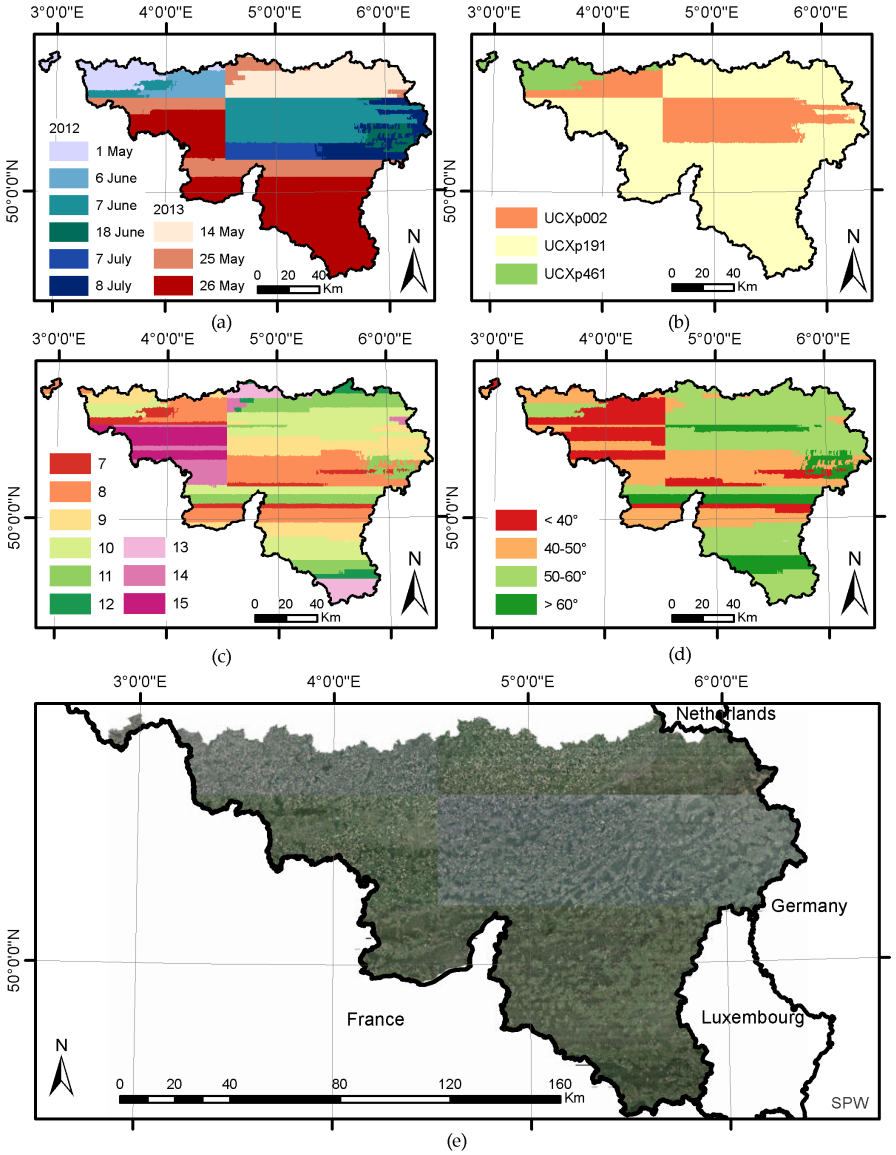

Figure 1.4: Aerial acquisition date (a), camera (b), local time (hour) (c) and sun vertical angle (d). The acquisition campaign was carried out using 3 cameras over 2 years from May to June (2012-2013), from 7 AM to 3 PM with vertical sun angle varying from 34.2 to 63.2°. The result is a heterogeneous mosaic (e) covering the southern part of Belgium and composed of 5872 tiles at 25-cm resolution.

LiDAR

The LiDAR acquisitions completed from 2012 to 2014 used two different sensors depending on the year of survey (Figure 1.5): Riegl LMS-Q680i for the western part in 2012-2013 and Riegl LMS-Q780 for the eastern part acquired in 2014. The power and wavelength are different for these 2 devices, the first one having less power, fewer echoes and a less suitable wavelength (1064 nm) than the second (1550 nm). Those two spatial strata will therefore be processed separately. The mean pulse density over the whole region is about 1.51 pulse/m^2. The western part was acquired with a lower density than the eastern part (Figure 1.5), which could affect the water detection especially in vegetated area where the pulse may not reach the soil. The required acquisition period was from January to March to limit the foliage effect in order to generate a Digital Terrain Model (DTM). The total of surveying days over the two years is 36 but the time slot was larger than expected, ranging from December to April. The altitude of acquisitions ranges from 1015 m to 1550 m above ground level. The swath is about 1700 m. Comparison of the DTM generated from the LiDAR with reference topographic points reveals a maximum RMSE in Z of 0.25 m. The LiDAR recorded the point elevation as a LAS (LASer file format exchange) file (Figure 1.6).

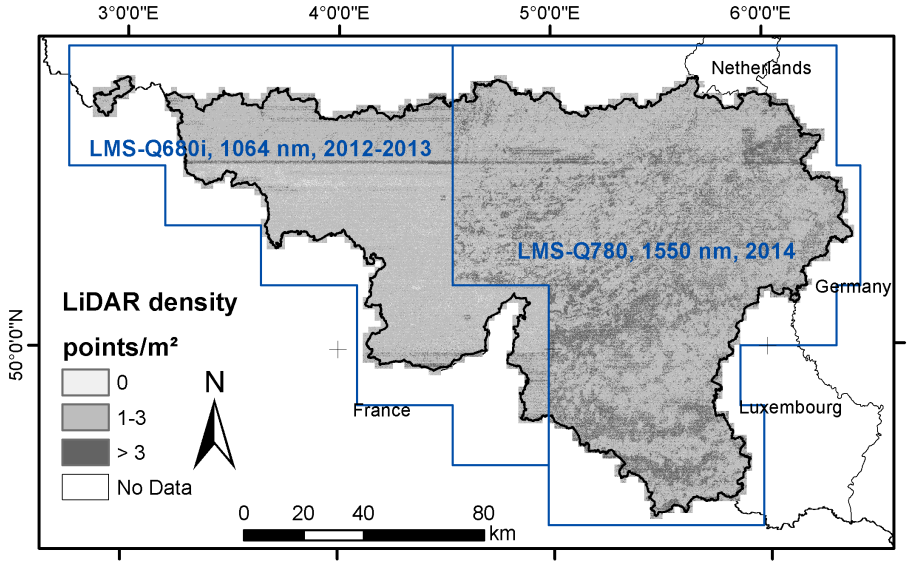

Figure 1.5: LiDAR acquisition was carried out with 2 different sensors. The LiDAR pulse density is heterogeneous and varies from 0 to more than 3 pulses/m^2. The western part was acquired with a lower density than the eastern part, which could affect the water detection.

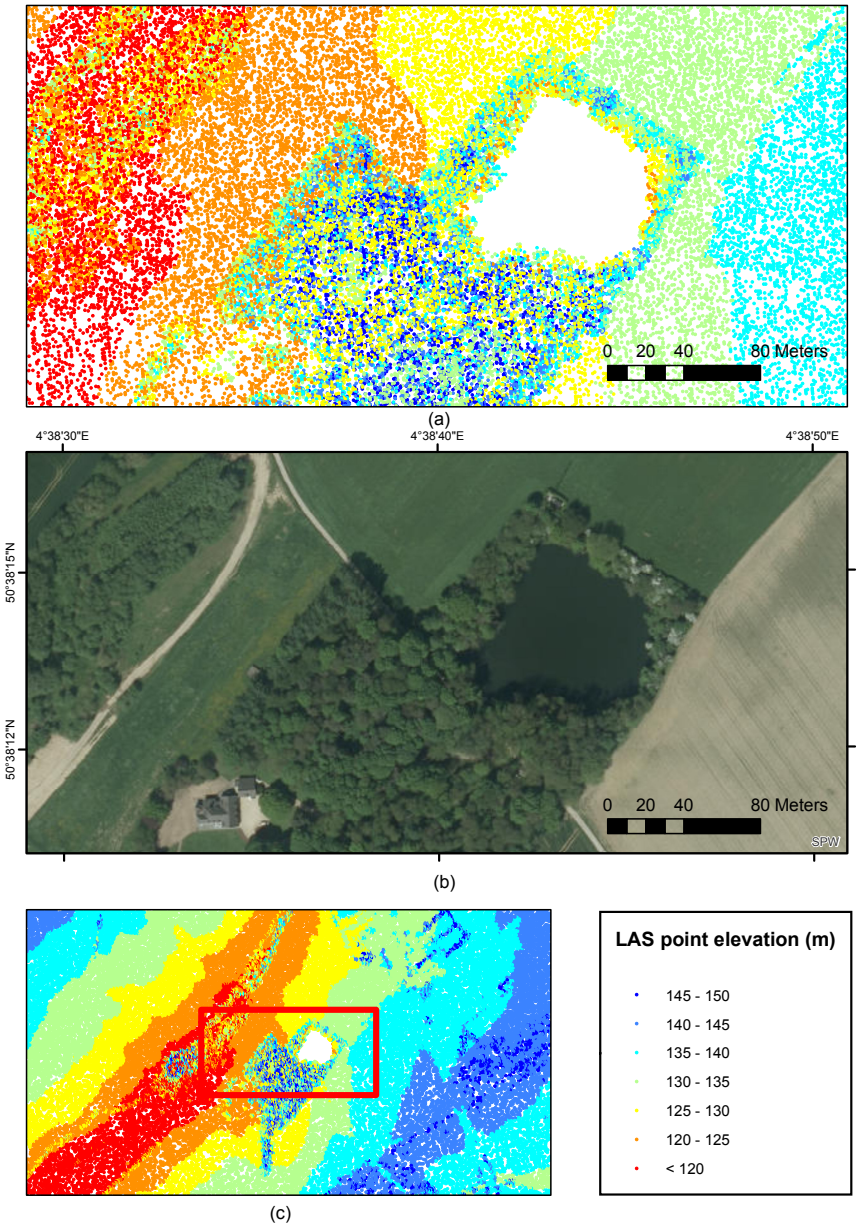

Figure 1.6: Rural area with roads, pasture, fields, forest and building: (a) LiDAR LAS point elevation and (b) the aerial photos. The (c) shows the LAS point with a smaller scale showing in red the location of the figure (a). The water body usually absorbs the laser pulse resulting in no elevation point.

1.4.2 Decreasing local target feature heterogeneity

The local heterogeneity on the aerial photos was addressed by two methods (Figure 1.1 lower half, box 2). First, shadows were modeled using a Digital Surface Model (DSM) and the sun angle associated with each aerial photos. These estimates are then used to remove shaded pixels from the water body delineations. After confirming the presence of a water body on the historical water body vector map, each water body was sampled. From this sample, the shaded points were removed along with outliers by means of an iterative trimming.

Neighborhood effects: shadow estimation

Xie *et al.* (2016) indicates that no existing water index can extract water information while at the same time suppress the false alarm of shadow. Indeed, benchmarking reveals that the shadow seen in the aerial photos was frequently misclassified as water. This was particularly true in this study as the contrast in the low reflectance values was poor and as the sun vertical angle was frequently close to 30°, resulting in frequent large shadows.

To tackle this shadow problem, a geometric shadow estimation is proposed. The approach proposed consists in shadow modeling using information of sensor, light source and geometry of observed objects. This approach determines the location of shadow precisely but geometry of scene and light sources must be know which could be restrictive (Shahtahmassebi *et al.*, 2013). In the same way as proposed here, other study have used laser data to model shadow over high resolution remote sensing imagery (Nakajima *et al.*, 2002; Zhan *et al.*, 2005; Dare, 2005). In this study, first, the azimuth and vertical sun angle were calculated using the acquisition time of the photos. Second, a DSM along with the sun angle makes it possible to predict the geometric projection of the shadow. The sun elevation and azimuthal angle were calculated from the time and the position of the aircraft during the acquisitions for the 5872 tiles. The 1-m resolution DSM was derived from the first-return of LiDAR data. The tangent of sun elevation angle corresponds to the ratio of the object height on the shadow projection, allowing estimation of the shadow. The algorithm produces a shadow mask.

Within-type diversity

The within-type diversity of water bodies is caused by the chemical component of water and by the sediment of the above surface and may result in very different spectral signature of water, as illustrated in Figure 1.2. The approach proposed to handle this within-type diversity over aerial photos is to use an unsupervised classification with a large number of clusters and then to label the clusters with the highest probability of being water according to a cleaned sampling of the historical water body vector map. The rationale behind this is that using a large number of clusters makes it possible to capture the different water classes and to separate them efficiently. In the subsequent aerial photo unsupervised classification (1.4.3), a representative sampling of points which

reliably lie within actual water body boundaries is needed to label the different water classes. This section describes the three steps required to obtain these points. After a confirmation of the water presence using a water index over the historical water body vector map, a sampling of points is drawn and then cleaned to keep only those points not affected by surrounding elements.

As the historical water body vector map is not up to date, it may contain disappeared water bodies; a pre-confirmation using the Normalized Difference Water Index (NDWI) makes it possible to remove dry water bodies. The NDWI from McFeeters (McFeeters, 1996) used a normalized difference between green and near infrared (NIR) bands resulting in a value for each pixel ranging from -1 to 1 (Equation 1.1). This index was selected as no SWIR band is available in the aerial photography.

$$NDWI = \frac{GREEN - NIR}{GREEN + NIR} \tag{1.1}$$

Defining the NDWI threshold best suited to separate water from land is challenging over large areas as it is known to be valid only locally. Therefore, a method to retrieve automatically the status of the water body was designed. The NDWI thresholds (from -1 to 1 with a 0.01 step) were systematically assessed to separate water from land. The threshold maximizing the number of confirmed water bodies was selected, allowing the removal of disappeared water bodies from the historical water body vector map.

A sampling consisting in 200 random points in each water body with a 1-m minimum allowed distance was drawn with the Create Random Points tool from ArcGIS (ESRI, 2016). The number of 200 was selected in order to characterize the within-type diversity of the water reflectance. The points fallen in shadow (retrieved in section 1.4.2) are removed. All the points with a Normalized Difference Vegetation Index (NDVI) (Tucker, 1979) value greater than 0.2 and a near infrared value greater than 180 (on a 256 values scale) are also removed as those values are unrealistic for water surfaces.

Thirdly, for each sampled water body with at least 50 points, the Mahalanobis distance (Mahalanobis, 1936) is calculated. The Mahalanobis distance is a measure of the distance between a point and a distribution. It is a multi-dimensional generalization of the idea of measuring how many standard deviations away is from the mean of a distribution. The Mahalanobis distance is unitless and scale-invariant, and takes into account the correlations of the data set. The distance between each point and the mean of the value in the six bands of the water body considered (red, green, blue, near infrared, NDVI, NDWI) is calculated with Equation 1.2 described by Richards (2013):

$$D_i = \sqrt{(x - m_i)^T \Sigma^i_{-1} (x - m_i)} \tag{1.2}$$

where D = Mahalanobis distance, i = the i class, x = data with n dimension (where n is here equal to 6 for red, green, blue, near infrared, NDVI, NDWI), Σ^i_{-1} = the inverse of covariance matrix and m_i = the mean vector of a class. An iterative trimming (as already used by Desclée *et al.* (2006); Radoux and Defourny (2010b); Matton *et al.* (2015)) is applied until all the points are in the confidence interval of a Chi-Square law of 95%. The points distant to more

than 95% of the distribution are removed. A new mean with the remaining points is then calculated along with their Mahalanobis distance to the mean. This filtering allows removal outliers and points affected by the local context while taking into account the water spectral within-type diversity (Figure 1.7). The result is a sample of points located on confirmed water bodies for each stratum that will be used in the next section to label the clusters.

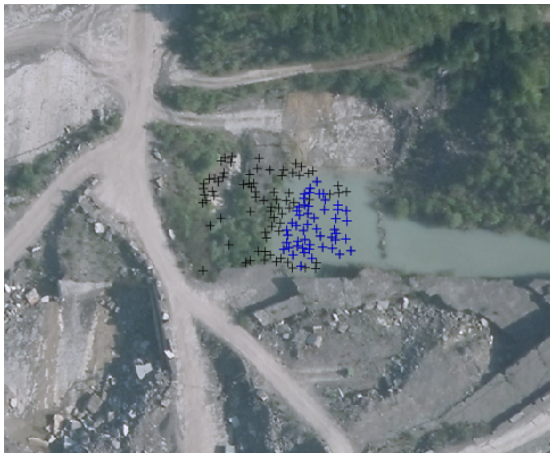

(a)

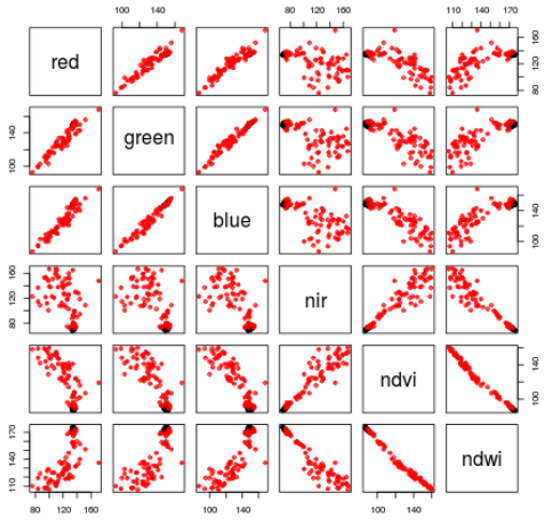

(b)

Figure 1.7: The random sampling consists in 200 points for each water body identified in the historical water body vector map. To avoid using points outside of a water body or with an abnormal reflectance as labelling data, the points are removed if their values have a too large Mahalanobis distance from the mean of the water body. The points in black in the HR photo (a) are removed while the blue are kept. On the scatter plot (b), the points removed are in red while the points kept are in black.

1.4.3 Classification and signal processing

The two different sources (aerial photos and LiDAR) are handled separately (Figure 1.1 lower half, box 3). The first section describes the aerial photos classification, labelling, and post-processing for which the previously presented samples retrieved from the cleaning of an existing vector dataset are used as labelling. The labelling corresponds to the assignment of a land cover class to a cluster resulting from the unsupervised classification. The second section describes how the LiDAR is handled to retrieve surface water.

Aerial photos classification

For each grouping of aerial photo acquisition (defined as stratum in the section 1.4.1), aerial photos are classified into a large number of clusters. In addition to using the red, green, blue and near infrared bands of the imagery, the classification used NDWI and NDVI as providing valuable information regarding vegetation and water.

An unsupervised K-means clustering is applied on each stratum independently over the 6-band file: red, green, blue, near infrared, NDVI, NDWI. The per-stratum number of clusters, which will be used to generate class membership, was set to 500. This arbitrarily large number of clusters was deemed to be large enough to separate the large heterogeneity of the land surface into different clusters. This helps separate water from non-water surfaces, as well as separate visually different types of water bodies. The training set size is 50,000 pixels and the maximum number of iterations for the learning step used is 10,000. The classification was done using Orfeo ToolBox (OTB) on a supercomputing facility. OTB (Inglada and Christophe, 2009) is an open-source C++ library for remote sensing images processing initiated and funded by CNES (French space agency) and enabling state-of-the-art processing of large images.

For each of the 36 stratum, the frequency of clusters corresponding to water in the cleaned sampled points of the historical water body vector map obtained at the section 1.4.2 is then computed. This permits to label the corresponding clusters as water or land.

A number of post-processing steps then permits the reduction of artefacts and commission errors. First, the shadow (retrieved at section 1.4.2) and buildings from ancillary data are removed. Second, a sequence of mathematical morphology operations realized with the Binary Morphological Operation algorithm from OTB (Inglada and Christophe, 2009) is applied: erode (1 m), dilate (3 m), erode (3 m) and dilate (1 m). The aim of those operations is to preserve edges and shapes as much as possible while removing artifacts. These morphology operations are generic tools widely used in the image-processing community. In this study, the first 1-m erosion removes lonely pixels while the closing operation (3-m dilate followed by 3-m erode) makes it possible to fill the gaps on water bodies. Finally, the last 1-m dilate counterbalances the first erode operation. Those filters thus have a positive effect on the results by removing lonely pixel artifacts and by filling gaps in the water bodies. However, the morphological operations have a negative effect on the results by removing

every lonely pixel (water bodies of 1 by 1 m are lost) and by filling 3 by 3 m gaps that are not gaps (islands smaller than 3 by 3 m).

Finally, a raster mosaic is built with all the strata using GDAL (OGC, 2015) and is then converted without simplification into vector data in order to update the existing vector dataset.

LiDAR signal processing

Next, the framework derives an alternate set of water body delineations using an entirely different source of data, LiDAR. The LiDAR signal is most of the time either fully absorbed by the water surface or lightly reflected with Lambertian reflection. The potential presence of water is thus indicated by a low return intensity or by the absence of return. A caveat when using LiDAR to detect water is that other surfaces also absorb the LiDAR beam such as dark roofs (shingle or roofing). Additionally, forests with heterogeneous canopy height trap the beam returns. Vegetated part of wetlands and roads can also absorb most of the signal and thus are frequently confused with water. Moreover, the LiDAR returns over water could be specular. The return intensity may be maximum when the beam is reflected specularly over water, improving omission of the water bodies.

In the current study, the LiDAR data were processed separately for the eastern and western strata (Figure 1.5). For each stratum, the LAS (Figure 1.6) data are extracted as two different rasters. (1) First, the LAS layer was converted to raster selecting the cells designated as water by the pre-classified water to a 1-m raster *water layer* raster using a Binning Maximum Simple interpolation (algorithm from ESRI (2016)). This flag is obtained by thresholding small intensity values of the last echo of the LiDAR pulse. The thresholds were defined by extracting the frequency histograms of the intensity to split visually the intensity values between water and no-water. The threshold varies according to stratum as the power of the LiDAR used differs. (2) Second, the LiDAR intensity was also extracted using the *Binning Maximum None* interpolation (algorithm from ESRI (2016)) into a 1-m resolution raster to retrieve a *no data layer* indicating the location where the pulse was fully absorbed. This second layer is highly contaminated but contains a lot of water bodies not present in the first layer. These two layers are then combined and most of the artefacts are removed with a morphological mathematics operation realized with the Binary Morphological Operation algorithm from OTB (Inglada and Christophe, 2009) with the following sequence:

- Binary union of the *water layer* and the *no data layer* is eroded (3 m), and dilated (3 m). This removes most of the artefacts but will remove small water bodies.
- A recombination of the resulting layer with the *water layer* allows recovery of small water bodies lost in the previous steps. The resulting layer is then dilated (2 m), eroded (3 m) and finally dilated (1 m).

- This sequence is followed by the removal of the remaining buildings using ancillary data (Hallot and Billen, 2013). As the building ancillary data are not up to date, some building may remain.

The resulting raster is then transformed into vector.

1.4.4 Combination and map update

Because the two new maps of water bodies have some degree of disagreement, they are blended using the following workflow illustrated in Figure 1.8 (general outline, see Figure 1.1 lower half, box 4). If a water body is detected on both the aerial photo classification and the LiDAR, the confidence of having a water body is higher. The LiDAR-detected water bodies have more accurate edge as the pulse may go through the canopy to reach the water. The geometrical union of the aerial photo classification layer and the LiDAR layer gives a convergence of the detections by summing the occurrence (detection occurrence number: 0, 1, 2). The layers are then combined to prioritize the update in 3 successive layers (A, B, C) facilitating the update while taking the best contours as described in Figure 1.8. The Layer A contains the water bodies detected by both the LiDAR and aerial photos with the contour of the LiDAR. Layer B contains the remaining polygons detected by the LiDAR only. Layer C contains the remaining polygons detected by the aerial photos classification.

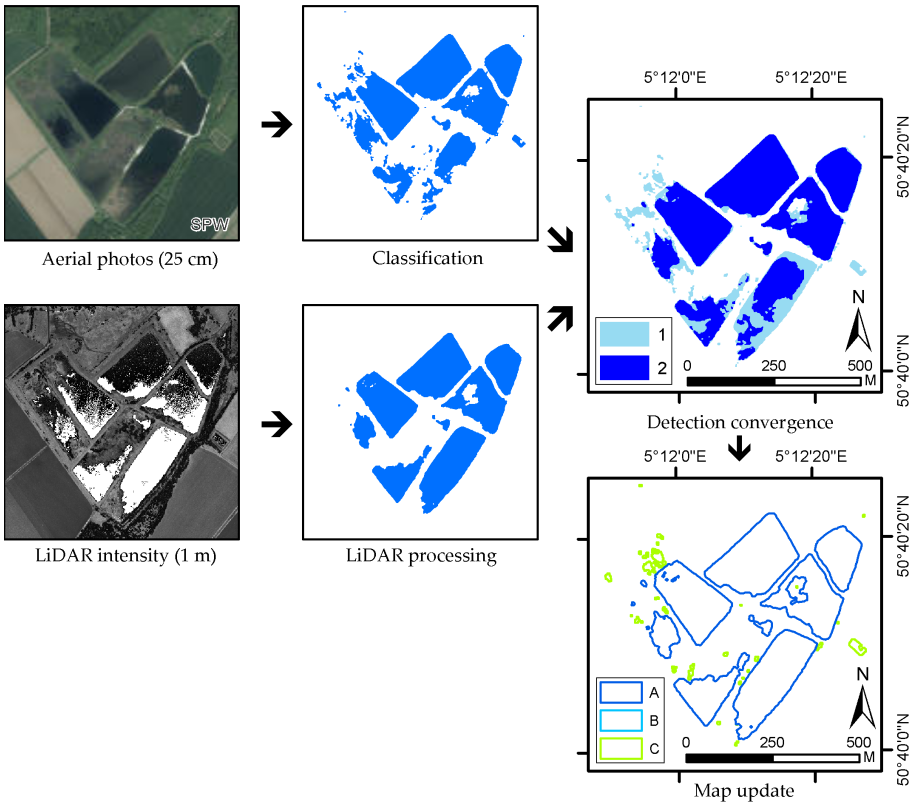

Figure 1.8: Combination of the two data sources via union of the polygons. From this union, the detection convergence is calculated (detection occurrence number: 0, 1, 2). Three successive layers are then created (A, B, C) to facilitate the update. Layer A corresponds to the contour of the LiDAR intersecting with a convergence value of 2. This layer thus contains fewer errors and the shape is better. Layer B is the remaining 1-m LiDAR not taken in Layer A. Layer C consists in the remaining polygons which are not intersecting Layer A and Layer B.

1.4.5 Validation

Validation dataset

After the merging of the dataset in section 1.4.4, the results are evaluated. The validation dataset is based on a random sampling of the aerial photos acquisitions stratified on the years (Figure 1.9). In total, 16 zones of 5 by 5 km were used (8 for 2012 and 8 for 2013). In those extracts, the water bodies and their extents were manually delineated by 2 operators and are considered as ground truth. The area sampled represents 2.5% of the total area and contains 1,334 water bodies of which 245 are new and were absent of the historical water body vector map. The validation is based on visual interpretation and includes all the surfaces of water.

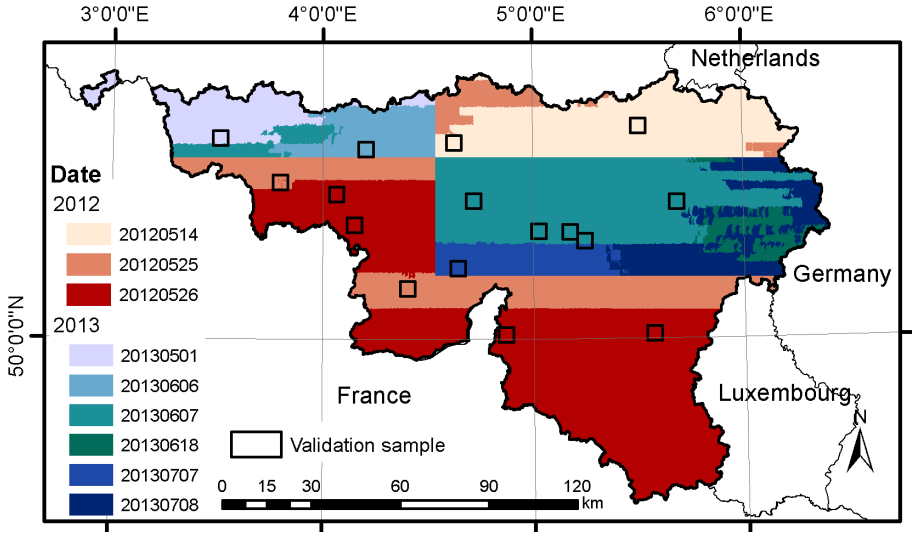

Figure 1.9: A validation dataset of manually-validated water bodies was built by extracting 16 zones of 5 by 5 km sampled randomly (8 in 2013 and 8 in 2014). The color represents the acquisition dates: red tones for 2012 and blue tones for 2013.

Quality indices

The quality evaluation relies on the *detection efficiency* and the *detection cost*. These indices were defined as they were relevant in the applied case presented in the study where the classical user and producer accuracy are not suited.

The *detection efficiency* is described in Equation 1.3:

$$Detection\ Efficiency = \frac{N_{detected}}{N_{real}} \tag{1.3}$$

where $N_{detected}$ corresponds to the number of water bodies detected and N_{real} corresponds to the number of water bodies in the validation. This gives an information about the omission of the resulting map.

The *detection cost* is described in Equation 1.4:

$$Detection\ Cost = \frac{N_{toreview}}{N_{real}} \tag{1.4}$$

where $N_{toreview}$ corresponds to the number of polygons to be reviewed by the operator. This number corresponds to all the polygons of potential water detected by the framework including wrongly detected water bodies. The detection cost gives a quantitative information of the work for an operator to review the map obtained by the framework and gives an information about the commission error.

Those two evaluations are calculated on Layer A, B, C and on the total layer for different area group of water bodies: 25-50 m^2, 50-100 m^2, >100 m^2 and all size together.

1.5 Results

1.5.1 Mapping observation conditions: homogeneous groupings of data acquisition

As described previously, the strata are defined to remove effect-from-observation heterogeneity first for aerial photos and then for LiDAR.

First, for aerial photos, the strata are defined by the combination of the same camera, the same date and the same acquisition time. The results are 36 zones of various shapes and sizes shown in Figure 1.10. To highlight the relevance of the proposed stratification for further processing of the aerial photos, Figure 1.11 (a, b, c) shows the water surface NDWI according to camera, date and time respectively. These three parameters influence the NDWI. First with regard to the camera (Figure 1.11 a), the UCXp191 camera has a NDWI value greater than the two other cameras. This higher value is a result of the lower near infrared values recorded by this camera. The second parameter is the acquisition date. Figure 1.11 (b) reveals that although there are only nine acquisition dates (three in 2012 and six in 2013), a seasonality with increasing value through the year is observed. The third effect is related to the acquisitions time and is shown on Figure 1.11 c. The NDWI peaks at 12:00 AM. To explain these variations, Figure 1.11 (d, e, and f) shows NDWI variations (Figure 1.11 d) and their components if we consider only one camera (e.g. UCXp191) to remove the "camera" effect. The green (Figure 1.11 f) is less sensitive to the time than the near infrared (Figure 1.11 e). The NDWI values peak at 12:00 AM and then decrease. This is explained by the near infrared decreasing to reach its minimum at 12:00 AM. The green is higher at 7:00 and 8:00 but then stays relatively stable throughout the day. To conclude, clearly the near-infrared values reach their lowest level at 12:00 AM resulting in a NDWI peak at this time.

Second, for the LiDAR acquisition, the stratification is done based on the sensor and the acquisition date which correspond to 2 strata represented on Figure 1.5. The western and the eastern parts were acquired at different wave lengths, with different densities, and different powers and will thus be handle separately in section 1.4.3.

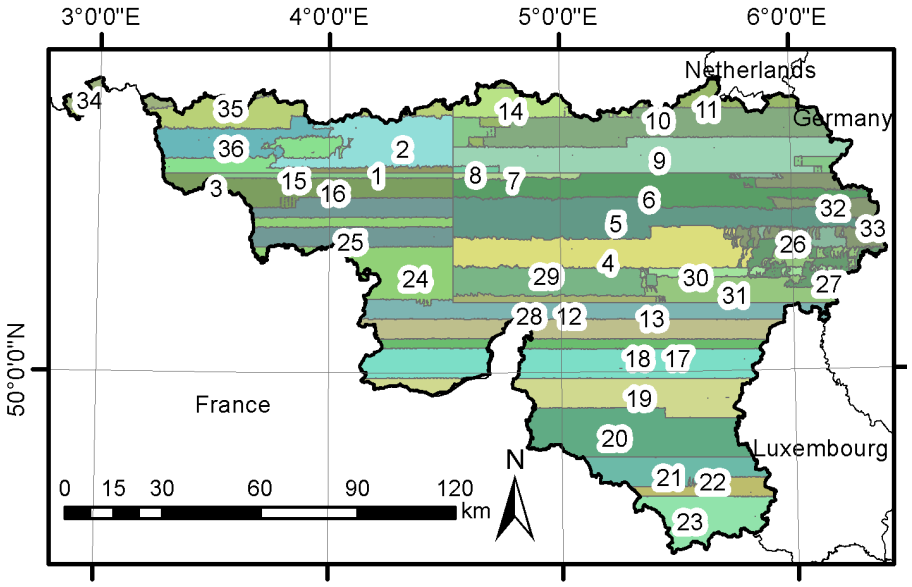

Figure 1.10: Spatial stratification for the aerial photos in 36 strata with homogeneous camera, time of acquisition and date.

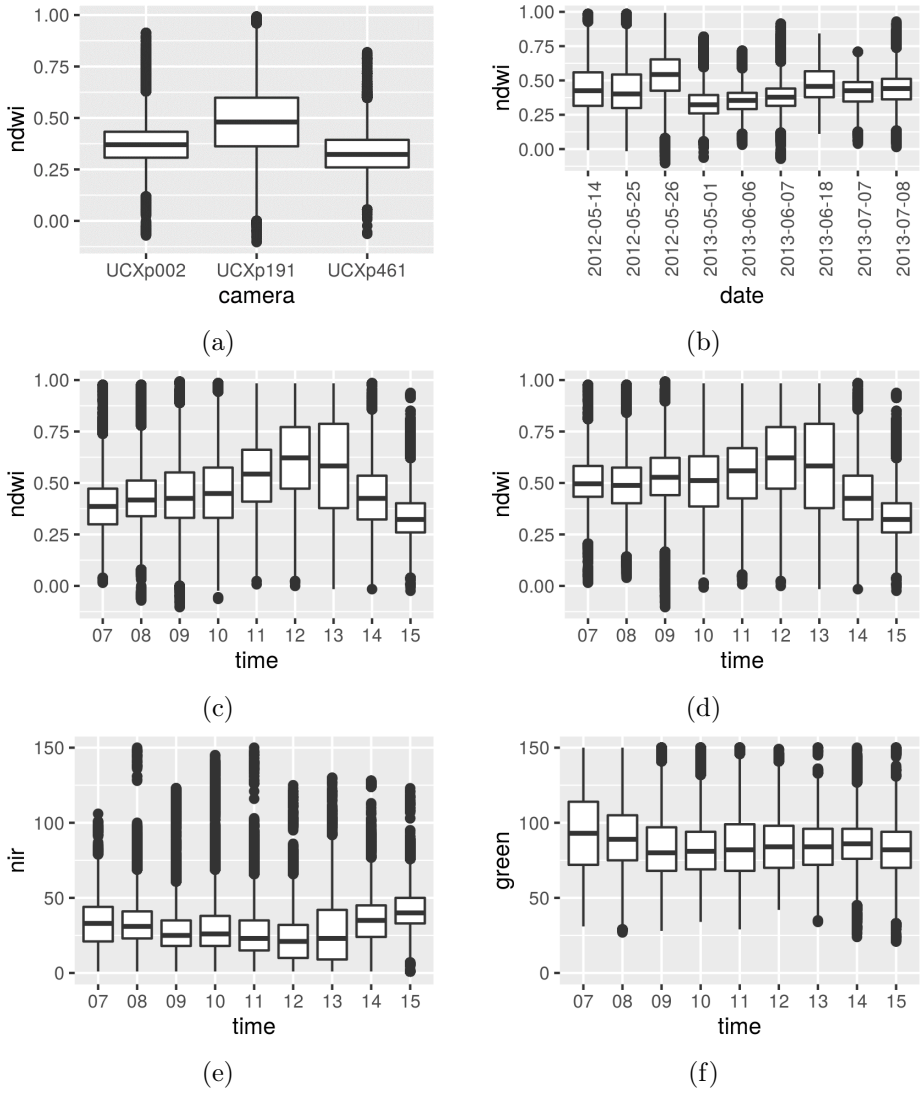

Figure 1.11: Effects of the camera (a), the date (b) and the time (c) of aerial photo acquisitions on the NDWI of surface water. The effects of these 3 variables show the relevance of using these variables to spatially stratify the aerial photos into a homogeneous set. Effect of the acquisition time on the NDWI (d) comes from the near infrared (e) and green (f). Only acquisitions using the UCXp191 camera were used here so as to remove the camera effect.

1.5.2 Local heterogeneity removal

Shadow

The shadow was calculated using a 1-m digital surface model obtained from the LiDAR along with the sun vertical and azimuth angle of the aerial acquisition. The result is a 1-m binary shadow mask where the shadow represents 29.96% of the total surface (Figure 1.12 a). The shadow was computed separately for each of the 5,872 tiles then merged into one layer. Although the calculated shadow corresponds most of the time to the real shadow on the photographs, some artefacts were observed. As LiDAR and aerial photos acquisition differs over time, moving objects between the two acquisitions (cars, boats, new constructions) could lead to ghost shadows as shown in Figure 1.12 b-c. Additionally, some tree shadows are underestimated because of the non-optimal quality of the digital surface model. Additional shadow results (Figure 1.18) are discussed at section 1.6.

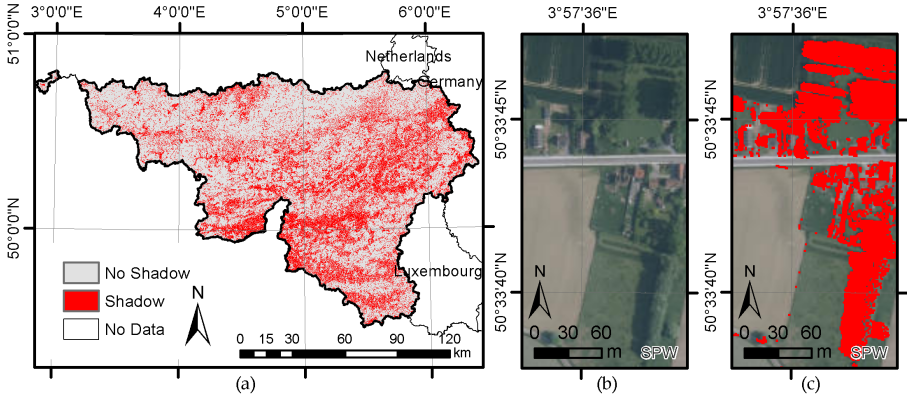

Figure 1.12: Shadow is modeled using a digital surface model and the sun vertical and azimuth angles. Overview over the whole mask (a) and aerial photograph detailed overview example without (b) and with the mask (c).

Random sampling and iterative trimming to remove surface affected by the context

The results of the process of filtering the 200 sampling points for each historically-mapped water body are shown in Figure 1.13. From the 1,508,805 random points, about 1/3 are kept after removing points in shadow and after the multivariate iterative trimming. The result is 474,171 points in 6061 distinct water bodies.

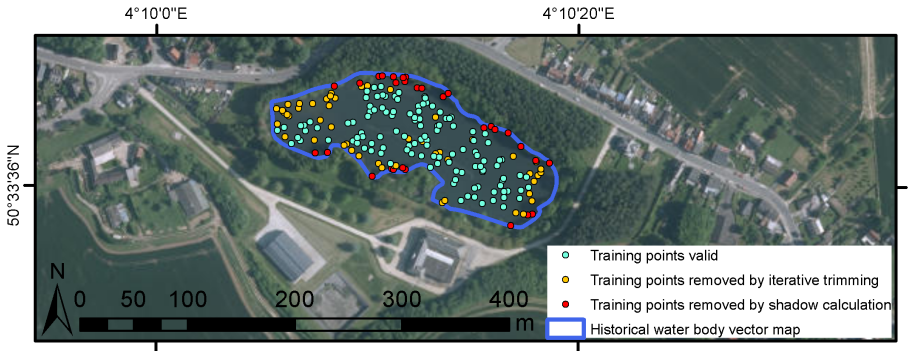

Figure 1.13: The random sampling consists in 200 points (with a 1-m minimum allowed distance) for each water body identified in the historical water body vector map. The points are then filtered out if they fall in the shadow (points in red) or if their values have an excessive Mahalanobis distance from the mean of the water body (points in orange). The remaining valid points (green) are considered to be high-confidence water locations and are used for the subsequent labelling.

1.5.3 Water body classification and signal processing handling intrinsic variability of the target

Aerial photos classification

The K-means 500 clusters classification is applied independently on each of the 36 strata. The aerial photos (Figure 1.14 a) are clustered in 500 clusters (Figure 1.14 b). The mosaic bond-line is slightly visible on Figure 1.14 (a) indicating two different acquisitions with different observation conditions. The classifiers are sensitive to this variability. Figure 1.14 (b) reveals that more than 5 clusters correspond to the same water body. Using a huge number of clusters makes it possible to deal with spectral variability of the water bodies.

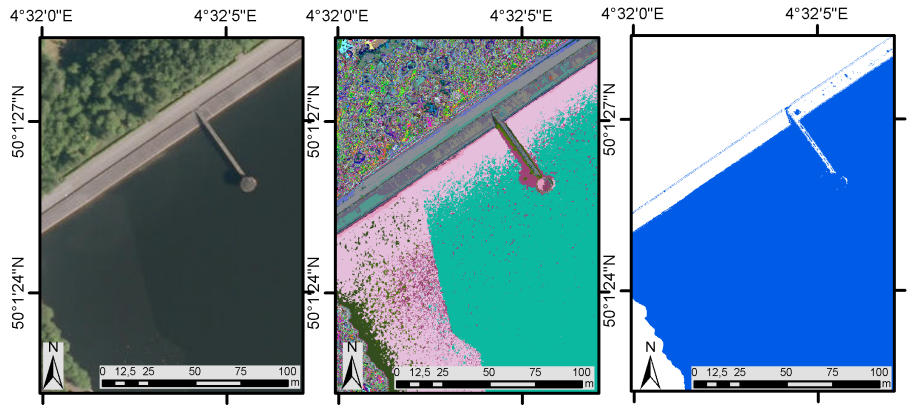

Figure 1.14: Classification results of the aerial photos. Aerial photos (a). K-means 500 clusters classification where each color is a different cluster (b) revealing the intrinsic heterogeneity of the water body, which is composed of more than 5 clusters. All those clusters are then labelled to water or land according to the frequency of the clusters into the training points resulting in a binary result water/no-water (c).

After the clustering of each stratum in 500 clusters, the labelling makes it possible to select the water clusters among the 500 clusters. The clusters of the 474,171 points sampled are extracted separately for each stratum resulting in a frequency for the clusters supposed to be water for each stratum. Each cluster with a frequency superior to 0.5% is then labelled as water. Throughout the 36 strata, the cluster number labelled as water varies from 1 to 26 per stratum with an average of 11 and standard deviation of 5 (Table 1.1). After the labeling, the shadow is removed and the morphological mathematics are applied. Finally, the raster is converted to a vector dataset containing 163,049 features.

Table 1.1: Statistics (minimum, quartiles, mean, maximums) of the stratum areas, the water body numbers, the water body areas, the labelling point numbers and the number of clusters classified as water for the 36 strata.

		Historical water body vector map sampling		**Classification**	
	Stratum (area km^2)	**Water body (number)**	**Water body (area m^2)**	**Labelling points (number)**	**Water cluster (number)**
Minimum	16	2	434.5	116	1
1st Qu.	190	77	1,851.6	5,465	8
Median	407.5	126	2,662.4	9,928	11
Mean	471.3	169	3,198.7	13,171	11
3rd Qu.	701.5	243	4,184.2	18,508	14
Maximum	1127	518	10,817.7	39,953	26

LiDAR signal processing

The LiDAR LAS is processed using a *Binning Maximum Simple* interpolation to obtain the *LiDAR intensity* raster at 1-m resolution, which is in turn converted to *water layer* by thresholding the values (Figure 1.15). On the other hand, the LAS is processed using the *Binning Maximum None* interpolation to obtain *no data layer*. The *water layer* provides the water on which the LiDAR pulses were reflected and then thresholded as water. The *no data layer* provides all the surfaces where the pulses were absorbed or reflected away from the sensor. This layer thus contains many artefacts but also many water surfaces as illustrated in Figure 1.15.

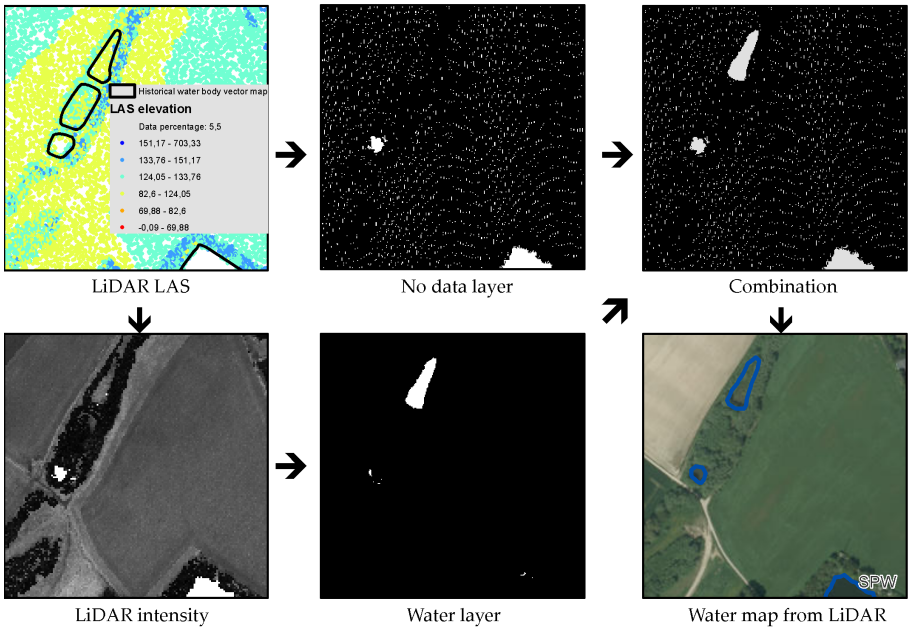

Figure 1.15: Retrieval of water bodies from LiDAR LAS datasets consists in thresholding the low values of the last echoes of the return to obtain a water layer and retrieving the surface where the beam is fully absorbed to obtain the no data layer. The *water layer* and the *no data layer* are then combined with a logical union. The resulting combination is then cleaned using morphological mathematics to finally obtain the water map from LiDAR.

These two layers are then combined along with the application of morphological mathematics in seven steps summarized in Table 1.2. The water surface initially detected decreased by 17.96% to reach 82.04% of the surface of the initial water detection.

The resulting raster is then converted to a 57,921 polygons vector file.

Table 1.2: LiDAR processing sequences with their corresponding surface water variations (percent %, first layer is considered as 100% for comparison)

order	**1**	**2**	**3**	**4**	**5**	**6**	**7**
operation	union of water and no data layers	eroded (3 m)	dilated (3 m)	union with water layer	dilated (2 m)	eroded (3 m)	dilated (1 m)
% surface water	100.00	87.75	88.07	88.10	88.40	88.00	82.04

1.5.4 Combinations and update of the water body map

Finally, the two layers are combined with a union summing detection (1 if detected only by one method and 2 if detected by both methods). The following steps then make it possible to prioritize the update in 3 layers while taking the best contours (Figure 1.16): Layer A (23,583 polygons), Layer B (34,338 polygons) and Layer C (134,542 polygons). Using three layers permits to benefit of the finest contour of the LiDAR. Layer A has the edges of LiDAR that are detected in both LiDAR and aerial photos, Layer B has the edges of LiDAR that are detected only by one method and that do not intersect with Layer A, and Layer C are the remaining polygons. Splitting the map update in those three layers permits to prioritize the review of the result by an operator presenting first high confidence detection and contour from Layer A to less confident detection and contour in Layer C. The 3 layers are finally combined after their revisions.

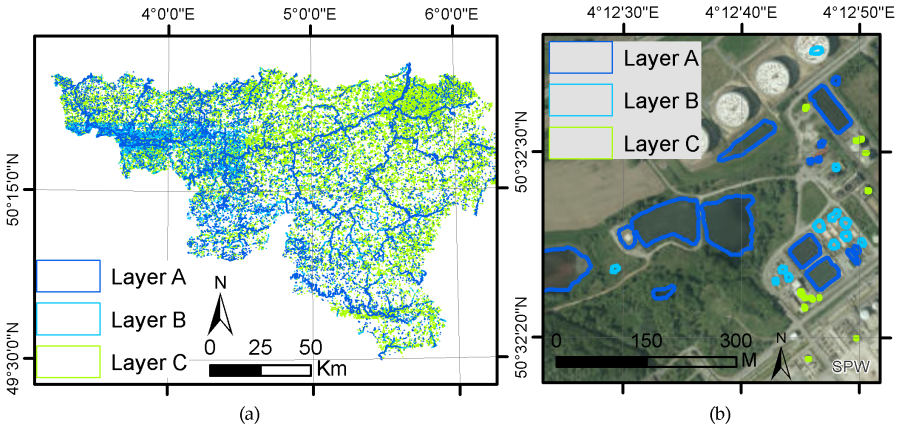

Figure 1.16: Results of the method combination: general overview (a) and detailed example (b). Layer A has the edges of LiDAR that are detected in both LiDAR and aerial photos, Layer B has the edges of LiDAR that are detected only by one method and that do not intersect with Layer A, and Layer C contains the remaining polygons.

1.5.5 Quality evaluation

Although the 3 layers (A, B, C) were finally combined, the quality evaluation is also done for each layer separately for the final results. Table 1.3 shows the results of detection efficiency and detection cost for the 3 resulting layers (A, B, C) for different sizes of water bodies. Among the total number (1,334) of the water bodies identified over the 16 validation zones, 973 were detected (72.93%). The detection efficiency is higher for large water bodies, as 98.57% of the water bodies greater than 100 m^2 are well detected. Figure 1.17 (a, b, c) illustrates good performance of the framework while commission errors greater than 100 m^2 are illustrated in Figure 1.17 (d, e, f). Case d was not detected because it was flagged as shadow and was thus removed. Most of them (such as e and f) have an atypical spectral signature (muddy, eutrophic, cover by vegetation).

When considering only the water bodies smaller than 50 m^2, the detection efficiency decreases to 19.39%. To explain the relative weak result for very small water bodies, a visual check of the 266 water bodies not detected reveals that 62.4% (166) are swimming pools. Two facts explained why the detection of swimming pools is not efficient: (1) swimming pools are most of the time covered by a plastic canvas in Belgium and (2) the sampled points used to label the classification are not drawn in swimming pools, which may have an atypical spectral signature. If swimming pools are removed from the validation dataset, the framework is able to detect 83.3% of the water bodies and 39.02% of the water bodies smaller than 50 m^2.

Table 1.3: Detection efficiency and detection cost for layer A, B and C and for the different size classes of water bodies (25-50 m^2, 50-100 m^2 or greater than 100 m^2). The Layer A contains the water bodies detected by both the LiDAR and aerial photos with the contour of the LiDAR. Layer B contains the remaining polygons detected by the LiDAR only. Layer C contains the remaining polygons detected by the aerial photos classification.

	<50 m^2		**50 - 100 m^2**		**>100 m^2**		**Total**	
	Detection Efficiency	**Detection Cost**	**Detection Efficiency**	**Detection Cost**	**Detection Efficiency**	**Detection Cost**	**Detection Efficiency**	**Detection Cost**
Layer A	6/330 (1.82%)	43/6 (7.17)	27/162 (16.67%)	73/27 (2.7)	540/843 (64.06%)	524/540 (0.97)	573/1334 (42.95%)	638/573 (1.11)
Layer B	16/330 (4.85%)	270/16 (16.88)	23/162 (14.2%)	334/23 (14.52)	132/843 (15.66%)	419/132 (3.17)	171/1334 (12.82%)	984/171 (5.75)
Layer C	42/330 (12.73%)	1878/42 (44.71)	28/162 (17.28%)	626/28 (22.36)	159/843 (18.86%)	671/159 (4.22)	229/1334 (17.17%)	2148/229 (9.38)
Total	64/330 (19.39%)	2191/64 (34.23)	78/162 (48.15%)	1033/78 (13.24)	831/843 (98.57%)	1614/831 (1.94)	973/1334 (72.93%)	3770/973 (3.87)

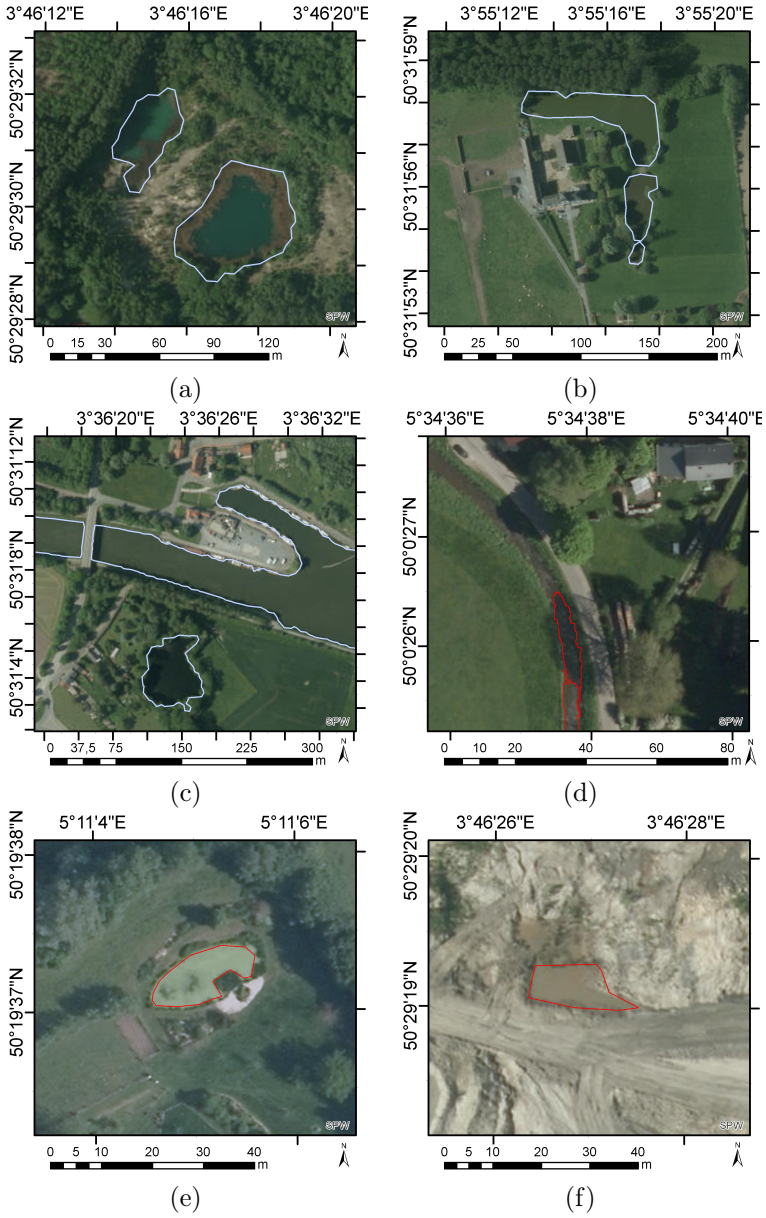

Figure 1.17: Cases (a), (b), (c) show the good performance of the detection in different contexts. Case (a) shows how the riparian zone is well detected thanks to the LiDAR. Case (b) shows well detected green water bodies with shadow of the trees. Case (c) shows the good detection performance for a stream with shadow from a bridge. Cases (d), (e), (f) show examples of water bodies greater than 100 m^2 not detected by the proposed framework. Case (d) is not detected because the shadow is flagged and removed. Water body can be not correctly detected because of the atypical color caused either by vegetation (e) or by sediment load (f).

1.6 Discussion

This study combines hyperspatial data sources of different types taken with heterogeneous observation conditions over large areas (17,000 km^2). The framework and its components are here discussed along with their limitations and perspectives for future research.

In this framework, a decision level fusion combining the results from multiple source is proposed. By managing the heterogeneity of the data source separately through the stratification via the observation conditions mapping as well as the removal of surface affected by local heterogeneity, an innovative and generic framework usable with other platforms and for other thematic maps was proposed. Clearly the proposed framework was driven by available data. A possible improving of the framework it to make it more generic by including other data sources such as hydrological network and soil map.

This research reveals the importance of managing the local neighborhood effects of the target, especially for shadow as this covers about 30% of the whole area of the study. Up to now, there has been no easy and effective method dealing with shadow at hyperspatial resolution over large areas, especially when the land cover target class is absorbing most of the visible spectra such as in water or urban areas (Dare, 2005). The confusion between shadow and water is an enduring problem for high-resolution images (Nath and Deb, 2010). Figure 1.18 represents red, green, blue, near infrared, NDVI and NDWI variables in shadow and not shadowed part of water bodies. This highlights the difficulty to separate shadow from band or index. Indeed, no existing water index can extract water information while at the same time suppressing the false alarm of shadow (Xie *et al.*, 2016) as the values are too close. This problem increases while going through hyperspatial resolution as small objects bring shadow not visible at coarser resolutions. The shadow modeling approach proposed in this study was possible because the geometry of scenes and light sources were known, however similar approaches were already proposed in former studies (Nakajima *et al.*, 2002; Zhan *et al.*, 2005; Dare, 2005). Finally, this study reveals that the need of precise and up-to-date DSM is critical for future studies as it is a prerequisite to model shadow.

Among the data used to map water, the framework proposes the classification of aerial photos. Each 25-cm pixel has 256^6 combination of values possible as 6 bands (red, green, blue, near infrared, NDVI and NDWI) are available with values ranging from 1-256. The proposed K-means clustering permits to reduce the dimension of the data from 256^6 to 500 clusters in order to better estimate the frequency. The arbitrary choice of 500 clusters is quite unusual when considering the literature because there is a risk of overfitting with a too large number of classes. Overfitting could jeopardize generalization of the classification to broader scale. In the current study, the clustering and the labelling are applied locally on each stratum which makes the overfitting on local stratum almost desirable to characterize the local spectral heterogeneity of the water bodies. There is no a priori method to evaluate the ideal number of clusters. A possible way to estimate the optimal number of clusters for future study is to iteratively classify the data with a varying cluster number and

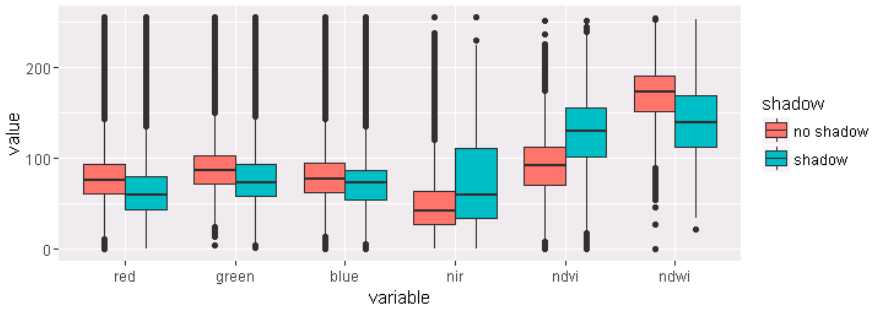

Figure 1.18: Red, green, blue, near infrared, NDVI and NDWI values from a water body sampling. The sampling consists in 200 random points in each water body with a 1-m minimum allowed distance. This corresponds to 1,5 million of points sampled among which 27.5% were in shadow and 72.5% were not in shadow. This shows that those 6 variables do not allow to separate shadow from no shadow.

compare the validation results at each step. In addition to the clustering, the sampling number and location in the historical water body vector map is crucial for a correct labelling of the clusters. In this study, 474,171 points in 6061 water bodies were used while there are about 40,000 water bodies in the study region. First the existence of water bodies in the historical map is confirmed. Then a 200-point sampling with 1-m minimum distance is trimmed to remove outliers. At the end of the process, small and heterogeneous water bodies could be discarded from the labelling points and therefore limit cluster labelling of atypical water bodies and thus their detections. As an illustration, after the trimming of the data, the smallest water body sampled is 434.5 m^2 (Table 1.1), this could explain the limited performance for water-body detection smaller than 100 m^2. Another limitation of the approach is the heterogeneity of the stratum areas. Among the 36 strata, the average area is 471 km^2 but the smallest covers only 16 km^2 (Table 1.1). This small stratum has a limited number of water bodies for the sampling and only 116 labelling points are available while an average stratum has about 13,000 points. In future research, too small stratum should be re-aggregated with their neighbors. Research on labeling points distribution with relation to the size and the heterogeneity of water could potentially improve the results. In addition to the cluster number and the labelling points, the super-computing facility required to process the data could limit the framework usefulness. A workaround tested, but not described in this study, was to decrease the resolution from 25 cm to 2 m reducing the processing time by a factor 64 and making it usable on a normal computer. The framework was working fine but water delineation was logically not sub-metric. In conclusion, aerial photos classification clustering is a powerful simple method to reduce the dimension of a dataset without a priori knowledge. Its labelling with historical data provides good results as long as the labelling data are well distributed and representative of the local water bodies. Future researches should focus on improving the robustness of the sampling used for labelling especially for very small water bodies.

Combination of source of data is particularly suited as it has already been highlighted in many researches (Wu *et al.*, 2014; Lichvar *et al.*, 2006; Hodgson *et al.*, 2003; Chen *et al.*, 2009; Bork and Su, 2007; Rodríguez-Cuenca and Alonso, 2014; Maxa and Bolstad, 2009; Elaksher, 2008). In particular, the LiDAR is able to penetrate the canopy and is thus more accurate in delineating the water bodies. However, it misses some water bodies as the laser pulse can be reflected. Additionally, the LiDAR pulse density is critical especially in forest area where the water bodies are difficult to detect on the aerial photos and LiDAR. When the LiDAR density falls between 0 and 1 point/m^2 (Figure 1.5), it means that it is not possible to detect water below meter. On the other hand, the aerial photos offer a higher resolution (25 cm) and improve or decrease the confidence of the detection from the LiDAR. The combination of data sources remains a challenge for the remote sensing community and few studies put forward an operational framework for water mapping. The proposed framework is well suited to addressing this challenge.

In this study, morphological mathematics were used for artifact reductions and water gap filling. For both aerial photos classification and LiDAR, the morphological mathematics operations were useful. Their effects on surfaces were outlined for LiDAR with 12.25% surface lost with the first 3-m erosion applied, and a total of 17.96% of surfaces lost after all the steps (Table 1.2). In this study, the rationale was always the same, a 1-m opening operation (erosion followed by dilation) permits to remove lonely pixel artifacts and a 3-m closure operation (dilation followed by erosion) permits to fill the gaps in the water bodies. Those morphological operations result in a limitation of the approach to detect water bodies smaller than 3 by 3 meters. Moreover, islands smaller than 3 by 3 could be removed by filling 3 by 3 m gaps that are not gaps. Future researches on morphological mathematics applications and on the optimal configuration of the kernel size could formalize those operations according to the objective of the study and its landscape structure.

Another option to classify an image is, first, to segment the image into homogeneous objects and, then, to do an object-based classification (Blaschke, 2010). In this study, a preliminary test on the aerial photos resampled from 25 cm to 2 m and using the mean shift algorithm implemented in the eCognition Developer software (Trimble Geospatial) took about 1 month to be segmented (thus about 16 months at 25 cm). Object-based image analysis is a time consuming task in extracting information from large images because most of the segmentation algorithms use the pixel-grid for the initial object representation. However, Csillik (2017) demonstrates that new segmentation methods, such as Simple Linear Iterative Clustering proposed by Achanta *et al.* (2012), an adaptation of k-means clustering for superpixel generation, could provide very good results on sub-metric imagery. According to Csillik (2017), this has the potential to enhance the automation of big remote sensing data analysis and processing, especially when time is an important constraint. Such approach should be envisaged in future researches.

Another point to discuss is the usefulness of hyperspatial resolution with regards to the performance achieved and the lower resolution imagery available. Clearly, as demonstrated in the introduction, having hyperspatial resolution

map is useful for managers, engineers and scientists. However, the framework complexity along with the acquisition period (here almost 3 years) could question the opportunity to use the proposed approach in place of lower resolution available imagery. First, distinction should be made between *detection* which is the presence or absence of water and *delineation* which is the contour of water. This framework focus on delineation and although all the water bodies are not detected with the approach, the ones detected have a delineation at 1-m resolution. The proposed approach detects 98.57% of water bodies greater than 100 m^2 with a sub-metric accuracy delineation. Radoux *et al.* (2016) demonstrates that on the same region, the smallest water body detectable with the 10-m Sentinel-2 bands was 11-m diameters. Thus even with the finest Sentinel-2 bands, it is not possible to detect water bodies smallest than 100 m^2. The framework is able to detect 48.15% of the water bodies smaller between 50 and 100 m^2 with a 1-m delineation. Besides, this framework was used by the administration to reduce their manual update work as they need to map water bodies from 25 m^2 as they are eligible for subsidies in the context of the CAP. Future researches improving estimation of the water contour accuracy could help to quantify and compare proposed approaches.

Although the amount of manual mapping work decreased sensibly as most of water bodies are well delineated with a precision higher than 1 m by the framework, this study also reveals that an operator is still valuable to check and validate the water bodies. For water bodies greater than 100 m^2 the operator was able to use the resulting layers, obtaining a 98.57% rate of detection success. For smaller water bodies ($<$50 m^2), the efficiency decreases to 39.02% if the swimming pools are not taken into account.

The validation scheme used in the study, *i.e.* a stratified random sampling, provides a valuable assessment of the results. However, as the stratification is based on the aerial photos acquisition year, the stratification doesn't really provide complementary information for the validation. Therefore, future validation scheme should not be necessary stratified but only random sampling. Moreover, based on photo interpretation of aerial photography, the validation dataset quality could be impacted by the quality of the aerial photos which also impact the classification results. Therefore, an independent ground truth sampling would be more appropriate even it is difficult to obtain. In addition to the validation of the water presence, a validation of the contour could also be particularly interesting for future researches especially at hyperspatial resolution.

The framework could be applied to data acquired by aircraft, satellite and drones. The recent digital revolution in aerial photography brings satellite methodologies to aerial photos. The proposed framework addressed this challenge over large areas. After questioning some commercial satellite data providers, it appears that currently few commercial providers are able to meet the acquisition specifications – spatial resolution below the meter, "cloud free" data, acquisition between 1st April and 1st July (to capture the start of the crop growing season). Up to now, commercial satellites such as Deimos-2 and WorldView-3 have a panchromatic resolution below 1 m at nadir but are not able to cover large areas with the acquisition specifications. The proposed

framework is suited to handling heterogeneous satellite mosaics that will be available on larger areas in the future.

Additionally, the proposed method could also be applied to Unmanned Aerial Vehicle (UAV) imagery processing. Shahbazi *et al.* (2014) reviewed UAV applications and water bodies play a large part as UAVs were used for mapping aquatic species and characterizing water bodies. Aerial remote sensing and UAV have similar constraints. In the light of the application reviewed (Shahbazi *et al.*, 2014), the radiometric inconsistency of images should be adjusted, and geometric errors need to be duly rectified to produce satisfying results. The proposed framework could reduce this work of image adjustment by mapping the acquisition conditions as a pre-requisite to classification.

The logical next step after the water body mapping is its type identification. Few studies have proposed robust methods for this identification mainly because the diversity of water type is high and their type definition is context dependent. As an example, after water body mapping, Huang *et al.* (2015) used a set of geometrical and textural features for identifying the water types (*e.g.*, rivers, lakes, canals, and ponds) from urban high-resolution remote-sensing images. However the results are context specific (Wuhan and Shenzhen) and should be refined to be more generic. Further researches on water type identification should be envisaged.

1.7 Conclusions

The paper describes a framework and its application to handling the heterogeneity of remote sensing platforms (UAV, aircraft, satellite), sensors (optical, LiDAR, SAR) and observation conditions (VZA, SZA, date). The proposed framework further deals with the water within-type diversity (morphology, origin, composition) and with the neighborhood effects (shadow) target water bodies. Such framework is suited to mapping inland water bodies over large areas with hyperspatial resolution. The proposed framework detects 83% of the water bodies – if swimming pools are not taken into account – and more than 98% of those water bodies greater than 100 m^2, with an edge accuracy below 1 m over large areas. This study opens avenues for operational application over regional scale.

Chapter 2

Water body sub-decametric detection potential of Sentinel-2

Abstract. In the previous chapter, we describe a framework to detect small water bodies at sub-metric resolution with aerial sensors. While aerial acquisitions are one-shot-planned campaigns, satellites are orbiting the Earth and delivering imagery on a regular basis. Moreover, satellites could provide synoptic view of the Earth and thus allow mapping of wider extent. This chapter focuses on the detection of decametric and sub-decametric water bodies with satellite imagery. So far, however, very small ponds (smaller than 1000 m^2) could be difficult to detect with HR satellites. In a collaborative study*, a methodology was developed to characterize the minimum sub-pixel feature detectable by the promising recently launched first Sentinel-2 satellite which is compared with a spectrally similar sensor (Landsat-8) and a spatially similar sensor (SPOT-5). A method to empirically estimate the minimum object size for an accurate detection of a set of structuring foreground/background pairs was developed. The framework combines a spectral separability analysis and an empirical Point Spread Function (PSF) estimation. The results obtained with regards to water detection suggest that isolated sub-pixel ponds are detectable using 20-m Red-Edge and SWIR Sentinel-2 bands with a minimum size of 16.7 m and 19.5 m respectively bur are not detectable using 10-m band such as NIR which is not able to detect pond with a diameter smaller than 12.5 m. If linear objects such as rivers are considered, the 10-m NIR band permits the detection of standing water of 6-m width.

In the paper in which each author contributed equally, my contributions were on the empirical PSF estimation and on the water bodies thematic. Only the results from the paper concerning water bodies will be presented here. First, the methodology used will be summarized followed by the results with emphasis on

*Radoux, J., Chomé, G., Jacques, D.C., Waldner, F., Bellemans, N., Matton, N., Lamarche, C., d'Andrimont, R. and Defourny, P., 2016. Sentinel-2's Potential for Sub-Pixel Landscape Feature Detection, in *Remote Sensing*, 8(6), p.488.

the spatial resolution and the minimum mapping size of water bodies. Finally, additional results, not presented in the paper, showing the impact of the PSF on a Sentinel-2 classification provides an illustration of the paper findings for water bodies.

2.1 Introduction

In the introduction of this thesis, the importance of water bodies mapping was depicted extensively. This is particularly true for ponds smaller than 1000 m^2 as they have major role in carbon sequestration. Carbon concentrations were indeed founded greatest in small ponds probably due to their high perimeter to surface ratio (Holgerson and Raymond, 2016). Moreover, a large number of species rely on the presence of small water bodies for their life cycle such as fishes, batrachians, dragonflies... The creation of water bodies in rural areas is therefore encouraged by institutions through various policies such as the European Common Agricultural Policy (CAP). In the context of the greening of the European CAP that supports agro-environmental elements, a pond is eligible for subsidies if its extent area is wider than 25 m^2 (SPW, 2012). Additionally, small ponds are dynamic in time and could also be quickly filled or invaded by vegetation which implies a need of monitoring in time. Yet, so far, very small ponds cannot be detected on traditional satellite imagery as they can form a continuum with wetlands making the two difficult to distinguish (Downing *et al.*, 2006).

However, satellite remote sensing has entered a new era with short revisiting period operational satellites acquiring free, open, global and systematic high-resolution visible and infrared imagery. Landsat-8 and Sentinel-2A acquisitions are available from March 2013 and November 2015 respectively. Thanks to its state-of-the-art specifications, Sentinel-2 (Malenovsky *et al.*, 2012; Drusch *et al.*, 2012) was designed for a variety of land monitoring applications including water detection (Du *et al.*, 2016). Currently only Sentinel-2A is operational while a second similar satellite, Sentinel-2B was put in orbit in 2017 but has not provided nominal imagery yet (Table 2). Sentinel-2 orbits the Earth on a 786-km height sun-synchronous orbit with a revisit cycle of 10 days which will be reduced to 5 days when the second satellite will be in operation. Thanks to its Multispectral Images (MSI) payload onboard, Sentinel-2 provides 13 spectral bands from 10 to 60 meters on a 260-km swath (Table 2.1). Landsat-8 orbits the Earth on a 705-km height sun-synchronous orbit with a revisit cycle of 16 days. Thanks to its Operational Land Imager (OLI) payload, Landsat-8 provides 9 spectral bands at 30-m resolution (Table 2.1). Those two payloads offer similar spectral bands with a good potential for water mapping especially with the two NIR and the two SWIR bands. However the spatial resolution is higher for Sentinel-2 than for Landsat-8 making those sensors difficult to compare from a spatial point of view. Fortunately, SPOT-5 (Take5), an experiment consisting in lowering the end-of-life SPOT-5 satellite by 3 kilometers to put it on a repeat cycle orbit similar to Sentinel-2, allowed to retrieve 5 months of image spatially similar to Sentinel-2 over selected sites in 2015 (Hagolle *et al.*, 2016). Thanks

to its High Resolution Geometric (HRG) payload, SPOT-5 provides four bands, if we exclude the panchromatic band, with a spatial resolution ranging from 10 to 20 meters (Table 2.1). The Sentinel-2A sensor could then be compared to Landsat-8 for spectral aspect and to SPOT-5 for the spatial component. The spatial and spectral specificities of those three satellites are summarized in the Table 2.1.

Table 2.1: Name, spectral range (nm) and spatial resolution (m) of the corresponding Sentinel-2 MSI, Landsat-8 OLI and SPOT-5 HRG bands. The asterisk indicates bands that are not assessed in this study such a band used for aerosol, cirrus, water vapor, thermal bands retrieved from the Landsat-8 Thermal Infrared Sensor (TIRS) payload as well as the panchromatic bands.

Sentinel-2 MSI		**Landsat-8 OLI**		**SPOT-5 HRG**		
Band [m]	**Range [nm]**	**Band [m]**	**Range [nm]**	**Band [m]**	**Range [nm]**	**Name**
B1 * (60)	443 ± 10	B1 (30)	440 ± 10			Aerosol
B2 (10)	490 ± 32.5	B2 (30)	480 ± 30			Blue
B3 (10)	560 ± 17.5	B3 (30)	560 ± 30	B1 (10)	545 ± 45	Green
B4 (10)	665 ± 15	B4 (30)	650 ± 20	B2 (10)	645 ± 35	Red
		B8 * (15)	590 ± 45	PAN (5)	595 ± 115	PAN
B5 (20)	705 ± 7.5					Red-edge 1
B6 (20)	740 ± 7.5					Red-edge 2
B7 (20)	783 ± 10					Red-edge 3
B8 (10)	842 ± 57.5			B3 (10)	835 ± 55	NIR_{wide}
B8A (20)	865 ± 10	B5 (30)	865 ± 15			NIR_{narrow}
B9 * (60)	945 ± 10					Cirrus
B10 * (60)	1375 ± 15	B9 (30)	1370 ± 10			Water Vapor
B11 (20)	1610 ± 45	B6 (30)	1610 ± 40	B4 (20)	1665 ± 85	SWIR 1
B12 (20)	2190 ± 90	B7 (30)	2200 ± 90			SWIR 2
		B10 * (100)	$10,895 \pm 295$			Thermal 1
		B11 * (100)	$12,005 \pm 505$			Thermal 2

Concerning spatial resolution, some research has already been carried out on mapping or extracting information at finer resolution than the effective pixel size of a sensor. For instance, spectral unmixing methods were developed to determine the fractions of land cover classes within a coarse pixel and downscaling methods, also known as super-resolution or sub-pixel mapping, aim at turning these proportions into a fine resolution map of class labels (Boucher, 2007). In particular, several studies used the spectral mixture analysis for sub-pixel water mapping to detect sub-pixel-scale ponds (Sethre and Rundquist, 2005), to derive a water fraction and flood maps from MODIS (Sun *et al.*, 2011), for sub-pixel lake mapping with MODIS (Ma *et al.*, 2014), to determine the shoreline position at a sub-pixel precision using Landsat (Pardo-Pascual *et al.*, 2012), and for urban sub-pixel water body mapping with Landsat-8 (Xie *et al.*, 2016).

Extensive work has also been carried out to evaluate the minimum spatial resolution to detect small features (Congalton *et al.*, 2002; Lausch and Herzog, 2002; Jensen and Cowen, 1999; Lechner *et al.*, 2009). For example, SPOT-5 imagery at 10 m was found suitable to map small ponds in Senegal (Lacaux *et al.*, 2007). Nonetheless, operational methods to map small landscape elements remain scarce (Thornton *et al.*, 2006). Moreover, as described in the thesis introduction, another potential source of the non-negligible reflectance is the adjacency effect as the water bodies are small and water leaving signal very low compared to the potential signal contamination from the adjacent land.

Pre-launch and on orbit characterization of spaceborne sensors are the first step towards verifying that the technical specifications are met with a focus on calibrating the sensor and assessing the continuity with previous missions (Knight and Kvaran, 2014; James *et al.*, 2014). On orbit characterization covers the spatial and the radiometric performances of the sensor. However, most on orbit radiometric characterizations use calibration data sets, as opposed to natural ground targets (Ron *et al.*, 2015), and spatial characterization uses Earth targets as well as stars and moon shots (Knight and Kvaran, 2014; De Lussy *et al.*, 2012). On the other hand, empirical analysis of new sensors based on natural surface targets provides fitness to use results for future applications. However, most studies with surface targets focus on developing methods and algorithms to extract the most precise and accurate information from a given sensor without looking specifically at the sensor performance. An intermediate analysis level between rigorous calibration/validation analysis and applications optimized for the input data could therefore bring more useful information.

Understanding the detection processes of sub-pixel landscape elements is the key to derive information for natural resources management. In addition, systematic analyses of the sub-pixel discrimination capacity for different landscape features is useful for the scientific community to assess the sensor ability to detect specific thematic features. Hence, the aim of this study is to measure the fitness for purpose of Sentinel-2 for the detection of small spatial objects, water bodies, that play a role in ecological networks. The minimum pixel size of 10 m and the narrow spectral bands selected for their specific response to key land surface properties are indeed very promising. The working hypothesis is that the combination of the spatial and spectral resolution analysis can be jointly used to characterize the Sentinel-2 performances for specific object detection independently of the landscape composition. This study presents a framework that simulates the process of detecting sub-pixel feature pairs by assessing the separability of synthetic mixtures. Additionally, the assessment of the empirical resolution of Sentinel-2 which includes a comparison with SPOT-5 and Landsat-8 also because Sentinel-2 aims at providing enhanced continuity of SPOT and at complementing the Landsat archive (Drusch *et al.*, 2012).

2.2 Methodology and study area

This section summarizes the framework developed to assess the minimum detectable water body object with Sentinel-2. First, the spectral resolution is assessed through pairwise separability analysis. Second, the spatial resolution is characterized via the empirical estimation of the PSF. Finally, the minimum object size detectable with the sensor is retrieved through integration of spatial and spectral components. Those three steps applied on Sentinel-2 MSI are compared with sensors with similar spectral (Landsat-8 OLI) and spatial (SPOT-5 HRG) resolutions respectively.

Spectral resolution. The first step consists in synthesizing the spectral signature of class pairs for different mixture proportion. Those signatures are

based on pure land surface reflectances extracted from satellite acquisitions in the South of Belgium. The acquisition extents of the three sensors are shown in the upper right side of Figure 2.1. Although other interesting and common landscape features were considered for the analysis such as roads, grass strips and small woody patches, only water bodies pairs are presented here (for the other classes see the complete study in Radoux *et al.* (2016)). As ponds are generally found in grassland areas in the considered region, water bodies were paired with grassy background: grassland and pasture. The spectral analysis was performed based on images of Southern Belgium (Figure 2.1). This area embraces a large diversity of fragmented landscapes and therefore is well suited for analyzing mixed pixels of different types. The analysis was performed on the closest SPOT-5 (Take 5) cloud-free acquisition covering Southern Belgium on 4th July 2015. Extreme caution was thus exercised in the comparison among sensors as the state, and thus the spectral response, of the vegetation may have significantly changed during the time interval. Figure 2.1 illustrates the spatial resolution differences of the three sensors of interest when imaging a 30 m wide pond. As the PSF is location-independent, acquisitions over Sacramento (California, USA) in September 2015 were selected (Figure 2.3 (a)). The average field size in Belgium was indeed too small for a proper PSF estimation and data were available for each sensor.

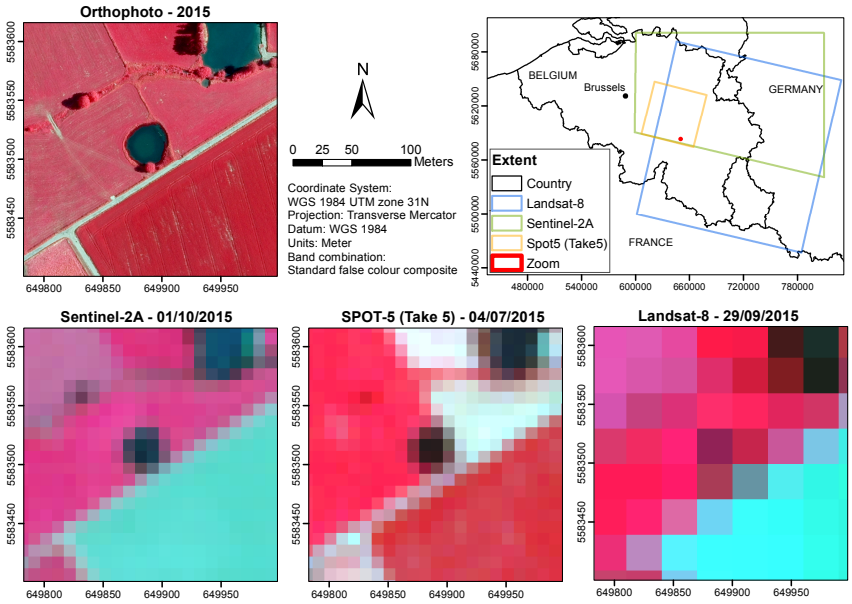

Figure 2.1: Snapshots of an orthophoto (25 cm), Sentinel-2A (10 m), SPOT-5 (Take 5) (10 m) and Landsat-8 (30 m) images of a small pond (30 m × 30 m) surrounded by permanent grassland in the South of Belgium. The four images are presented using the same standard false color bands combination (R: NIR_{wide}, G: Red, B: Green).

For the three sensors, Level-1C products, *i.e.*, top-of-atmosphere reflectances in cartographic geometry, were available for the two selected sites. Sentinel-2 image were obtained during the commissioning phase of the satellite. The geolocation of the provided Sentinel-2 image was evaluated visually and achieved a geometric quality RMSE of approximately 20 m. The images were therefore manually co-registered based on a 25 cm orthophoto of the Walloon region with a first-order polynomial model and resampled with the nearest neighbor method in order to preserve the radiometry of the pixels. Eventually, the RMSE of the co-registration model was 4.9 m. Since atmospherically corrected images are essential to assess spectral indices with spatial reliability and products comparison, level-1C data have been processed to level-2A (top-of-canopy) taking into account the effects of aerosols and water vapor on reflectances. These corrections have been realized using the *Sen2Cor* tool (Müller-Wilm, 2015) for the Sentinel-2 images, *L8SR* algorithm for Landsat-8 images (Vermote *et al.*, 2016) and *MACCS* for SPOT-5 images Hagolle *et al.* (2015). The *Sen2Cor* algorithm uses Sentinel-2 bands for atmospheric corrections whereas the *MACCS* tools rely on US National Centers for Environmental Prediction water vapor, air pressure, air temperature data and Total Ozone Mapping Spectrometer ozone data. The *L8SR* algorithm calculates internally the surface pressure based on the elevation and uses Moderate Resolution Imaging Spectroradiometer (MODIS) Climate Modeling Grid—Aerosol (CMA) product for water vapor, air temperature and aerosol optical thickness estimates, MODIS CMG Coarse resolution ozone product for ozone data. Due to processor constraints, the manual co-registration of Sentinel-2 images have been applied after atmospheric correction.

Second, the separability of the two classes of the pairs were evaluated for a set of spectral bands and for 35 indices frequently used in remote sensing. Among those 35 indices, three indices are specific for water detection : $NDWI_1$ (Gao, 1996), $NDWI_2$ (McFeeters, 1996) and *NHI* (Lacaux *et al.*, 2007). The latter one is the mathematical opposite of the well known *MNDWI* (Xu, 2006) (Equations 2.1, 2.2, 2.3). For brevity, the other indices are not presented here but are described in details in Radoux *et al.* (2016).

$$NDWI_1 = \frac{\rho_{NIRnarrow} - \rho_{SWIR1}}{\rho_{NIRnarrow} + \rho_{SWIR1}} \tag{2.1}$$

$$NDWI_2 = \frac{\rho_{Green} - \rho_{NIRnarrow}}{\rho_{Green} + \rho_{NIRnarrow}} \tag{2.2}$$

$$NHI = \frac{\rho_{SWIR1} - \rho_{Green}}{\rho_{SWIR1} + \rho_{Green}} \tag{2.3}$$

Spatial resolution. The spatial resolution differences of the three sensors considered when imaging a 30 m wide pond are illustrated in Figure 2.1. The most common measure of sensor spatial resolution is the Ground Sample Distance (GSD), also known as the ground-projected instantaneous field of view, which can sometimes also refer to the distance between two adjacent pixel centroids as measured on the ground (Schowengerdt, 2007). However, the spatial quality of an optical remote sensing instrument involves more aspects of the imaging system than the sole characteristics of the pixel resolution (Joseph,

2000). Schowengerdt (2007) provides extensive definitions and examples of aspects of spatial resolution, representing the cumulative result of optical properties of the sensing system. Generally, spatial resolution involves the interaction between the GSD and the PSF, which models the blurring effect due to all elements of the imaging system. The blurring effect of a sensor is characterized by the PSF which can be viewed as the spatial responsivity of the sensor (Schowengerdt, 2007). A plethora of methods were developed to assess the PSF or the direction line spread functions (LSF) pre-launch or on orbit from remote sensing imagery (Schowengerdt *et al.*, 1985; Ruiz and Lopez, 2002; Helder *et al.*, 2004; Pagnutti *et al.*, 2010; Campagnolo and Montano, 2014; Wenny *et al.*, 2015). Following the recommendations of Wenny *et al.* (2015), a transition between bare fields and green crop fields was considered as it offers a maximum contrast, a uniformity, a sharp transition and proper orientation with respect to the satellite orbit (Figure 2.2). Since Sentinel-2 is in a polar orbit at an inclination of 98°, the near-optimal angle for the field boundary orientation is 98°± 8° for along-scan estimations and 8°± 8° for along-track estimations (Wenny *et al.*, 2015). Landsat-8 and SPOT-5 are also on polar orbit with a 98° inclination. The sensor PSF is a two-dimensional function usually assumed to be separable in LSF in the along-scan (LSF_s) and along-track (LSF_t) directions so that: $PSF = LSF_t \times LSF_s$. Similarly, the PSF is also separable as $PSF = LSF_{row} \times LSF_{col}$, where LSF_{row} and LSF_{col} are respectively along the rows and the columns of the gridded product. In this study, the LSF was estimated using the three-step approach proposed by Wenny *et al.* (2015). To estimate the LSF, field border with high contrast were used. As the PSF is location-independent, acquisitions over Sacramento (California, USA) in September 2015 were selected (Figure 2.3 (a)). The average field size in Belgium was indeed too small for a proper PSF estimation and data were available for each sensor. In order to accurately measure the LSF, the exact sub-pixel location of the edge is first estimated by fitting modified Fermi functions (Equation (2.4)) to each row profiles.

$$y(x) = d + \frac{b-d}{1+\exp\left(-s(x-e)\right)} + gx \tag{2.4}$$

where d is the mean reflectance value on the dark side of the edge, b represents the mean reflectance value on the bright side, s is the slope of the edge and e corresponds to the actual edge position, g is the linear coefficient of the modified Fermi function. The parameters of the Fermi function were determined by minimizing the nonlinear least square estimates of the model. As parameter e represents the edge sub-pixel location, row profiles can be aligned to obtain the edge spread function. The linear portion of the modified Fermi model was subtracted from the edge spread function (ESF) profiles. The latter were then scaled from zero to one by dividing by the height of the edge. After this preliminary step, the ESF profiles were smoothed using a spline function which subsequently served to provide regular spacing. The spline filter was implemented to provide smoothed ESF profiles with a step size of 0.05 pixels, *i.e.*, 20 data points per pixel. Finally, the ESF profiles were differentiated to obtain the LSF (Figure 2.3 (c)), a one-dimensional approximation of the PSF.

Again, LSF were normalized between zero and one. The empirical resolution is commonly defined as the width within which the PSF drops to half the maximal value, called Full Width Half Maximum (FWHM). To provide confidence in the PSF estimates, the edge signal-to-noise ratio was computed as the ratio of the mean difference in mean digital number between the dark and bright sides of the edge, and the mean of the standard deviation of the dark and bright sides of the image edge. The empirical FWHM have been derived for each sensor by selecting one band for the main pixel footprint sizes.

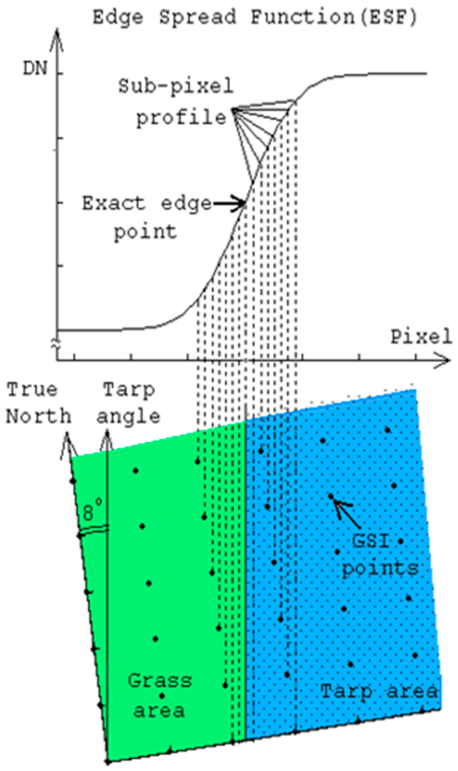

Figure 2.2: Sampling of an edge target by a satellite sensor emphasizing the orientation of the edge with respect to the satellite-sampling grid (bottom). The figure shows how the orientation of the edge leads to a well-sampled edge spread function (top). Figure from Wenny *et al.* (2015).

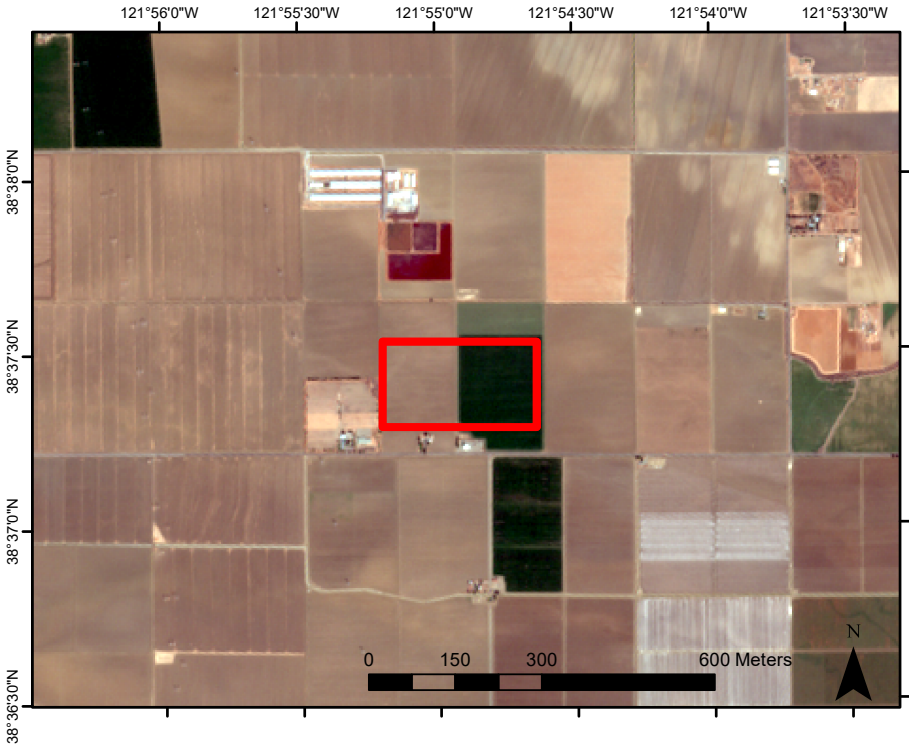

(a)

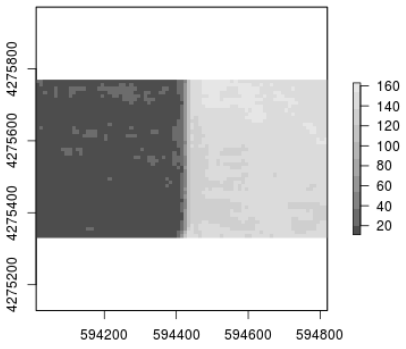

(b)

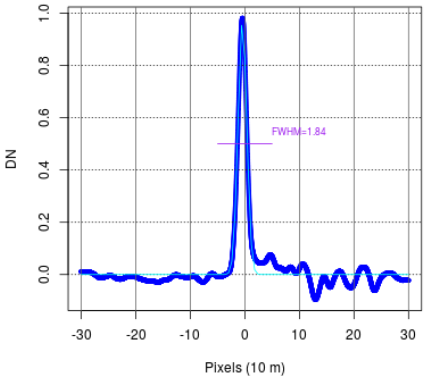

(c)

Figure 2.3: A transition between bare fields and green crop fields was considered as it offers a maximum contrast, homogeneity, sharp transition and proper orientation with respect to the satellite orbit. The red rectangle in (a), a true color Sentinel-2 composite acquired in Sacramento in September 2015, was clipped for the Red, Red-edge and $SWIR_1$ bands. The (b) shows the field transition in the Red band and (c) shows the derived line spread function estimates (blue) with the Gaussian model fit (cyan line), and the FWHM (purple).

Minimum object size. The spectral and the spatial resolution were combined to assess the minimum object size detectable by Sentinel-2 and the other sensors. A spatial object can be detected from a homogeneous background if it remains spectrally separable despite the blurring effect of the PSF. The combination of the spectral and the spatial resolution therefore allows assessing the sensor's potential to detect small spatial objects on the image. Three object shapes have been studied (Figure 2.4): (a) continuous linear objects crossing the pixel in its center or (b) its border, and (c) compact object. These three simplified shapes represent the extreme cases of the most common shapes observable for rivers and ponds.

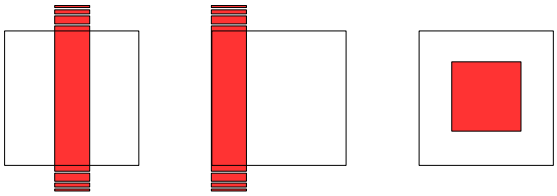

Figure 2.4: Shapes of interest: (a) continuous linear objects (such as river) crossing the pixel in its center; (b) continuous linear objects centered with relation to the pixel border; (c) compact object centered in the pixel such as pond.

The PSF was modeled as a bi-dimensional Gaussian function with a mean of zero and a standard deviation of FHWM/2.355 (Fedorov *et al.*, 2006) assuming that PSF is homogeneous in the along-track and across-track directions. Pixels farther from the center that the 95% confidence interval were assumed not to contribute to the PSF, *i.e.*, their relative contribution is considered as null. To identify the actual minimum detectable area for the three shapes, the width of the foreground object was incrementally increased until the integral of the bi-convolution of the PSF on the object reached the minimum foreground mixture proportion. In other words, the iteration stops when the contribution of the foreground to the measured pixel reflectance is large enough to detect the presence of this foreground object with less than 5% of errors.

2.3 Results

2.3.1 On the spectral resolution

The discrimination power of each pair of classes for most relevant bands and indices for water are presented in Figure 2.5: (a) corresponds to bands and indices common to the three sensors, while (b) shows bands and indices specific for Sentinel-2 and (c) presents indices and bands only available for Sentinel-2 and Landsat-8. As expected, water was well detected using spectral bands in the NIR, the SWIR and the Red-edge bands: a mixture of water and grassland is classified preferentially as water if approximately 20 % of its signal comes from water (limit proportion of background is 0.8). The best band or index for water

detection however depends on the type of background considered. On average, the most reliable band for detecting water in our study area is the Red-edge$_2$ followed by NIR and Red-edge$_1$. On the other hand, ratio indices commonly used for water detection only become accurate when the sub-pixel proportion of water increases around 75 %. NDWI$_1$, NDWI$_2$ and NHI show similar weaker results, which could be partly due to the fact that some of those indices were designed for semi-arid regions where discrimination against various bare soils is the primary issue. For the purpose of small ponds detection in grasslands, where they play a major ecological role especially in temperate ecosystems, vegetation indices such as the Perpendicular Vegetation Index (PVI) appear more sensitive.

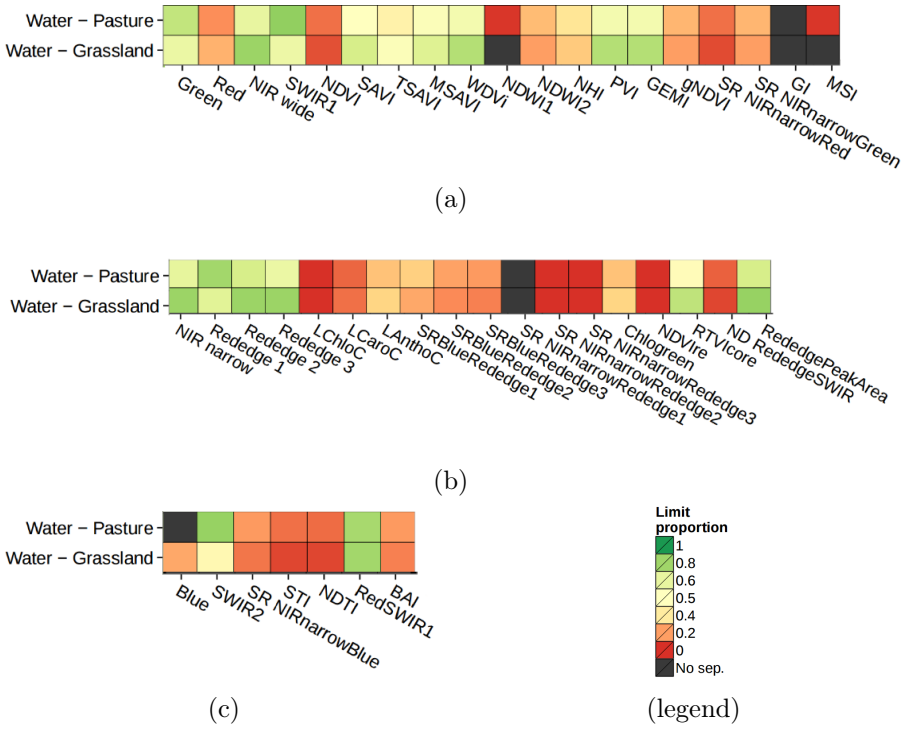

Figure 2.5: Discriminating power of spectral bands and indices to distinguish foreground water class according to the limit proportion of background (pasture or grassland): (a) shows all the bands and indices which are common to the Sentinel-2, Landsat-8 and SPOT-5, (b) corresponds to bands and indices that are specific to Sentinel-2, and (c) shows bands and indices that are not present in SPOT-5.

2.3.2 On the spatial resolution

The empirical spatial resolution, *i.e.* the FWHM, corresponds to the width within which the PSF drops to half the maximum value. The five spectral bands for which the FHWM were empirically estimated are summarized in Table 2.2.

The FHWM estimations range from 20.11 m for the Red band of SPOT-5 to 51.05 m for the Red band of Landsat-8. Considering channels with the same spatial resolution of 10 m, SPOT-5 Red band (20.11 m) is slightly finer than Sentinel-2 Red band (22.06 m) but not significantly different. Relatively to the pixel footprints, the Red-edge$_1$ band of Sentinel-2 and the Red band of Landsat-8 outperform the other tested bands.

Table 2.2: Channels properties and the corresponding full width half maximum values (FWHM) and signal-to-noise ratio (SNR). The standard deviation (SD) provides information on the precision of the estimated FHWM.

Satellite	**Band**	**Channel**	**Resolution [m]**	**FHWM [m]**	**SD [m]**	**SNR**
Landsat-8	Band 3	Red	30	51.05	5.48	21
SPOT-5	Band 2	Red	10	20.11	1.99	57
Sentinel-2	Band 4	Red	10	22.06	1.7	88
Sentinel-2	Band 5	Red-edge$_1$	20	33.48	3.44	50
Sentinel-2	Band 11	SWIR$_1$	20	39.10	2.21	31

In addition to the standard deviation (SD), the signal-to-noise ratio (SNR) was calculated for each of the edge spread functions that were generated (Helder *et al.*, 2006). Guidelines suggest that SNR $\geq$ 100 is optimal for accurate PSF estimation but that consistent estimates can be obtained from an SNR of 50 or greater (Wenny *et al.*, 2015). Values for Landsat-8 and Sentinel-2's SWIR should thus be handled with care.

2.3.3 On the potential for object detection

The minimum width that is required to accurately detect specific foreground objects from their background using the best index or individual band for each sensor is shown in Table 2.3.

Table 2.3: Minimum water bodies' width (m) of continuous linear objects crossing the pixel in its center or its border and square object centered in the pixel detectable by each sensor and the corresponding limit proportion (Prop). The values obtained for the pairs *water-pasture* and *water-grassland* were averaged as they were very similar.

Satellite	Prop (%)	Linear Center (m)	Linear Border (m)	Centered Object (m)
Landsat-8 (30 m)	0.77	12.75	16.25	28
Sentinel-2 (10 m)	0.76	6	6.75	12.5
SPOT-5 (10 m)	0.68	7.25	8.75	13.5
Sentinel-2 Red-Edge (20 m)	0.8	7.25	9.25	16.75
Sentinel-2 SWIR (20 m)	0.81	8.25	10	19.5

Water ponds, considered as centered objects, surrounded by a grassy background are difficult to separate from their background using the 10-m Sentinel-2 bands. Taking into account the PSF and despite a high separability result (limit proportion of 0.76), Sentinel-2 can only detect water bodies larger than 12.5 m, thus larger than its 10-m pixels. SPOT-5 needs even wider water bodies

to be detectable (13.5 m). Sentinel-2 20-m bands (Red-edge and SWIR) and Landsat-8 could detect water bodies just below their spatial resolution with a minimum size of respectively 16.75 m, 19.5 m and 28 m. When looking at the center or border linear crossing objects which have similar results, Sentinel-2 reveals a good potential to detect narrow continuous linear water courses (from 6 m using the 10-m band to 7.25 m using the 20-m Red-edge band). Such results show the ability of Sentinel-2 to detect river and stream at a scale finer than the 10 m and are promising.

2.4 Application of Sentinel-2 potential to detect small water bodies

In this section we first illustrate the results of the paper by comparing a Sentinel-2 classification to a high-resolution reference obtained in chapter 1. The relation between the Sentinel-2 water body classification success and the sub-pixel fraction of water is then evaluated. Secondly, the PSF effect over different sizes and shapes of water bodies is illustrated to draw conclusions of the effective potential of Sentinel-2 for small water body detection. Finally, the isolated sub-pixel surface is compared to a water body classification showing the difficulty to detect the sub-pixel water bodies.

2.4.1 Method

A supervised classification using a Gaussian maximum likelihood algorithm was trained and applied over a Sentinel-2 image covering the South of Belgium acquired on the 15 of March 2016. This classification contains 10 classes: broad-leaved forest, needle-leaved forest, shrubland, grassland, pasture, urban areas, water, roads, bare soil and crop. Blue, Green, Red, NIR_{narrow} and $SWIR_2$ were selected as input data and were all resampled to the coarser resolution band (20 m). This classification was then compared to the 1-m water body map obtained with aerial multispectral photos and LiDAR in chapter 1. This 1-m reference is first convoluted with the Sentinel-2 20-m PSF (from Table 2.2) and then sub-sampled with a nearest-neighborhood algorithm to obtain the reference map at 20-m resolution including the PSF.

2.4.2 Results

Impact of the PSF on the water body classification success rate

Figure 2.6 provides the success rate of the classification according to the percentage of water into the pixel with or without taking into account the PSF. First, the blue curve is what Sentinel-2 is able to detect. It shows that when the sub-pixel contains 25% of water, the success of classification is less than 10% to detect water. When half of the pixel is seen covered with water by the sensor, the water classification success is equal to 50%. The red curve shows what is the effective proportion of water in the pixel, *i.e.* the value that would be seen if we could remove the PSF. In this hypothetical case, the classification

success will be greater for pixel with less than 1/3 water while should be weaker when the pixel contains more than 1/3 of water. The PSF thus improves the detection of water when considering all the water pixels of the scene. This is explained by the spatial structure of water bodies. Most of the water bodies are wider than the pixel resolution and thus their neighborhood pixel's PSF artificially increase the amount of water seen by the sensor, thus improving the classification success when the pixel has more than 1/3 of water.

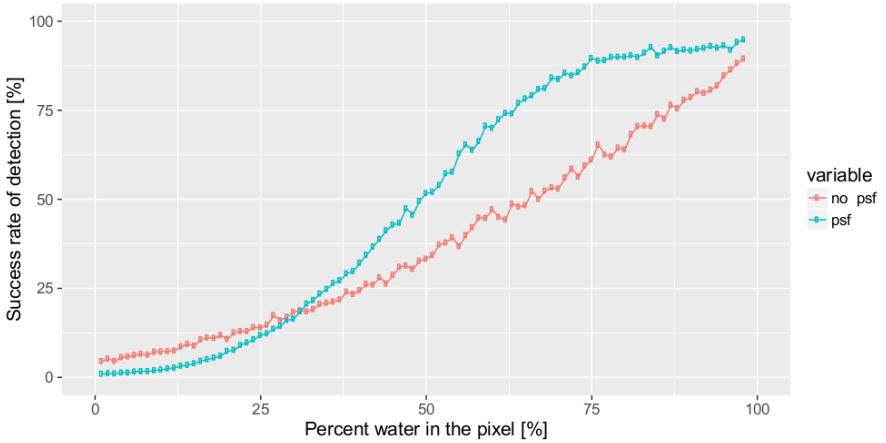

Figure 2.6: Success rate of Sentinel-2 image classification for water classification according to the water sub-pixel percentage with or without taking into account the PSF. The blue curve corresponds to the 1-m water reference map convoluted with the Sentinel-2 PSF and then resampled to Sentinel-2. The red curve consists in the hypothetical case if the PSF could be removed.

Figure 2.7 is an illustration of the PSF effect for three different water bodies shapes: (a) a river, (b) a middle size water body with an island and (c) an isolated sub-pixel small pond. It illustrates the impact of the PSF on the very small ponds and shows the difficulty to detect isolated sub-pixel water bodies. Indeed, the last line of Figure 2.7 corresponds to the percentage of water supposed to be seen by Sentinel-2 including the PSF estimated previously. At this resolution, we see that the river is well detectable but islands on middle size water body as well as isolated pond are not detectable. This is confirmed by the 20-m false color combination of SWIR, Red, and Green presented on the third line.

Impact of the PSF on the isolated water bodies classification

Further results focusing on isolated sub-pixels confirm the difficulty to detect sub-pixel water bodies. As an illustration, we identify 2246 sub-pixel water bodies on the overlapping areas of the 20-m Sentinel-2 image classification and the Walloon region 1-m water body reference. Those ponds are isolated, meaning that there is no water on their eight neighboring pixels, so that the

PSF from close ponds could not affect the value of the considered pixel. We found only 1.7 % of the isolated ponds detected with Sentinel-2. Those results are fully consistent with the Table 2.3 showing that the minimum isolated water bodies detectable using the Sentinel-2 SWIR is 19.5 m meaning that Sentinel-2 cannot detect isolated sub-pixel water ponds.

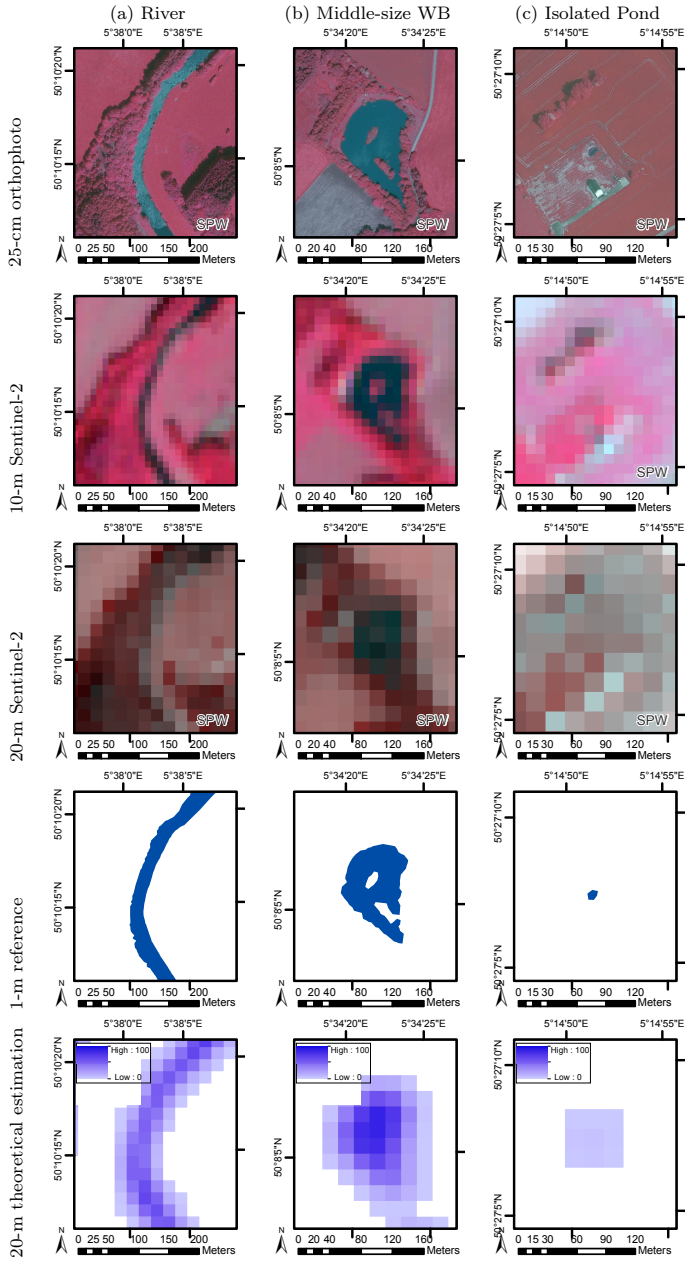

Figure 2.7: Three shapes of water bodies: (a) a river, (b) a middle size water body and (c) an isolated sub-pixel small pond. Six different data are shown by line: (1) a 25-cm orthophoto in false color bands combination (R: NIR, G: Red, B: Green), (2) a 10-m Sentinel-2 (R: NIR, G: Red, B: Green), (3) a 20-m Sentinel-2 (R: SWIR, G: Red, B: Green), (4) a 1-m resolution reference water body map obtained in chapter 1, and (5) the percentage of water being supposed to be sensed by Sentinel-2 at 20-m including its PSF retrieved through the framework presented in this chapter.

2.5 Discussion

This research assessed the potential ability of Sentinel-2's resolution for small landscape feature detection and compared its performances with similar sensors in terms of spectral and spatial resolutions, respectively Landsat-8 and SPOT-5. This methodological framework could be applied on other landscape features or other sensors to characterize the potential of passive optical remote sensing data in a wide range of applications. The spatial and spectral resolutions were assessed separately at first and were then combined to evaluate the theoretical performance of the sensors. The spectral bands shared by the three sensors provided similar discrimination power. However, the analysis showed that Sentinel-2 outperformed the other sensors for most of its indices. By combining high spatial and spectral resolutions, the overall performance of Sentinel-2 for small landscape feature detection placed it above SPOT-5 and Landsat-8. The effect of pan-sharpening on the three images should however be further investigated and is likely to bring SPOT-5 on top for more pairs.

Based on this preliminary study, the two SWIR bands show excellent relative and absolute performances. The major spectral difference between Sentinel-2 and Landsat-8 is the presence of Red-edge bands. Those bands, located at the transition between Red and standard NIR, were added for their potential to discriminate vegetation status and types. In this study, those bands did not markedly improve the separability between classes despite testing a large array of band combinations. These results correspond however to the first radiometric resolution set for the pre-operational Sentinel-2 images, which was further enhanced later on but unavailable on the tested image. The results of the PSF estimation were reproduced with operational Sentinel-2 images with enhanced radiometric corrections (Gascon *et al.*, 2016) and the results were equivalent.

For the water body detection, Du *et al.* (2016) used $NDWI_2$ and MNDWI which is equivalent to the NHI in terms of information as it is the mathematical opposite. In this study, results show that MNDWI performs equally to $NDWI_2$ for water bodies mapping although Du *et al.* (2016) indicates a better discrimination of water using MNDWI. Additionally, several single band indices such as Green, NIR_{wide}, SWIR, NIR_{narrow} and the three Red-edge bands perform equally with less than 5 % classification error probability. However, $NDWI_1$ does not achieve the same success rate for water detection as it has an error probability ranging from 0.15 for water in grassland to 0.05 for water in pasture. Those differences could be explained by the consideration of water only with grassy background while small water bodies could be found predominantly with other background according the region of the study.

Another interesting result is that the 10-m bands of Sentinel-2 could not detect isolated sub-pixel water while 20-m band could. The minimum size of water detectable is difficult to compare with literature as other studies use other sensors and usually only provide the minimum water area detectable and not the minimum size and shape. Minimum detection area referred in the literature is 0.4 ha (Ozesmi and Bauer, 2002; Pitt *et al.*, 2012), 0.5 ha (Jones *et al.*, 2009) and 0.9 ha (Ozesmi and Bauer, 2002). The bands assessed here

have three spatial resolutions (10, 20, 30 m) corresponding to three pixel areas (100, 400, 900 m^2 or 0.01, 0.04, 0.09 ha). Results indicating the limitation of the 10-m bands (0.01 ha pixel) for water and good performance of 20-m band (0.04 ha pixel) are thus in a range of 10 times smaller than what is mentioned in the literature. However, this comparison is limited as this obviously linked to the spatial resolution. A sharpening using the 20-m SWIR band and the 20-m Red-edge to obtain a 10-m resolution could probably improve the results and should be further investigate. Additionally to ponds, Sentinel-2 should also detect narrow continuous linear water courses of 6-m width which seems particularly promising to monitor rivers world wide.

Chapter 3

Monitoring African water bodies from twice-daily MODIS observation

Abstract. The usefulness of static and dynamic water body maps must no longer be demonstrated. Building upon the availability of high revisit frequency Earth Observation satellites at medium spatial resolution (250 m), this chapter investigates the feasibility of mapping and monitoring water bodies at continental scale with MODIS. A 2004-2010 time series of twice-daily observation covering the whole African continent was systematically processed using a surface water detection method to derive 10-day indicators describing the location, the intra– and inter-annual variability as well as the temporal characterization of water bodies (*i.e.* seasonal or permanent water and maximum extent). The multispectral surface reflectance transformation in the HSV color space allows a per-pixel identification of surface water. The subsequent time aggregation of the water indicator provides the water occurrence for each decade built from the 7-year observations. The cartographic products were successfully cross-compared with already existing maps and water products. The validation of the water body maximum extent map estimates the commission error at less than 6% and the seasonality information was also found consistent with the Köppen climatic classes.

The proposed approach is largely modified from 2 published proceedings* and is under review for publication in *GIScience & Remote Sensing*. My contribution was on the design, development and application of the temporal analysis and the quality assessments.

* (i) d'Andrimont, R., Pekel, J.-F., Van Bogaert, E., & Defourny, P. 2010. Monitoring water bodies over whole Africa in near real time : detection algorithms and preliminary results. (RAQRS Proceeding). (ii) d'Andrimont, R., Pekel, J.-F., & Defourny, P. 2011. Monitoring African surface water dynamic using medium resolution daily data allows anomalies detection in nearly real time. (MultiTemp Proceeding).

3.1 Introduction

Given the population growth and the uneven distribution of water supply, better knowledge of the spatial distribution and temporal variability of inland surface water resources is critically needed in view of sustainable development policies and management (Vörösmarty *et al.*, 2000). The Global Climate Observing System (GCOS) includes as Essential Climate Variables (ECV) the lake areas and water level (GCOS, 2011). These variables are needed to support the climate studies and the models required by the United Nations Framework Convention on Climate Change (UNFCCC). The "lake areas" ECV needs mapping of lakes and large reservoirs which directly interfere with the local climate through evaporation and albedo (GCOS, 2011). Moreover, flood and drought monitoring having dramatic economic and human impacts (Alsdorf and Lettenmaier, 2003) need to be monitored in more systematic way. Other application domains are also concerned: human and animal health, food security – agriculture, cattle breeding, aquaculture, gardening – and biodiversity protection (UNESCO, 2009; Vörösmarty *et al.*, 2000). Up-to-date and timely information about surface water can be provided by two different but complementary approaches: mapping and monitoring.

First, the state of the art of surface water mapping at continental and global scales is reviewed. Although topographic mapping based on photogrammetry is a major source about inland water location, it is not consistent across countries and quickly out-of-date due to a long production cycle. Water body maps are thus often the result of an off-line exploitation of space mission or dataset whereas monitoring methods are implemented to generate timely information throughout the year. Water maps can be derived from various Earth Observation (EO) data such as optical imagery, SAR interferometry, LiDAR and gravitational variation. Unfortunately, only optical imagery provides the measurements needed to monitor surface water with a sufficient revisit frequency yet (Alsdorf and Lettenmaier, 2003). In the last 15 years, various methods and datasets were proposed to map surface water at global or continental scale. Few global recent data set products are available with a spatial resolution equal or higher than 1 km. Among these, three products were available when this study was conducted.

First, the widely used Global Lakes and Wetlands Database (GLWD) (Lehner and Döll, 2004) is a compilation of many existing databases. However, according to Haas *et al.* (2009), the use of this database as a standard reference is limited due to the quality and the production date of the source data.

Second, the Shuttle Radar Topography Mission Water Body Dataset (SWBD) (Slater *et al.*, 2006) has a high spatial resolution (30 m). However, it describes the situation as observed at a specific acquisition time (February 2000). The acquisition conditions were not ideal for water bodies as they correspond to the dry season in Northern hemisphere semi-arid regions such as the Sahel. This is a season with low level and even drying out of many seasonal water bodies.

Thirdly, the MODIS 250-m land-water mask (MOD44W) (Carroll *et al.*, 2009) available on the Global Land Cover Facility is a one-off mapping product

based on the combination of SRTM and MODIS data. Although the spatial resolution is 250 m, the dataset is not adequate for applications such as seasonal variability analysis.

After this study, several global products with improved resolution were made available such as SAR-WBI (Santoro and Wegmuller, 2014), the datamask from the Global Forest Change (GFC) (Hansen *et al.*, 2013), the ESA CCI global map of open water body (Lamarche *et al.*, 2017), the Global Inland Water (GIW) v1.0 (Feng *et al.*, 2016) and the Global 3 arc-second Water Body Map (G3WBM) (Yamazaki *et al.*, 2015). Other products were announced in the literature but are not available such as the GLObal WAter BOdies database (GLOWABO) (Verpoorter *et al.*, 2014) and the Global Water Pack (Klein *et al.*, 2015). Chapter 3 and Lamarche *et al.* (2017) compare these products in terms of spatial extent, completeness, thematic accuracy, inland water/ocean discrimination and spatial resolution. Although these products provide major improvements in global inland surface water characterization, none of them propose an annual map update nor a dynamic monitoring.

In addition to inland surface water mapping, several studies were published on water body monitoring. Besides ad hoc mapping for the crisis management (Kugler and De Groeve, 2007), it was shown that surface variation of smaller temporary reservoirs in semi-arid regions due to changing seasonal rainfall patterns can be monitored with optical EO data (Gond *et al.*, 2004; Gardelle *et al.*, 2010; Haas *et al.*, 2011). Nevertheless, to the best knowledge of the authors, there is only two continental water body operational monitoring systems. First, the NASA wetland Earth Science Data Record (ESDR) (NASA-JPL, 2014) delivering global 10-day flood map at the resolution of 25 km which is too coarse to measure most of the natural fluctuations. Second, an operational system monitoring small water bodies, first for the Sahelian zone and then scale up to Africa, uses 10-day syntheses of SPOT-VGT data (Bartholomé, 2008). Based on a contextual algorithm (Gond *et al.*, 2004), the product was developed and validated for sub-humid and semi-arid regions where it performs well (Haas, 2010). Due to limitations observed over dense vegetation areas, it cannot be successfully used at continental scale. To expand the monitoring at continental scale, another method was proposed. First developed for locust monitoring (Pekel *et al.*, 2014), then adapted to water (Pekel *et al.*, 2014), a method using a colorimetric transformation was used to monitor water bodies over time and derive indicators (d'Andrimont *et al.*, 2010, 2011b).

Building upon the availability of high revisit frequency EO observations at medium spatial resolution, this chapter aims to map and monitor the seasonal variability of water bodies at continental scale. More specifically, the objective is to assess the performances of the algorithm proposed by Pekel *et al.* (2014) to retrieve the water body extent at continental scale and to develop derived thematic water products. Through the exploitation of a 7-year time series of MODIS daily surface reflectance acquired over the whole African continent, different indicators are proposed, tested and assessed to characterize the inter-

annual and intra-annual variabilities of water bodies but also to discriminate seasonal from permanent water.

3.2 Data and study area

Four MODIS daily surface reflectance products (collection 5, L2G) are used: (i) Aqua Surface Reflectance at 250 m (MYD09GQ), (ii) Terra Surface Reflectance at 250 m (MOD09GQ), (iii) Aqua Surface Reflectance at 500 m (MYD09GA), and (iv) Terra Surface Reflectance at 500 m (MOD09GA). They are downloaded from the Land Processes Distributed Active Archive Center (LP DAAC) to cover the African continent over a 7-year period, from 2004 to 2010. The study area ranges from 30° North to 40° South and from 30° West to 60° East. Three wavelengths are considered: the Red and the Near-InfraRed (NIR) at 250 m and the Short-Wave InfraRed (SWIR) at 500 m.

In addition to the reflectance, the MODIS Aqua 8-day Land Surface Temperature & Emissivity products (MYD11A2 collection 5) at 1-km spatial resolution are also downloaded from the LP DAAC to cover the entire African continent over a 4-year period, from 2005 to 2008. The MODIS Land Surface Temperature (LST) used in this study is derived from two thermal infrared channels, *i.e.* bands 31 (10.78-11.28 μm) and 32 (11.77-12.27 μm) using the split-window algorithm (Wan *et al.*, 2002) which corrects for atmospheric effects and uses an emissivity look-up table based on global land surface emissivity in the thermal infrared (Snyder *et al.*, 1998).

3.3 Methodology

3.3.1 Water detection

Data pre-processing

Three processing steps before the water detection include the surface reflectance compositing, the composite color space transformation, and the LST average diurnal amplitude computation. These methods are chosen for their robustness and computation speed which make them good candidates for operational applications requiring near real-time information delivery (Pekel *et al.*, 2014).

First, the MODIS surface reflectance measured twice-daily thanks to Aqua and Terra platforms is composited over a 10-day interval (1 to 10, 11 to 20 and 21 to the end of each month) using the Mean Compositing algorithm. This method averages the valid cloud free reflectance values from both Aqua and Terra, based on the standard data quality flags (Vancutsem *et al.*, 2007a,b). This compositing method, assuming that the remaining noise in the daily reflectance is mainly random or can be averaged out, was also selected in the framework of GLC2000 (Mayaux *et al.*, 2004; Bartholomé and Belward, 2005), GlobCover (Defourny *et al.*, 2006; Arino *et al.*, 2008; Defourny *et al.*, 2009) and other land cover mapping initiatives (Gond *et al.*, 2004, 2005). The resulting composites are projected from sinusoidal to Lat/long projection (WGS84 datum). The

500-m SWIR channel is resampled to 250 m resolution using nearest-neighbor resampling algorithm.

Secondly, the 10-day SWIR, NIR, and Red reflectance bands are assigned to Red, Green, and Blue (RGB) colors respectively to be transformed into the Hue, Saturation, and Value (HSV) color space using a standardized colorimetric transformation described in Equations 3.1, 3.2 and 3.3 adapted from Smith (1978). Decoupling the chromaticity (H and S) and the brightness (V) is adapted for developing a color image processing methodology requiring color specification for target identification and extraction (Pekel *et al.*, 2014). This step allows applying the water surface detection algorithm in the Hue-Value subspace.

$$\mathrm{V} = \max\,(\mathrm{SWIR,NIR,Red}) \tag{3.1}$$

$$\mathrm{S} = \frac{\mathrm{V}\text{ - }\min\,(\mathrm{SWIR,NIR,Red})}{\mathrm{V}} \tag{3.2}$$

$$\mathrm{H} = \begin{cases} 0 & \text{if V} = \min(\mathrm{SWIR,NIR,Red}) \\ (\frac{60^\circ \times \mathrm{SWIR\ -NIR}}{\mathrm{V}\text{ - }\min(\mathrm{SWIR,NIR,Red})} + 360^\circ) \times \mathrm{mod}360^\circ & \text{if V} = \mathrm{SWIR} \\ \frac{60^\circ \times \mathrm{SWIR\ -Red}}{\mathrm{V}\text{ - }\min(\mathrm{SWIR,NIR,Red})} + 120^\circ & \text{if V} = \mathrm{NIR} \\ \frac{60^\circ \times \mathrm{SWIR\ -Red}}{\mathrm{V}\text{ - }\min(\mathrm{SWIR,NIR,Red})} + 240^\circ & \text{if V} = \mathrm{Red} \end{cases} \tag{3.3}$$

Finally, LST night and day composited products are averaged separately over four years to derive respectively night and day average temperature products. The average diurnal amplitude is obtained from the difference between these two average products at continental scale. It is used as a proxy of the thermal inertia of land surfaces (Price, 1977; Pekel *et al.*, 2014) and is resampled (nearest-neighbor algorithm) from 1000 m to 250 m. This rough estimation of thermal inertia was found to be sufficient for the scope of this study, as we are exclusively interested in the diurnal amplitude of a specific surface type in the desert.

Water detection methodology

The "H-V space" methodology is summarized here below and further described in Pekel *et al.* (2014). A large sampling of objects corresponding to several millions of pixels spread both in time – different seasons and different years between 2004 and 2010 – and space – from the desert to the dense humid forest – are collected by visual interpretation. They are then used to characterize the open water surface signatures (including lakes, dams, rivers, temporary and permanent water bodies, with different depth, sediments and organic load) and the "other land surfaces" (sands, rocks, lava flows, bright and salt soils, steppes, savannas, shrubs, dry forests, humid forests, swamp forests, rainfed and irrigated croplands, cities). The colorimetric properties of these two categories are remarkably separated in the H-V space with limited risk of confusion in most cases (97% of observations). They can therefore be discriminated through a simple threshold.

An additional discrimination criterion is needed for the overlapping region between the two categories as observed in the H-V space (less than 3% of

observations). These ambiguous pixels are exclusively located in dark lava flow areas in the desert. The ambiguity can thus be partly resolved by using a mask, built in three steps. The first step consists in deriving a mask identifying "potential" permanent water surface where pixels are detected as "water" in more than 95% of observations throughout the composite time series. This mask including also pixels corresponding to dark lava flows is therefore defined as "permanent water and lava". The second step relies on the thermal inertia properties as observed by MODIS LST products. Water surfaces indeed display a strong inertial resistance to thermal fluctuation which translates into low temperature variation during the diurnal heating/cooling cycle. Conversely, dark colored lava flows are characterized by very large thermal amplitude during the diurnal cycle (up to 25°C). Therefore, a threshold applied to the average LST amplitude is efficient enough to provide a mask separating permanent water surfaces from "all other categories". The third step combines the first "permanent water and lava" mask with the "all other categories" mask obtained in the second step. It results in a final "dark lava" mask, allowing discarding the "no water" pixels present inside the overlap area in the H-V space.

3.3.2 Temporal analysis

Water body dynamics could be summarized by different indicators according to the temporal scale of interest. After compositing the daily data into decadal (*i.e.* 10-day) synthesis which are then transformed to H-V space, the pixels are classified as land, water or no data if no valid cloud free reflectance is available during the decade(Figure 3.1). The water detection time series are then used to provide indicators corresponding to different aspects of water dynamics depicting their inter-annual variability, their intra-annual variability and their temporal characterization, *i.e.* seasonal or permanent water and water body maximum extent.

Inter-annual variability

In order to characterize the inter-annual variation, the *Annual Occurrence* is defined as the percentage of time when water is detected for a given year (Figure 3.1-1.). The ratio *Annual Occurrence* (Equation 3.4) is the division of the sum of the detected *water states* (ω) by the sum of the *valid observations* (v) over the *decades* (d) for a given *year* (y) and for each pixel.

$$Annual\ Occurrence_y = \frac{\sum_{d=0}^{d=36} \omega_d}{\sum_{d=0}^{d=36} v_d} \tag{3.4}$$

The *water state*, defined as $\omega \in \{0, 1\}$ corresponds respectively to non-water and water. The *valid observation* $v \in \{0, 1\}$ equals 0 when no cloud free observation is available during the decade and 1 when at least one cloud free observation is available during the decade.

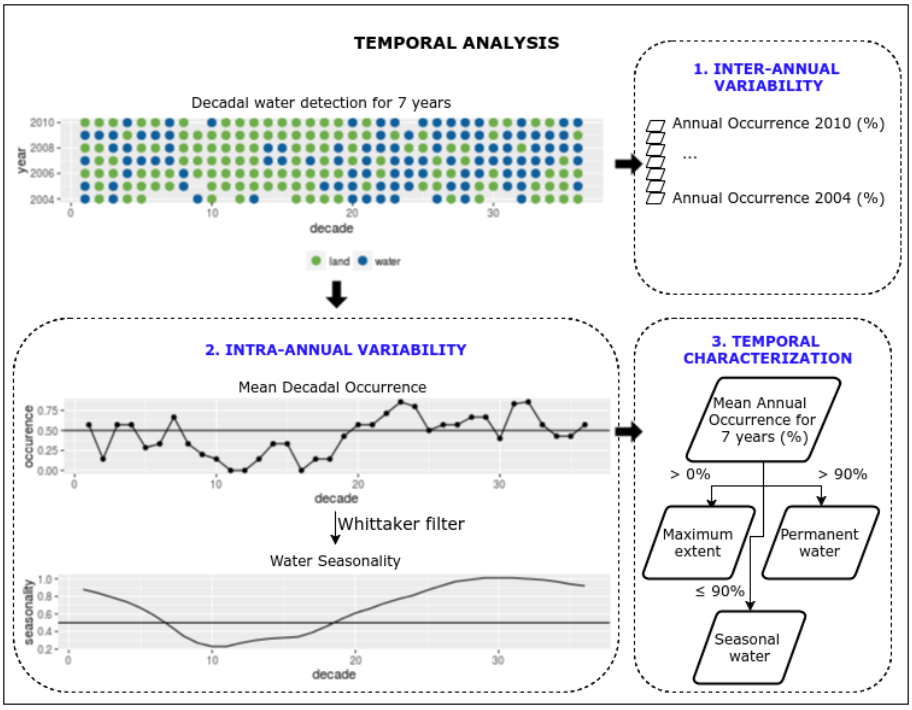

Figure 3.1: For each pixel, a 7-year decadal water detection provides information about 1) inter-annual variability, 2) intra-annual variability and 3) temporal characterization.

Intra-annual variability

Beside the inter-annual variability, a second indicator is the *Water Seasonality* representing the intra-annual variation of water state for each pixel. To obtain the seasonality, the *water state* for each 10-day period from 2004 to 2010 is used to calculate the *Mean Decadal Occurrence* which is then smoothed for each pixel and for each *decade* (d) through a two-step calculation (Figure 3.1-2).

First, the *Mean Decadal Occurrence* for a given pixel and a given *decade* (d) is calculated by dividing the sum of the *water states* (ω) detected by the sum of the *valid observations* (v) across *years* (y) (Equation 3.5).

$$Mean\ Decadal\ Occurrence_d = \frac{\sum_{y=1}^{y=7} \omega_d}{\sum_{y=1}^{y=7} v_d} \tag{3.5}$$

Second, although reflectance data sets are pre-processed to reduce noise from sensor resolution and calibration, digital quantization errors, ground and atmospheric conditions, and orbital and sensor degradation, some noise is still present, including noise that results from cloud cover, poor atmospheric conditions, unfavorable sun-sensor-surface viewing geometries, detection failures and gaps in the time series (Pettorelli *et al.*, 2005; Kobayashi and Dye, 2005;

Geng *et al.*, 2014). Therefore, a temporal smoothing is applied the *Mean Decadal Occurrence* profile obtained with 7 years. Among the temporal profile smoothing available in the literature, the Whittaker filter (Eilers, 2003) is selected for its simple implementation compatible with massive processing. Moreover, the filter is flexible as it does not need any a priori assumption and it has a capacity to interpolate the missing values automatically. Eilers (2003) adapted the algorithm published in 1923 by Whittaker to a smoother able to fit discrete series and put penalty on the roughness of the smoothed curve. Geng *et al.* (2014) compared eight smoothers with MODIS data and conclude that the Whittaker smoother was one of the most suited. As described by Atzberger and Eilers (2011), the aim is to fit a smooth series z to a noisy series y while balancing two conflicting goals: fidelity to the data and roughness of z. A balanced combination of the two goals is the sum Q (Equation 3.6) which needs to be minimized to obtain the z smoothed series. The sum of squared differences S (Equation 3.7) measures the fit to the data. R (Equation 3.8) is the smoothed curve and corresponds to the second order differences. The smoothing parameter (λ) is chosen by the user. Increasing λ value corresponds to increase the influence of R on Q at the cost of degradation of the fit.

$$Q = S + \lambda R \tag{3.6}$$

with

$$S = \sum_i (y_i - z_i)^2 \tag{3.7}$$

$$R = \sum_i ((z_i - z_{i-1}) - (z_{i-1} - z_{i-2}))^2 \tag{3.8}$$

The Whittaker smoothing parameter λ is set to 5 as it has been found the most relevant to handle missing data and obtain good profile from any vegetation NDVI yearly profile (Verhegghen *et al.*, 2014). This has a similar shape and amplitude to water dynamic seasonality profile. The smoothed *Water Seasonality* is obtained by applying the Whittaker filter on the *Mean Decadal Occurrence* profile. The smoothing is operated on the yearly profile extended by half a year before and half a year after in order to take into account the full annual cycle that occur in-between years.

The output, referred as *Water Seasonality*, is a 36-band file where each band corresponds to a different 10-day period depicting the smoothed water occurrence of each pixel. It permits visualization of the temporal water body dynamic as a profile (Figure 3.1-2.). A similar characterization of the dynamic of binary state land cover classes was already proposed for the burned areas and for the snow seasonality (Lamarche *et al.*, 2013; Rousseau *et al.*, 2015)

Temporal characterization

In addition to their inter- and intra-annual variability, classify the water as seasonal or permanent and obtain the maximum extent of water is worthwhile

information. This could be calculated from the 36-decade *Mean Decadal Occurrence* in order to obtain a single-band product summarizing the water state for each pixel for the 7 years. The *Mean Annual Occurrence* is defined as the mean of *Mean Decadal Occurrence* over valid observations (Equation 3.9).

$$Mean\ Annual\ Occurrence\ _{7years} = \frac{\sum_{d=0}^{d=36} Mean\ Decadal\ Occurrence_d}{\sum_{d=0}^{d=36} v_d} \tag{3.9}$$

The result is a map providing occurrence percentage suitable for any end-user threshold. In this study, different maps could be obtained by thresholding the $Mean\ Annual\ Occurrence\ _{7years}$: the *maximum extent water body map* ($> 0\%$), the *seasonal water body map* ($\leq 90\%$) and the *permanent water body map* ($> 90\%$ of the year) (Figure 3.1-3.).

3.3.3 Quality assessment of the temporal analysis

To evaluate the different product's accuracy and their spatial and temporal consistency, three approaches are considered. First, the *maximum extent water body map* is assessed through a random sampling biased towards water areas. Second, an exhaustive comparison between the 10-day products and existing products is carried out. Finally, the *Water Seasonality* is matched to the climatic zone distribution to check possible macroscopic error in the seasonality patterns.

Maximum extent water body map

In order to assess the product commission error (*i.e.* false detection of water), a stratified random sampling is drawn to assess the *maximum extent water body map* over 7 years. As inland water surface corresponds to less than 3% of the African continent, and major lakes and coastlines make up the majority of these detected water surfaces, the sampling is biased to over-sample the temporary water bodies and the rim of permanent water bodies that fluctuate over time. In order to over-sample the changing water bodies, the inner part of major lakes is disregarded. To this end the SWBD is used to create a 1-km inner buffer in the lake center direction for the 10 major African lakes. Moreover, a coastal mask derived from the GlobCover map (Defourny *et al.*, 2006; Arino *et al.*, 2008) is used to avoid selecting samples in the ocean.

A random sampling of 500 points in the water maximum extent excepting inner major lakes and ocean is then drawn (Figure 3.2). The MODIS pixel footprint corresponding to each sample is then displayed on Google Earth imagery to proceed with the photo-interpretation of high and very high resolution images. According to the photo-interpretation practices building on convergence of evidence (Estes and Simonett, 1975; Teng *et al.*, 1997), it is possible to identify water presence at the time of imaging, but also surfaces that can be seasonally flooded. Consequently, the "ground truth" database is not anymore restricted to a single date snapshot. Each sample is labeled as "water", "non-water" or "undetermined". A sample is considered as water when more than the half of the pixel surface is covered by water or a by a floodable surface. The

pixel is undetermined if the visual interpretation is not reliable. This sampling strategy is designed to estimate the commission error of the algorithm but not the omission error as the no water class is not sampled.

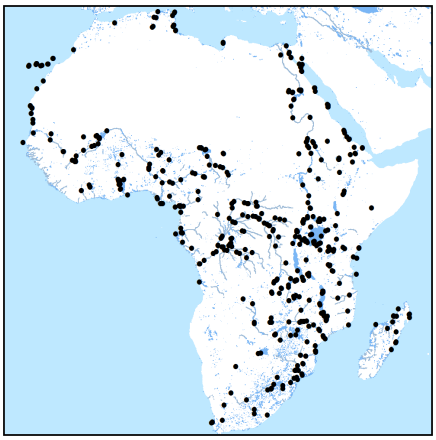

Figure 3.2: Distribution of 500 points randomly drawn in the potential water extent over Africa to assess the *maximum extent water body map* commission error.

Product comparisons

The product quality is also assessed by comparison with two other available water products. First, the *permanent water body map* is compared to the MOD44W product (Carroll *et al.*, 2009). Second, the decadal detection output is compared with the Small Water Body product (SWB) which is valid over the Sahelian zone. The implementation of this SWB algorithm has allowed monitoring the small water bodies and the seasonality of temporary humid areas in an operational manner from January 1999 until 2014 using SPOT-VGT[†]. It should be noted that the SWB product confirms detection of a given decade only when the detection also took place for the same pixel during the previous decade. For the assessment, four decades are selected with a 3-month interval to capture the temporal variability over a year. The year 2010 is selected as it is considered as a normal year in West Africa.

To compare the products, discrepancy matrices are compiled along with the calculation of the Overall Quantity Disagreement (OQD) (Equations 3.10 and 3.11) and the Overall Allocation Disagreement (OAD) (Equations 3.12 and 3.13) as defined by Pontius *et al.* (2011). In our notation, p_{ij} is the estimated proportion of the study area that is in class i in the assessed map and in class j in the reference map. The number of categories is J for both.

[†] The SWB product used in this study was downloaded from the Copernicus GIO Global land portal (`http://land.copernicus.eu/global/products/wb`) where it is referenced as WB V1.4.

$$QD = \left| (\sum_{i=1}^{J} p_{ij}) - (\sum_{j=1}^{J} p_{ji}) \right| \tag{3.10}$$

$$OQD = \frac{\sum_{j=1}^{J} QD}{2} \tag{3.11}$$

$$AD = 2 \min \left[(\sum_{i=1}^{J} p_{ij}) - p_{jj} \ , (\sum_{j=1}^{J} p_{ji}) - p_{jj} \right] \tag{3.12}$$

$$OAD = \frac{\sum_{j=1}^{J} AD}{2} \tag{3.13}$$

Linking water seasonality to climate classification

The Köppen-Geiger climate classification map (Kottek *et al.*, 2006) is used to compute the distribution of permanent and seasonal water bodies areas per climatic zone. For this analysis, four water body seasonality classes are defined according to their persistence within the year (3 seasonal and 1 permanent): (a) less than 1/3 of the decades, (b) between 1/3 and 2/3 of the decades, (c) between 2/3 and 90% of the decades, and (d) more than 90% of the decades. The relative proportions of the different classes are then compared with the respective climatic zone.

3.4 Results

This very first continental scale experiment of surface water detection provides temporally and spatially consistent results. This demonstrates the potentiality of water body mapping at a decadal frequency, which could open interesting avenues for the near real-time monitoring.

3.4.1 Valid data availability for water body detection

A major challenge is the persistent cloudiness over a part of Central and West Africa. The Figure 3.3 represents the average number of valid cloud free observations along the year. In spite of the 2 MODIS observations a day provided by both Aqua and Terra satellites, the annual average number of cloud-free observations is lower than 20 observations a year along the Atlantic coast and is null for the coastal zone of Nigeria (up to 70 km buffer over land). The continent could be divided in two parts identifying the type of possible applications for each zone: (1) the regions with more than 150 cloud free observations a year are suitable for near real-time monitoring and inter-annual comparison as well as for water body mapping, and (2) the regions with less than 150 observations a year (corresponding to about 1 observation out 5 of the potential observations) are not suited for near real-time monitoring with MODIS. For these cloudy regions, where the water scarcity is usually not a major issue, data aggregation over multi-year time series still provide quite consistent results for permanent water body mapping.

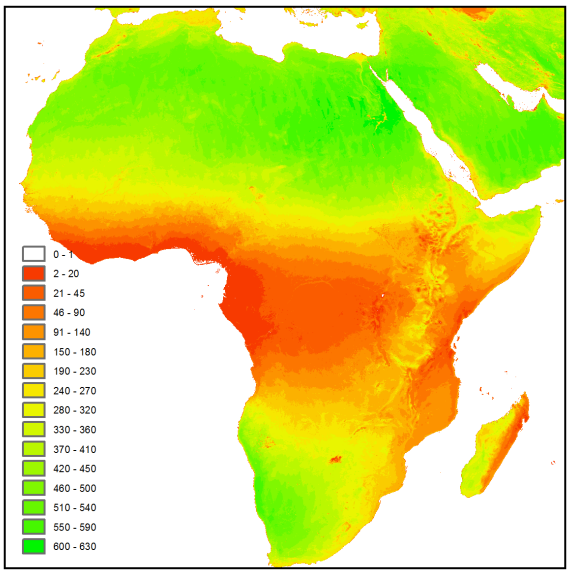

Figure 3.3: Average number of valid observations over a year from both MODIS instruments calculated from 7 years (2004–2010).

3.4.2 Temporal analysis

Inter-annual variability

As a measurement of inter-annual fluctuation, the *Annual Occurrence* for each year from 2004 to 2010 was obtained and is illustrated over Turkana lake and Chew Bahir lake in Figure 3.4. This product monitors the shrinking or expansion of water extent across years. However, the results were less robust than the *Mean Annual Occurrence* as based only on a year and could therefore be limited in areas with important cloud coverage.

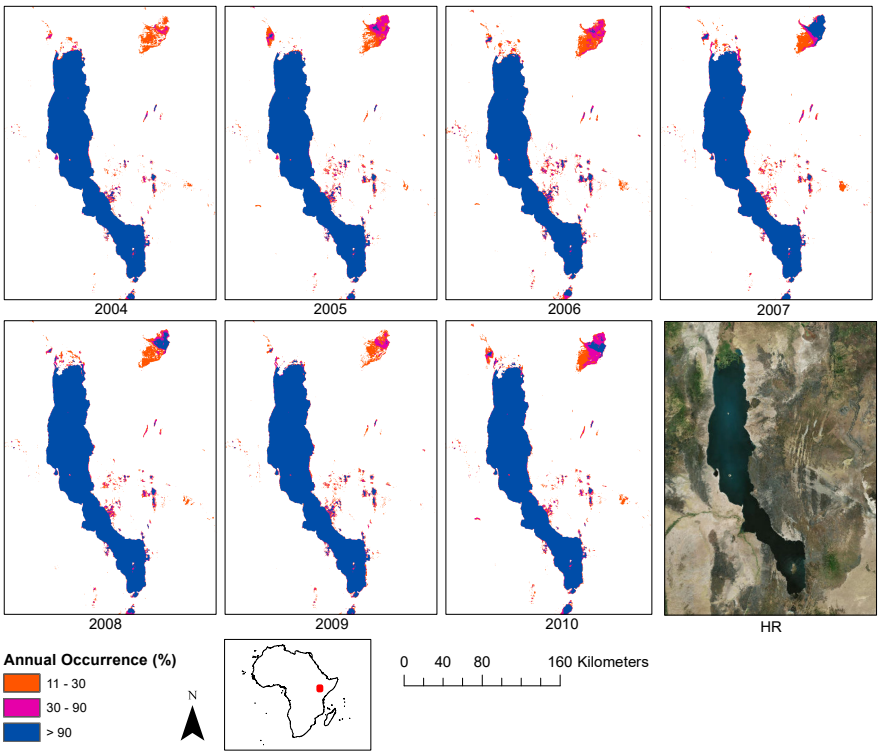

Figure 3.4: *Annual Occurrence* (%) from 2004 to 2010 on Turkana lake (Kenya) and Chew Bahir lake (Ethiopia) grasps the inter-annual fluctuations of water extent.HR is a high resolution satellite imagery.

Intra-annual variability

Based on the decadal detections from 7 years, the *Mean Decadal Occurrence* was obtained and was then used to calculate the *Water Seasonality*. Figure 3.5 illustrates the seasonality over the Niger River in Mali for different types of water: seasonal (point 1 and 3) and permanent (point 2).

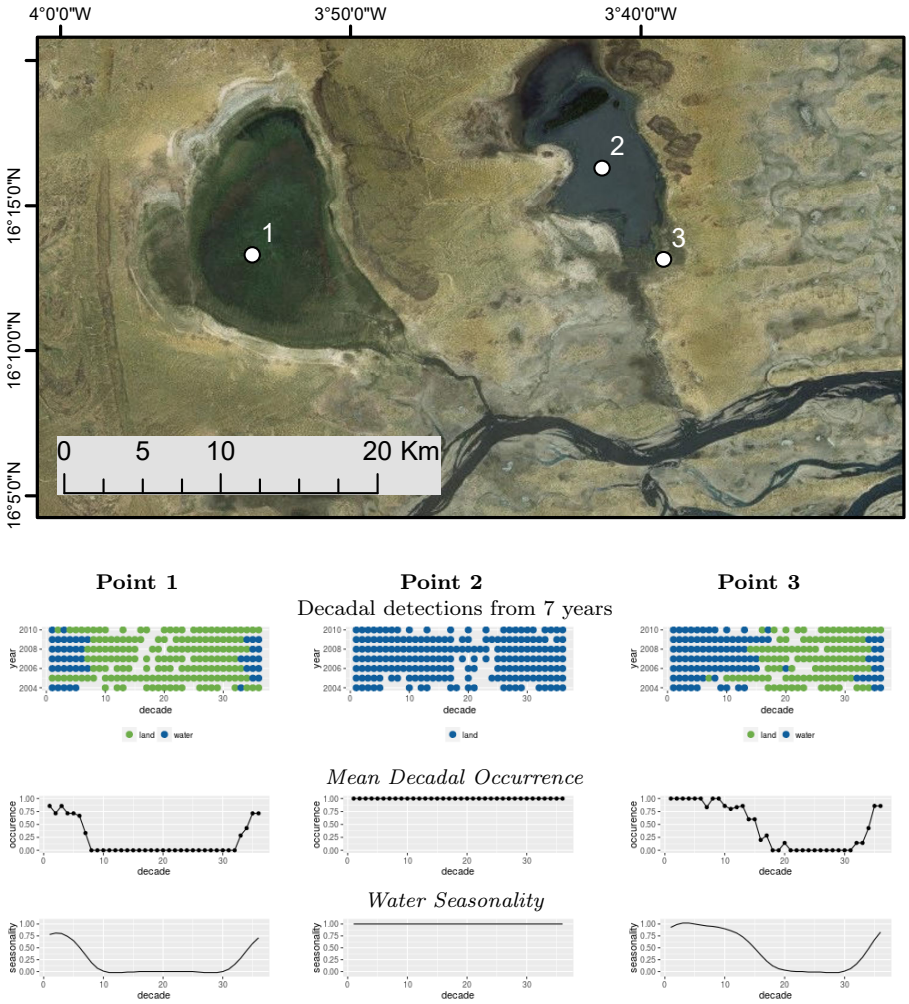

Figure 3.5: Intra-annual water variation is obtained from the decadal detections from 7 years providing the *Mean Decadal Occurrence* which is then smoothed to retrieve the water *Water Seasonality*. Three pixel temporal profiles of the Niger River in Mali shows the potential of the approach to obtain seasonality profile for seasonal (point 1 and 3) and permanent (point 2) surface water.

Temporal characterization

The *Mean Annual Occurrence* map depicts the water according to its mean frequency of observation along the year. The Figure 3.6 (a) shows small water bodies in the Sahelian zone where temporary water bodies were predominant. The Figure 3.6 (b) corresponds to a section of the Volta Lake where dam management for power production and natural conditions induce a significant fluctuation in the water extent. The Figure 3.6 (c) shows the Congo River and

a fraction of the Ntomba Lake well depicted in the equatorial forest. Despite high cloud cover frequency, time series aggregation provide a spatially consistent discrimination between water surface types according to their more or less seasonal nature.

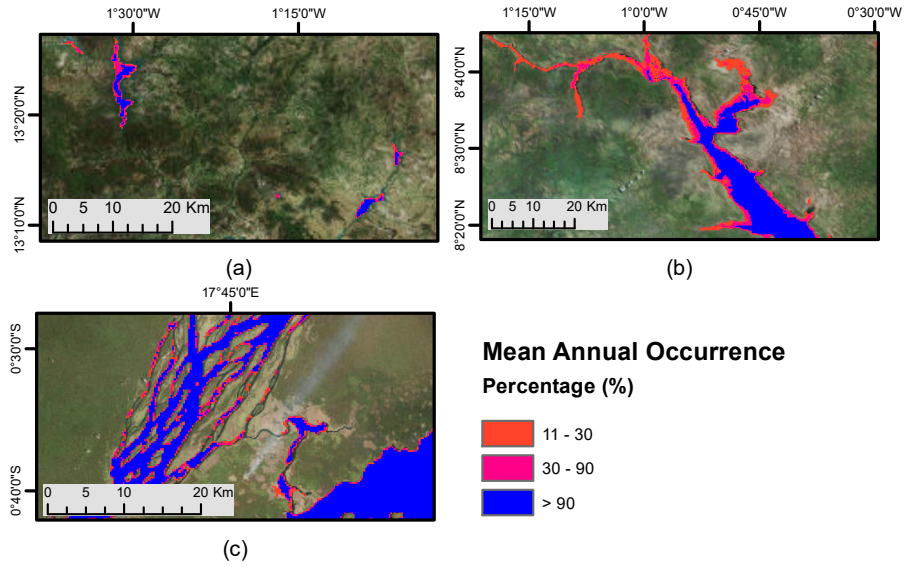

Figure 3.6: *Mean Annual Occurrence* (%) calculated from 7 years is displayed in 3 classes for three different extents: (a) the large water body surface fluctuation in Sahel where the temporary water bodies were predominant, (b) the Volta lake where fluctuations is caused by anthropogenic and natural drivers, and (c) the Congo river well depicted in spite of significant cloud cover.

However, water extent fluctuation of one pixel can also be attributed to the geometric accuracy or be caused by poor observational coverage (referred to as obscov). Indeed, in the case of MODIS, the instrument design and the way the information is stored into a grid can have strong impacts at pixel level (Tan *et al.*, 2006).

Additionally, by thresholding the *Mean Annual Occurrence*, the maximum extent of water along with seasonal and permanent water body maps for the 2004-2010 period have been retrieved providing valuable information for inventory purposes as well as input to model. The *permanent water body map* is shown in Figure 3.7).

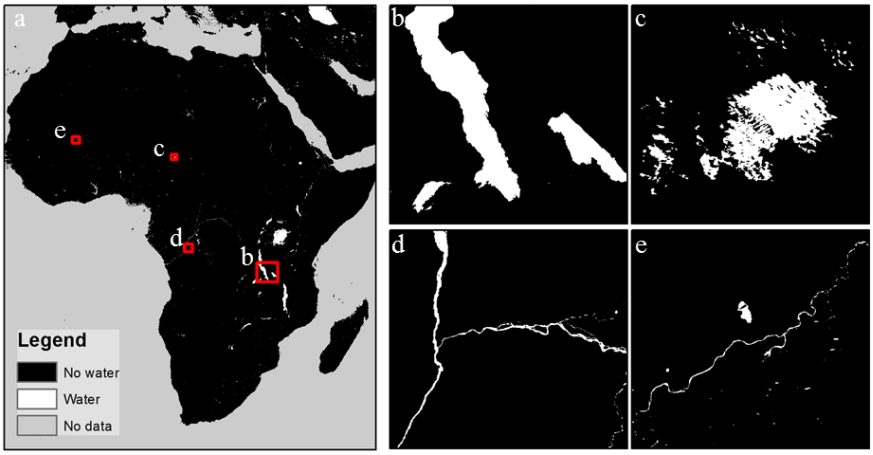

Figure 3.7: Overview of the 250-m *permanent water body map* (a) and subsets revealing the spatial consistency of the map in various contexts : lakes of Tanganyika and Rukwa (b), Chad lake (c), the Congo River (d) and the Niger river (e).

3.4.3 Quality assessment of the temporal analysis

Maximum extent water body map

The commission error of the *maximum extent water body map* was evaluated through a systematic comparison of 500 points randomly distributed according to the sampling design previously described. The commission error is as low as 5.42% (Table 3.1).

Table 3.1: The commission error of the *maximum extent water body map* is evaluated by visual interpretation of 500 random samples using high and very high resolution images. Two samples were undetermined and thus removed from the assessment resulting in 498 points. The commission error is 5.42%.

Reference \ Output map	Water
Non-water	27 (5.42 %)
Water	471 (94.52 %)
Total	498 (100 %)

Products comparisons

The first comparison was completed between the *permanent water body map* and the MOD44W product. The discrepancy matrix presented in Table 3.2 shows a good overall agreement between products (99.78%), and specifically for the detected water (1.1%). The *permanent water body map* depicts more water (1.26%) than the static MOD44W product (1.16%) corresponding to more than 8% in relative difference. This was expected as the observation used for the latter corresponds only to the dry period for the whole West and East Africa while the other is computed from a 7-year time series.

To further analyze these results, the water body extent discrepancies larger than 50 km^2 were systematically assessed on high resolution imagery.

First, among the potential commission errors, *i.e.* detected as water by the *permanent water body map* and non-water by MOD44W, there were 47 polygons greater than 50 km^2 among which only 19 were effectively commission errors (the 28 remaining were thus errors in MOD44W). The remaining 19 commission error areas were distributed in the following landscapes: dark rocks (12), salti lakes (2), volcanic rocks (4) and undefined (1). The distribution among the countries is Chad (9), Ethiopia (4), Libya (2), Eritrea (2), Algeria (1) and Western Sahara (1).

Second, among the potential omission errors, *i.e.* detected as non-water by the *permanent water body map* and water by MOD44W, there were 43 polygons greater than 50 km^2 among which only 14 were effectively omission errors (the 29 remaining were thus errors in MOD44W). The remaining 14 omission errors were lakes (6), desert lakes (3) Chott and salt lakes (2), rivers (2) and Sebkhas (1). The omission error distribution across countries is the following: Egypt (5), Algeria (3), Chad (2), Niger (1), Nigeria (1), Tanzania (1) and Tunisia (1).

Table 3.2: Discrepancy matrix between the water body map and MOD44W (the results are given in percent and do not include ocean and "no data" values).

Water body map \ **MOD44W**	**No water**	**Water**	**Total**
No water	98.68	0.16	98.84
Water	0.06	1.10	1.16
Total	98.74	1.26	99.78

A second comparison highlights the discrepancies between the 10-day water product with SWB, a dynamic water body product available over Western Sahel. In order to compare the 250-m MODIS product with the 1-km SPOT-VGT SWB product, the MODIS products were aggregated to the SPOT-VGT grid using the mode algorithm. This was done for 4 decades distributed at 3-month interval in the year 2010. As the SWB method is designed for semi-arid regions, both products were clipped on the semi-arid region. Afterwards, they were reclassified to obtain 2 classes (non-water and water): humid vegetation class in the SWB was thus reclassified as non-water and no-data from both products were removed.

Finally, the cross-tabulation matrices comparing the 4 selected decades are presented in Table 3.3 and shows that for the 4 decades, the MODIS-based product detects more water than the SWB products due to the finer spatial resolution. On the other hand, the relative seasonal variation computed for the 4 decades are consistently the same for both products. The Table 3.3 provides an information about disagreement between products. The overall quantity disagreements (OQD) are small (0.01–0.26) while the overall allocation disagreements (OAD) are slightly larger (0.56–0.73). Although, the agreements between products are high (98.84–99.68%) and thus the quantity of disagreement is limited, the overall allocation disagreements show that the disagreements come from the pixels location. In conclusion, the comparisons reveal that the amount of water of each class is close but that their pixels are not located at the same place.

Table 3.3: Comparison of water body monitoring by SPOT-VGT SWB and MODIS-based products for 4 decades of 2010 in Western Sahel.

	SPOT-VGT SWB				
	Discrepancies (%)			**Disagreement**	
	Non-water	**Water**	***Sum***	**Allocation** (*OAD*)	**Quantity** (*OQD*)
MODIS 01-10 Jan 2010				0.68	0.02
Non-water	99.19	0.01	*99.20*		
Water	0.69	0.11	*0.80*		
Sum	*99.88*	*0.12*	*99.30*		
MODIS 01-10 Apr 2010				0.71	0.01
Non-water	99.54	0.03	*99.57*		
Water	0.36	0.07	*0.43*		
Sum	*99.90*	*0.10*	*99.61*		
MODIS 01-10 Jul 2010				0.73	0.01
Non-water	99.64	0.04	*99.68*		
Water	0.28	0.04	*0.32*		
Sum	*99.72*	*0.08*	*99.68*		
MODIS 01-10 Oct 2010				0.56	0.26
Non-water	98.64	0.04	*98.68*		
Water	1.12	0.20	*1.32*		
Sum	*99.76*	*0.24*	*98.84*		

Linking water seasonality to climate classification

The seasonality of water bodies corresponds to what is expected for each climate type. This also demonstrates how quantitative water body dynamics could be measured and may be used as a quantitative ecosystem indicator. Table 3.4 reports the distribution of the different water body seasonality classes aggregated by climatic regions of the Köppen-Geiger climate classification (Kottek *et al.*, 2006). The resulting distribution of the seasonality classes closely corresponds to what is expected from a climatic point of view. For the Equatorial zone, the permanent water corresponds to the dominant climate type observed (from 81% for "fully humid" area to 61% for "winter dry" area). For the arid class (represented by "B"), the permanent water proportion is smaller than temporary

water. Moreover, almost half of the observed water surfaces lasts for less than 4 months for the cold arid "BSk" (46%) and the cold arid desert "BWk" (43%) climatic regions. Both BSk and BWk are located in Northern Africa and South Africa. For the warm temperate climate ("C"), the area with a dry summer ("Csa", "Csb") and with a dry winter and a hot summer ("Cwa") are characterized by equal proportions of the different seasonal classes: one third of temporary water bodies lasting less than 4 months, one third of temporary water bodies lasts for more than 4 months and one third of permanent water bodies.

Table 3.4: Water surface distribution percentage according their persistence within the year for each Köppen-Geiger climate class. The Köppen-Geiger climate type are classified according to the main climate (A: equatorial, B: arid, C: warm temperate), the precipitation (W: desert, S: steppe, f: fully humid, s: summer dry, w: winter dry) and the temperature (h: hot arid, k: cold arid, a: hot summer, b: warm summer, c: cool summer). Background grey bars represent the percentage for each seasonality class.

Climate Type Köppen				Duration in the year			
	Main climate	Precipitation	Temperature	< 1/3	1/3 to 2/3	> 2/3	permanent
Af	equatorial	fully humid		6	5	8	81
Am	equatorial	monsoonal		8	11	19	62
As	equatorial	summer dry		7	8	18	67
Aw	equatorial	winter dry		11	6	22	61
BSh	arid	steppe	hot arid	23	17	14	46
BSk	arid	steppe	cold arid	46	18	17	19
BWh	arid	desert	hot arid	25	20	20	35
BWk	arid	desert	cold arid	43	22	21	14
Cfa	warm temperate	fully humid	hot summer	17	10	14	59
Cfb	warm temperate	fully humid	warm summer	12	6	32	50
Csa	warm temperate	summer dry	hot summer	33	14	18	35
Csb	warm temperate	summer dry	warm summer	29	17	18	36
Cwa	warm temperate	winter dry	hot summer	37	16	11	36
Cwb	warm temperate	winter dry	warm summer	10	7	22	61

3.5 Discussion

In this section, the major limitations of the proposed approach along with proposed mitigation measures and potential improvements are discussed.

Optical input data

Despite the recent and coming launches of the optical Sentinel satellites, especially Sentinel-2 and Sentinel-3 both suited for water bodies monitoring, MODIS with its twice-daily revisit will remain a challenger in terms of frequency to imaging the globe. Indeed, nor Sentinel-2, nor Sentinel-3, will provide a better revisit frequency at global scale. Therefore, the limitations about cloud coverage

will remain a limitation factor in the coming years as already highlighted by Whitcraft *et al.* (2015). The high cloud coverage in some areas along with the presence of snow, reduce the available data and limit the 10-day water detection. In areas where data is lacking for most 10-day syntheses, the algorithm is not able to ensure continuous near real-time detection. Frequent cloud coverage is likely to hinder reliable water body monitoring as well as inter-annual anomaly analysis in the equatorial zones, in spite the twice-daily overpasses. For these equatorial zones, the synergistic use of SAR observation with optical should be investigated.

In addition to the revisit frequency, the quality of cloud, shadow and snow screening is crucial for water body detection performance. Indeed, the presence of clouds leads to both omission and commission errors. On the first hand, the water detection algorithm tends to miss water when unscreened clouds are present; on the other hand, unscreened cloud shadows lead to false water detection. False detection also occurs over ice and snow areas especially at the border of the permanent snows.

Another limitation is that the reflectance obtained after atmospheric correction could be negative on water bodies as a result of aerosols load overestimation over very low water-leaving radiance (Li *et al.*, 2009). Therefore a water body mask is used to apply specific atmospheric correction over water. Usually this water mask is not dynamic, major artifacts could thus be observed such as "no data" over large lakes (Pekel *et al.*, 2014) and limit the performance of the detection. Using dynamic water mask for atmospheric correction could limit this caveat in the future.

Finally, a specific limitation of MODIS sensors comes from its whisk-brooms imaging system resulting in a MODIS grid not corresponding to the observation footprint. The particular design of the instrument and the way the information is stored into a grid has strong impacts (Tan *et al.*, 2006). For that reason, MODIS reflectance is provided along with an observational coverage value (obscov), which defines the observation/grid cell intersection area divided by the area of the observation footprint (Wolfe *et al.*, 1998). It was demonstrated that this information could be taken into account in remote sensing applications to limit its effects (Duveiller *et al.*, 2011). For water bodies with a size close to the pixel, the obscov could limit the effective resolution of the resulting product. The obscov information could be integrated in the compositing process to weight the reflectance to mitigate this effect.

Validation

This study provides interesting assessments and comparisons however improvement of the approach along with the definition used could enhance similar study in the future.

First, the accuracy assessment sampling based on 500 points in water permitted to evaluate the commission error for the *maximum extent water body map*. During the photo-interpretation of the sampling, a pixel footprint was labeled as water when at least half of its surface was covered or could be covered by water. This definition used for the assessments penalizes the product for

pixel cover by 50 to 100% of water not detected by MODIS. Using a definition closer to the sensor detection potential such as, a pixel fully cover by water, could limit the overestimation of the commission error.

Secondly, comparison of the *permanent water body map* with MOD44W permits to retrieve discrepancies matrix. Again, the definition of the water class is crucial and could be be a limitation for validation. Here permanent is defined as having a *Mean Annual Occurrence* greater than 90%, while in MOD44W, there is no clear definition for permanent water.

Thirdly, the comparisons of 10-day period maps with existing SWB products provide discrepancy matrices along with disagreement metrics. The comparison reveals a small overall quantity disagreement but a large overall allocation disagreement between products. Clearly, such approach is limited as the sampling through time was limited to 4 dates of one year. A recent publication about validation of a dynamic burned area product from MODIS (Boschetti *et al.*, 2016) proposes a sampling design scheme based on a stratification with equal sample allocation among strata and integrates the time as a variable for the sampling design. The study shows it is effective in reducing the standard errors of accuracy and area estimators. Such approach could be envisaged to assess water body dynamic maps in the future.

Transferability of the detection method

The detection method is well suited for water detection at continental scale and is transferable to other sensors, however some limitations have been highlighted in this study.

The major limitation of the method is the need to adapt the thresholds according to the sensors used. After having tested the MODIS Hue-Value thresholds on SPOT-VGT and PROBA-V sensor, it appears that the thresholds selected in the Hue-Value space do not provide the same results.

In addition, because of the equation used to obtain the Hue, a slight differences in SWIR, NIR and Red may induce major changes in Hue. As Hue's values are different for water bodies when computed from the reflectances of two different sensors, the same thresholds cannot be used for making a consistent detection of water. This limitation implies that new thresholds should be defined to transfer the methodology to another sensor.

Future researches should provide a statistical automated method for best thresholds selection along with the sampling used to set up thresholds.

How to manage false detections?

After having tested the algorithm in various conditions with different sensors, some major false detections still remain but can be localized and removed. Indeed, the algorithm is making false detections over some very low reflectance values such as topographical shadows, dark rocks and lava flows. As already mentioned, other areas wrongly detected are the ice and snow areas in particular at the edge of the permanent snows. To mitigate these false detections, we propose a false-detection mask obtained in five steps which permits to remove the major systematic commission errors made by the algorithm.

The rationale is to mask areas where water is detected by the algorithm but is not present in external reference products and at the same time covered by glaciers, or located on steep slopes, or on high altitudes. This masking is confirmed through high-resolution imagery photo-interpretation. In practical terms, the *maximum extent water body map* is compared to a compilation of external global permanent water references in order to retrieve all the potential commission errors areas. Then the second step masks the permanent glaciers as mapped by the Randolph Glaciers Inventory (Pfeffer *et al.*, 2014) and SCAR data (Fox *et al.*, 2013). The third step masks the commission errors over steep slopes by using the SRTM CGIAR at 90-m (Jarvis *et al.*, 2008) with the definition of Martinis *et al.* (2013): the dynamic water bodies are unrealistic over areas of steep incline ($> 10°$), or significant height and lower slope ($> 2,000$ m and a slope of $> 8°$). Finally the polygons of the mask are visually assessed on high resolution imagery (*i.e.* Google Earth and Bing). After visual analysis, the polygons identified as potentially covered by water are removed from the mask to avoid masking water. This last step is the major limitation as it needs photo-interpretation which is time consuming. Applying such a mask permits to reduce most of the systematic false detections.

3.6 Conclusions

Simple and robust image processing methods were sufficient to retrieve reliable information about the location, the intra- and inter-annual variability of water bodies in Africa from a 7-year MODIS dataset. Moreover the method is sufficiently simple to be easily implemented in an operational processing chain to generate timely or near real-time water status information (where enough data is available) for water management and environmental monitoring purposes. This continental-wide experiment indicates that global scale mapping of water bodies and their seasonal dynamic could be achieved from multi-year time series. The output of this experiment also delivered a map of permanent inland open water surfaces, a map of their average seasonal status and an intra-annual seasonality profile from every location in Africa. The seasonal duration of water bodies as identified from the MODIS data is in agreement with the climatic regions defined by the Köppen-Geiger climatic classification. This underlines the interest of analyzing the behavior of small water bodies along with larger lakes and reservoirs for climate change studies.

The future researches should focus on expanding the approach geographically to global scale and on improving the genericity of the method to make it transferable to other sensors. Nevertheless, all the presented limitations should be addressed. Another promising perspective it to adapt the proposed approach to higher resolution sensors such as Landsat and Sentinel-2. This could leads to better characterization of the water surface dynamics which are currently limited. Finally, this study has contributed to implement the proposed approach first as Geoland-2 prototype and then as a Copernicus Global Land service (Lacaze *et al.*, 2010, 2011, 2012; d'Andrimont *et al.*, 2010, 2011b; Smets *et al.*, 2013; Lacaze *et al.*, 2014a,b).

Chapter 4

Validation of a 150-m permanent inland water global map

Abstract. In the first three chapters, we presented methods to map surface water at different spatial scales. A logical next challenge is to be able to assess the accuracy of the resulting maps. Map's validation is challenging, especially for underrepresented dynamic land cover class such as inland water (∼3%). Currently, there is no consensus among the scientific community and no harmonization leading to difficulties to assess the quality of the binary maps. The development of rigorous validation methodologies for surface water is therefore particularly important. After reviewing the existing global water products along with their accuracy assessments, a global validation to assess permanent water map is proposed and applied on a global, spatially-complete and accurate mask of inland water for the 2000-2012 period obtained by integration of existing products. This map of open water bodies was built in the framework of the European Space Agency (ESA) Climate Change Initiative (CCI) and is referred as the CCI global map. The originality of the validation developed approach is to intentionally skew the sampling towards areas prone to errors in characterizing water bodies. The input used to derive the global map along with the consolidated products were assessed quantitatively against a reference validation database of 2110 samples spread throughout the globe. Using all samples, overall accuracy was always very high among all products, between 98% and 100%. When focusing on the challenging areas for water bodies mapping such as shorelines, lakes and rivers banks, all products yielded substantially lower accuracy figures with overall accuracies ranging between 74% and 89%.
The proposed approach and the results were published in a collaborative paper* where my contribution was on the validation part which is presented in this chapter.

*Lamarche, C., Santoro, M., Bontemps, S., d'Andrimont, R., Radoux, J., Giustarini, L., Brockmann, C., Wevers, J., Defourny, P. & Arino, O. 2017. Compilation and Validation of SAR and Optical Data Products for a Complete and Global Map of Inland/Ocean Water Tailored to the Climate Modeling Community, in *Remote Sensing*, 9(1), p. 36.

4.1 Introduction

Reliable assessment of the world water resources is of paramount importance for decision making, governance and mitigation (Bates *et al.*, 2008). Maps depicting distribution and extent of surface water also support hydrological simulation analyses, climate modeling and satellite data processing (Carroll *et al.*, 2009). Global maps of open water bodies allow retrieving key climate variables such as evaporation, water/land surface temperature, energy balance, selecting appropriate aerosol algorithms and sharing a common coastline map between processes. Nine global water body products at moderate (250 - 1,000 m) or high spatial resolution ($<$ 30 m) are currently available (Table 4.1) and are reviewed below.

Traditionally, cartographic methods with the support of Earth observation data have been used to delineate water bodies. The Global Lakes and Wetlands Database (GLWD) (Lehner and Döll, 2004) compiled large-scale and regional sources for lakes, reservoirs and wetlands greater than 0.1 km^2 dating prior to 2000. The Global Insight Plus database (Europa-Technologies, 2014) contains drainage features represented as lines/polylines at 1:1 M scale with a horizontal accuracy below or equal to 2048 m. The major caveats of such data products are the coarse representation of water bodies, geolocation flaws and the risk of becoming obsolete.

Remote sensing is the primary tool to provide accurate, detailed and up-to-date characterization of inland water bodies on a systematic basis for any location on Earth. A variety of methods and datasets have been developed in the last decade to map open water bodies at global or near-global scale, using active radar and passive optical satellite observation.

The first wall-to-wall map of water bodies for large parts of the globe was derived with Synthetic Aperture Radar (SAR) data acquired during the Shuttle Radar Topography Mission (SRTM). The SRTM Water Body Dataset (SWBD) (Farr *et al.*, 2007) was obtained as a by-product of the main target of the mission, *i.e.*, a digital elevation model of all land masses imaged by the SAR. The SWBD has a spatial resolution of 90 m, is void-free, with river continuity being ensured by a thorough post-processing of the initial classification from the SAR data (Slater *et al.*, 2006). The SWBD map represents the water extent between 11 and 21 February 2000 between 60° N and 54° S. More recently, multi-temporal SAR metrics derived from Envisat ASAR data acquired between 2005 and 2012 were exploited to generate a nearly global dataset of permanent open water bodies. The dataset referred to as SAR-based Water Body Indicator (SAR-WBI) covers land masses between 84° N and 60° S and has a spatial resolution of 150 m, except in areas with predominant coarse resolution ASAR data coverage (1000 m) (Santoro and Wegmuller, 2014). The SAR-WBI was found to accurately characterize the spatial distribution of water bodies, primarily in the northern latitudes. The major caveat of the SAR-WBI is the omission of water along

Table 4.1: Available global or near-global water body products with their references, data sources and water thematic classes.

Products (References)	**Sources**	**Water thematic classes**
GLWD (Lehner and Döll, 2004)	Dataset compilation	Permanent
Global Insight Plus (Europa-Technologies, 2014)	Dataset compilation	Permanent
SWBD (Farr *et al.*, 2007)	SAR (SRTM)	Permanent
SAR-WBI (Santoro and Wegmuller, 2014)	SAR (ASAR)	Permanent
MOD44W (Carroll *et al.*, 2009)	SAR (SRTM) + Optical (MODIS)	Permanent
GIO WB (Lacaze *et al.*, 2015)	Optical (SPOT-VGT, PROBA-V)	Dynamic
GFC-datamask (Hansen *et al.*, 2013)	Optical (Landsat)	Permanent
GIW v1.0 (Feng *et al.*, 2016)	Optical (Landsat)	Permanent
G3WBM (Yamazaki *et al.*, 2015)	Optical (Landsat)	Permanent, Temporary

shorelines and the absence of water features being smaller than twice the pixel size.

The first water bodies dataset based on optical remote sensing data and reported in the literature is the Global Raster Water Mask at 250-m resolution (MOD44W) (Carroll *et al.*, 2009). This dataset builds on the SWBD, by filling gaps with MODIS optical data available for years 2000 and 2001. To achieve a truly global extent, the classification was complemented with water detections from the MODIS data north of 60° N and with a mosaic of Antarctica land masses (Haran *et al.*, 2005) south of 60° S (Carroll *et al.*, 2009). In regions where water was detected using MODIS data, water bodies smaller than 2–3 pixels may have been missed (Carroll *et al.*, 2009). MODIS data at 250- and 500-m resolution were also used in the Global Water Pack methodology to derive the daily temporal dynamics of water (Klein *et al.*, 2015), but no product has been released so far. PROBA-V acquisitions from January 2014 to present at a spatial resolution of 1000 m are used to generate the Copernicus Global Land Service Collection 2 (Copernicus WB) dataset, consisting of water body maps every 10 days between 80° N and 60° S (Lacaze *et al.*, 2015).

High-resolution (30 m) Landsat time series were intensively exploited in the last few years to detect water surfaces and monitor water dynamics. The Global Forest Change (GFC) product depicts forest extent and change from 2000–2012 (Hansen *et al.*, 2013). The sub-dataset "datamask" (hereafter, GFC-datamask) includes the class "permanent water bodies" covering all land masses between 80° N and 57° S. The 30-m Landsat Global Land Survey (GLS) data acquired for the 2000 epoch were used to generate an inland surface water classification between 90° N and 60° S referred to as the Global Inland Water (GIW) v1.0 product (Feng *et al.*, 2016). Using multi-temporal GLS images from 1990–2010, (Yamazaki *et al.*, 2015) produced a map of permanent and seasonal water bodies referred to as the Global 3 Arc-Second Water Body Map (G3WBM). The data product spans 90° N and 60° S and has a spatial resolution of 90 m. Pan-sharpened Landsat 7 (14.25 m spatial resolution) imagery circa 2000 was used to generate the Global Water Bodies database (GLOWABO), including all lakes larger than 0.002 km^2 (Verpoorter *et al.*, 2014). More recently, (Donchyts *et al.*, 2016) presented the Deltares Aqua Monitor and Pekel *et al.* (2016) the Landsat-based 30-year global surface water dynamics with a spatial resolution of 30 m.

Quality assessment and continuous quality monitoring constitute the only means of guaranteeing the compliance of generated products with user requirement. This should follow, as much as possible, the guidelines, protocols and metrics defined by the Land Product Validation (LPV) group of the Committee on Earth Observation Satellite (CEOS) for the validation of satellite-derived land products. Despite the areas of Water Bodies are not included into the focus areas of the LPV group, the validation protocol should rely on similar aspects: the spatial and temporal consistency, and the accuracy of the water detection. Validation of the reviewed water body products, when performed, followed various strategies. Accuracy assessments of the MOD44W (Carroll *et al.*, 2009), the GIW v1.0 (Feng *et al.*, 2016), the GLWD (Lehner and Döll, 2004), the GLOWABO (Verpoorter *et al.*, 2014) and the G3WBM Yamazaki

et al. (2015) rely on the comparison of the total water bodies area estimation between existing products. These methods of comparison are not spatially explicit, as no information is provided about the location of disagreements between products. In addition, results are not validated with reference data. To validate the SAR-WBI, confusion matrices were built over limited areas using independent maps (Santoro and Wegmuller, 2014). Santoro and Wegmuller (2014) reported the Overall Accuracy (OA), Producer Accuracy (PA), User Accuracy (UA) and Kappa indices. The variety of approaches does not allow comparing strengths and weaknesses of available water body products. In addition, reference validation datasets cover limited areas and are only used to validate a given product, without making any performance comparison with other existing ones.

In the context of the ESA CCI, climate and remote sensing communities expressed the need for a global, precise and accurate mask of open permanent water body that could be used across Essential Climate Variables (ECVs) (Mason *et al.*, 2010) for consistent land-water mask, satellite data processing and climate modelling. Therefore, after reviewing the criteria of the users and the available products, four input water body products were selected: the SWBD, the SAR-WBI, the GFC-datamask and the GIW v1.0. They were combined and consolidated by Lamarche *et al.* (2017) resulting in the CCI global map of open water body† (Figure 4.1), the only fully global inland water/ocean distribution at 150-m spatial resolution.

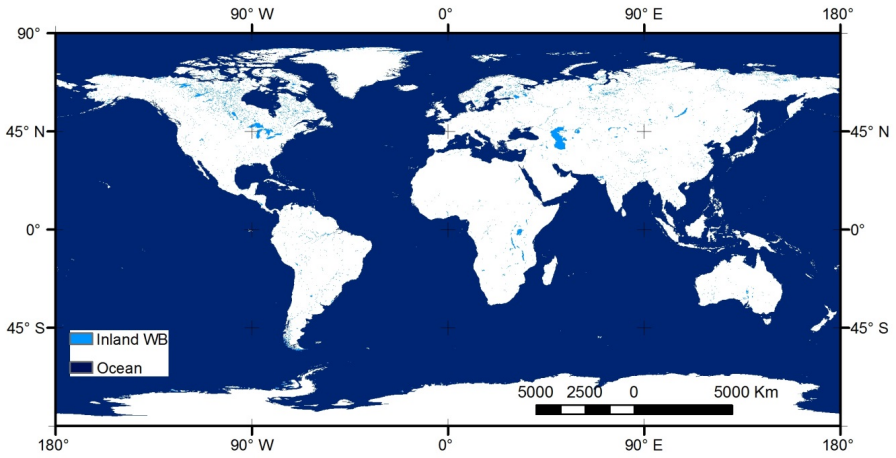

Figure 4.1: The CCI global map of open water bodies (Version 4.0) compiled by Lamarche *et al.* (2017).

The complementarity of the GFC-datamask and the GIW v1.0 products was key to obtain an exhaustive detection and delineation of water bodies.

†The Water Body Map (referred as Version 4.0) is available for download at `http://maps.elie.ucl.ac.be/CCI/viewer/download.php`

Figure 4.2 from Lamarche *et al.* (2017) illustrates the increase of river continuity brought by the GIW v1.0 (a,b), compensations for water body omissions present in the GFC-datamask (c) and "no data" filling by the GFC-datamask (d). The SAR-WBI contributed significantly north of 68° N (Figure 4.2e). In addition, it contributed to updating the classification based on the Landsat data in areas with more recent artificial basins. Figure 4.2f illustrates the Indira Sagar Dam commissioned on May 2005, where neither was included in GIW v1.0, nor in the GFC-datamask.

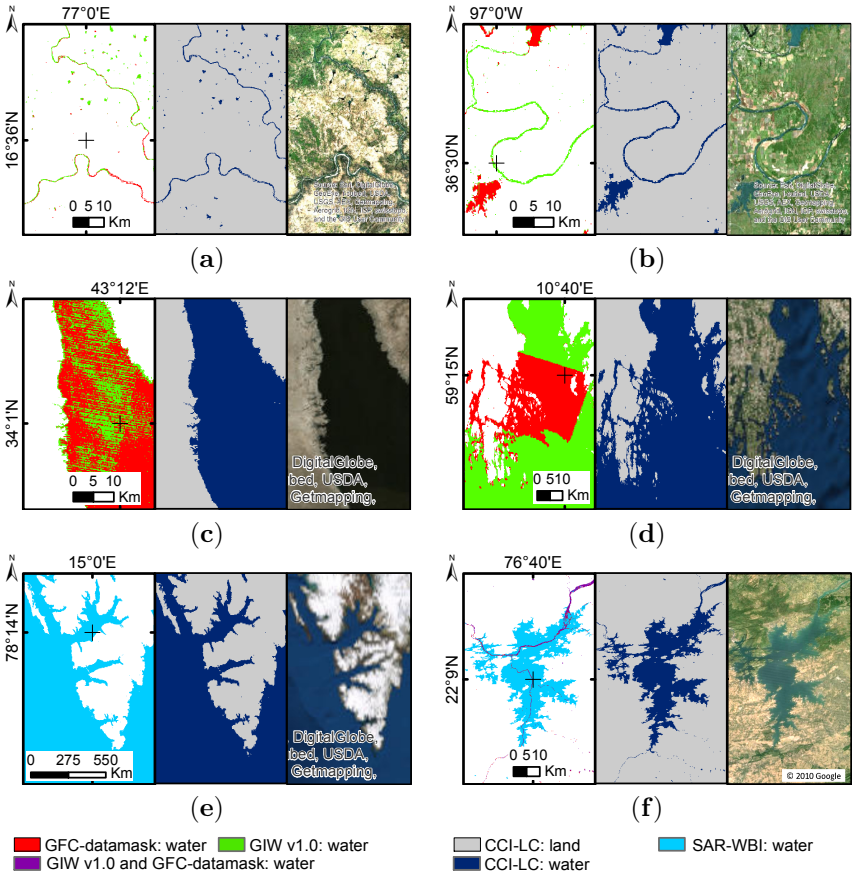

Figure 4.2: Lamarche *et al.* (2017) provide examples illustrating the complementarity of selected input data sources to the CCI global map of open water bodies: (**a**) the lack of continuity in the GIW v1.0 river network was complemented by the GFC-datamask; (**b**) the lack of continuity in the GFC-datamask river network was complemented by the GIW v1.0; (**c**) artifacts from the Scan Line Corrector-off issue in Landsat ETM+ in the GFC-datamask were compensated with inclusion of water from the GIW v1.0. (**d**); GIW v1.0 unprocessed or atmospherically-contaminated areas were filled with the GFC-datamask; (**e**) detections in the SAR-WBI in areas north of 68° N, not included in other water body products; (**f**) map updating with the SAR-WBI for more recent water bodies.

The objective of this study is to propose an original and rigorous stratified random sampling designed for the quality assessment of binary classifications where one class is marginally distributed. This method is applied for the global assessment of the CCI map of open water body and for a detailed comparison of its constitutive source products.

4.2 Methodology

4.2.1 Sampling scheme

Differently than traditional accuracy assessments relying on simple random sampling, a two-level stratified random sampling (Figure 4.3) was used to avoid under-sampling rarely occurring map classes such as "water" (Congalton, 1988).

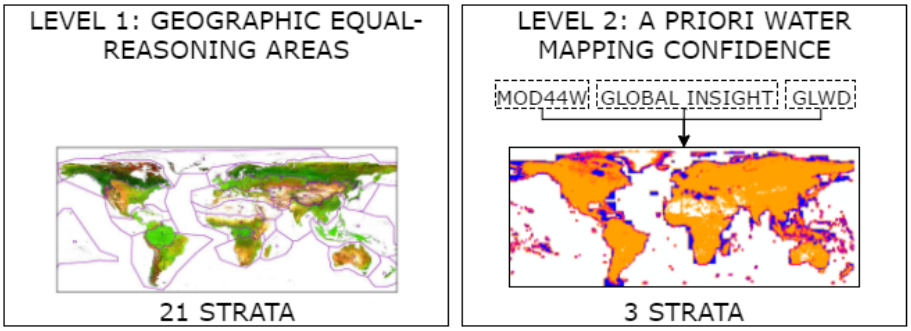

Figure 4.3: Global permanent water maps are assessed by a two-level stratified sampling using both equal-reasoning areas stratification (level 1) along with external water dataset to skew the sampling in error-prone areas (level 2).

The first level of stratification was geographic in order to obtain a homogeneous distribution of validation samples everywhere (Figure 4.3-left). It generated 21 "Level-1" strata (open oceans and polar areas excluded) defined by bioclimatic and remote sensing criteria (Defourny *et al.*, 2012). The number of samples per Level-1 strata was proportional to their area.

Good practices of accuracy assessment suggest that class-based stratification reduces standard errors of class-specific accuracy estimates (Olofsson *et al.*, 2014). However, because inland water corresponds to a marginal class with respect to global land surface, using water and land as strata would be obviously beneficial for the user accuracy, but could result in optimistic producer accuracy results due to the reduced probability to sample water omission. The "level-2" stratum was therefore developed based on the a priori confidence of correctly representing map classes (Figure 4.3-right). This confidence-based stratification was categorized into three Level-2 strata: high confidence in correctly mapping the land class (Stratum 1), high confidence in correctly mapping the water class (Stratum 2) and error-prone areas (Stratum 3). The combination of the MOD44W (Carroll *et al.*, 2009), the GLWD (Lehner and Döll, 2004) and the Global Insight Plus water layer (Europa-Technologies, 2014) was used to obtain

the three strata. Stratum 1 corresponded to land agreement between the three maps, Stratum 2 to water agreement and Stratum 3 to discrepancies between at least two of the three maps. The surface of Stratum 3, *i.e.*, error-prone areas, corresponded to 76% of the total surface of inland water.

The sample size, S, was optimized with regard to the expected accuracy of the CCI global map of open water bodies, and the confidence interval was derived according to the binomial distribution (Stadelman, 1994):

$$S = \frac{p \times (1-p)}{(\frac{E}{Z_\alpha})^2} \tag{4.1}$$

where E is the allowable error in the sample (half of the confidence interval), Z_α is the critical value drawn from the normal distribution for a given level of confidence and p is the targeted accuracy of the product. A confidence interval of 4% with a confidence level of 95% ($Z_\alpha = 1.96$) was chosen.

Our assumption is that the accuracy of water classification is lower where different maps disagree, while water bodies are usually classified with high to very high overall accuracy in areas of agreement. The targeted accuracy was therefore set to be at least 85% in the error-prone area, which corresponds to approximately 1200 samples. An additional 1200 samples were distributed equally to the other two strata, where the targeted accuracy was at least 93%.

4.2.2 Generation of the validation database

The sampling unit was the pixel materialized with a footprint of 150 m × 150 m. These samples were visually interpreted independently from the product using high resolution Google Earth imagery. Careful attention was paid to interpret and record the permanent, as well as the temporary character of snow and water evenly across the globe by extensive use of historical imagery. According to the photo-interpretation practices building on the convergence of evidence (Estes and Simonett, 1975; Teng *et al.*, 1997), it was possible to identify surfaces that can be seasonally flooded. In particular, these surfaces concern dry river beds, flood-prone areas, irrigated agriculture, mangroves/inundated forests, ephemeral streams, salt pans and snow packs. Samples were labeled as water when at least half of the sample was covered with open surface water. Samples showing temporary snow or water were labeled as land, but the temporal aspect was also recorded. For all samples, the date of the high resolution imagery was recorded. In addition, wetlands and swamps were also recorded.

4.2.3 Accuracy assessment

The CCI global map of open water bodies and its constitutive sources, *i.e.*, the SAR-WBI, the GIW v1.0 dataset and the GFC-datamask were validated against the reference samples of the validation database, assuming that these represent the true Earth surface state. The SWBD was not validated given its minor contribution to the CCI global map of open WB (0.69% of the total inland

water surface). Here, accuracy was assessed at three levels. One assessment included all samples and took into account all strata. A second assessment exclusively focused on the error-prone stratum of Level-2. A third assessment focused on the samples recorded as temporary water. Herewith, it was intended to evaluate whether seasonal water bodies affect the water body product.

The most common way to express classification accuracy is the preparation of a so-called error matrix also known as confusion matrix or contingency matrix (Table 4.2). Such matrices show the cross tabulation of the classified land cover and the actual land cover revealed by sample site results. The assessment was thus quantified in terms of confusion matrices built by comparing each class of the map (n_i) to the reference sample classes (n_j).

Table 4.2: Mathematical formulation of the error matrix.

		j=Columns (Reference)			**Row Total**
		1	**2**	**k**	n_{i+}
i=Rows (Classification)	**1**	n_{11}	n_{12}	n_{1k}	n_{1+}
	2	n_{21}	n_{22}	n_{2k}	n_{2+}
	k	n_{k1}	n_{k2}	n_{kk}	n_{k+}
Column Total	n_{+j}	n_{+1}	n_{+2}	n_{+3}	n

Each confusion matrix reported the Overall Accuracy (OA), the User's Accuracy (UA), the Producer's Accuracy (PA) (Strahler *et al.*, 2006) and the F-score. A McNemar test (McNemar, 1947) is applied to evaluate if performances are significantly different between confusion matrices.

OA represents the proportion of all cases correctly classified (Equation (4.2)) with n being the total number of samples and q the total number of classes (water and non-water). Because the sampling probability was different among the three Level-2 strata, global index values were weighted according to the sampling probability.

$$OA = \sum_{s=1}^{3} w_s \sum_{k=1}^{q} \frac{n_{kks}}{n_s} \tag{4.2}$$

In Equation (4.2), w_s is the weight of the stratum, which is inversely proportional to the sampling effort. The weights are computed for each stratum based on Equation (4.3).

$$w_s = \frac{S_s/n_s}{\sum_{s=1}^{3} S_s/n_s} \tag{4.3}$$

where S_s is the area of the stratum and n_s is the number of sample points in the stratum.

UA corresponds to the probability that a randomly-selected pixel from the map is classified as correct in the reference sample. PA corresponds to the probability that a reference sample is correctly classified in the map. Therefore, UA is related to the commission error while PA informs about the omission error.

They are calculated following Equations (4.4) and (4.5) inside each stratum and thereafter weighted using the same method as for the global overall accuracy.

$$UA_i = \frac{n_{ii}}{n_{i+}} \tag{4.4}$$

$$PA_j = \frac{n_{jj}}{n_{+j}} \tag{4.5}$$

The F-score (Equation (4.6)) represents for a class k the harmonic mean of the user and producer accuracies and ranges between 0 and 1.

$$F - score = 2 * \frac{UA_k * PA_k}{UA_k + PA_k} \tag{4.6}$$

In this study, the same set of sites are used in the assessment of the accuracy of the thematic maps to be compared. Consequently, the samples are not independent, the statistical significance of the difference between two proportions may be evaluated using McNemar's test (McNemar, 1947). This is a non-parametric test that is based upon confusion matrices that are 2 by 2 in dimension and permits to test statistical significance of the difference between two proportions (Foody, 2004). The McNemar test was applied to evaluate if the values reported in the confusion matrix for each individual product were significantly different.

4.3 Results

The reference database included 2400 samples spread over land masses with the exclusion of polar areas (Figure 4.4). Of these, 2121 corresponded to valid data in each of the data sets used to generate the CCI water body product. Eleven samples were further discarded either because of cumbersome interpretation of the Google Earth imagery due to cloud coverage, unavailability of images or uncertain interpretation. For the 2110 samples, 1030 samples are included in the error-prone stratum of level-2 and 234 correspond to temporary water bodies like ephemeral streams, beaches, irrigated cultures and salty lakes.

For each of the three products (the SAR-WBI, the GIW v1.0 and the the GFC-datamask), the overall accuracy was always very high, between 98 and 100% (Table 4.3). This was a consequence of the overwhelming proportion of the land class at global scale with regards to the marginal water class. Yet, water surfaces were not identified with high accuracy in any of the input data sets (Table 4.3). The PAs of water were always lower compared to the values obtained for the CCI water body map, with considerable differences among the individual input data sets. The PA of the CCI global map of open water bodies (92%) outperformed the best PA of the input data sets by 13%. On the contrary, the UA of the GFC-datamask was higher (97%) compared to UA of the CCI global map of open water bodies (86%). The CCI global map of open water bodies overestimated water while the GFC-datamask underestimated it. The GFC-datamask water omission errors were found typically along lake

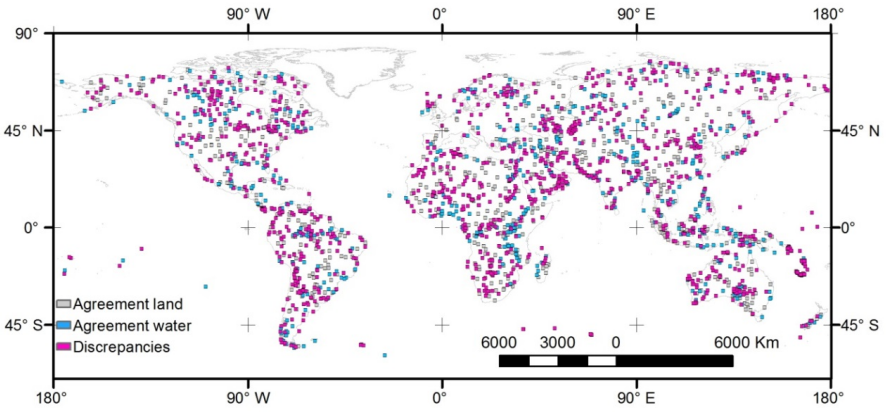

Figure 4.4: Location of the 2110 samples (area of 150 m × 150 m) selected for the validation of the water body products. For each sample, the Level-2 stratum is specified (land agreement, water agreement and discrepancies).

banks, shallow water and dams. The GFC-datamask minimum water extent is probably due to its definition of water using a strict threshold equal or greater to 50% of water detection in the Landsat time series (Potapov *et al.*, 2012). Commission errors are marginal and occur along some lakes and over black lava rocks (e.g. Ethiopia).

Table 4.3: Input water body maps and CCI water body map with their accuracy estimates in percent (%) based on an evaluation of 2110 samples.

	Extent		Non-Water			Water		
	(LAT)	OA (%)	PA (%)	UA (%)	F-Score (%)	PA (%)	UA (%)	F-Score (%)
SAR-WBI*	84°N - 60° S	98	99	99	99	62	84	71
GIW v1.0*	90° N - 60° S	98	99	99	99	78	77	77
GFC-datamask*	80° N - 57° S	99	100	99	100	79	97	87
CCI global map	90° N - 90° S	99	99	100	100	92	86	89

*Sources marked with * have a limited completeness: SAR-WBI:97%, GIW v1.0: 91%, GFC-datamask: 93%, CCI global map of open WB: 100%.*

The F-score of the CCI global map of open water bodies (89%) was significantly higher than the value obtained for the GFC-datamask. The F-score of the SAR-WBI was the lowest of all values (71%) mainly due to an underestimation of water (low PA). Omission errors were located mainly along coastlines, water body boundaries and in mountainous areas (Santoro and Wegmuller, 2014). In areas where the SAR-WBI was based primarily on data with a spatial resolution of 1000 m, water bodies were either missed, imprecisely delineated or only partially detected in fragments. Most commission errors correspond to temporary water (e.g., inundated areas, floodplains, deserts and salars) and to a lesser extent to coastlines, irrigated croplands and mountainous areas (Santoro and Wegmuller, 2014).

The second accuracy analysis focused on error-prone areas (Table 4.4). Compared to the accuracy figures of Table 4.3, the PAs and UAs for this stratum were substantially lower (on average, 14% and 21%, respectively).

Table 4.4: Accuracy results, in percent (%), for the error-prone stratum 3 (1030 samples).

		Non-Water			Water		
	OA	PA	UA	F-Score	PA	UA	F-Score
SAR-WBI	74	90	79	84	23	43	30
GIW v1.0	86	92	90	91	67	72	70
GFC-datamask	89	98	89	93	61	89	73
CCI global map	89	93	92	93	75	78	77

The trend in OA and the PA of the non-water class in the SAR-WBI and the GIW v1.0 datasets did not differ when restricting the analysis to error-prone areas only (see Tables 4.3 and 4.4). On the contrary, the PA and the F-score of the water class of the SAR-WBI were substantially lower. This was due to the frequent omission of water in the SAR-WBI; however, since water represented a small proportion of the classes being mapped, the effect of omission was not visible in the statistics derived for the overall assessment.

Similarly, the GFC-datamask and the CCI global map of open water bodies gave identical trends in the results for OA and F-scores for the class non-water (see Tables 4.3 and 4.4). The GFC-datamask was prone to water omission and the CCI global map of open water bodies to water commission. The underestimation of water in the GFC-datamask (PA of 61%) was exacerbated in error-prone areas that include a high proportion of shorelines, lakes and river banks. The PA of the CCI global map of open water bodies reached 75%, indicating that the large omissions of the GFC-datamask and of the GIW v1.0 were effectively compensated for.

The OA obtained with the third accuracy analysis based on the 234 samples corresponding to temporary water was 79%, 89%, 94% and 99% for the SAR-WBI, the GIW v1.0, the CCI global map of open water bodies and the GFC-datamask, respectively. This ranking was in line with the results highlighted in Table 4.3. The GFC-datamask tended to map a minimum water extent and always showed low rates of water commission (high UA). These results will be discussed in the next section.

4.4 Discussion

4.4.1 Confidence-based stratification

In this study, we proposed a rigorous stratified random sampling designed for the quality assessment of a binary classification where one class is marginally distributed. It is also interesting to evaluate to what extent the random sampling scheme is representative of the correctly and incorrectly classified pixels of the validated product as it highlights the actual precision of accuracy indices. Table

4.5 gives the probability to sample pixels, correctly or incorrectly classified as water or land, according to the results of class distribution for the three different random sampling schemes. With the simple random sampling, there is an equal probability to sample any pixel of the map. The two other sampling schemes, which are stratified, first distribute the sample points according to a given value of the map. For the commonly-used class-based stratified sampling scheme, half of the sampling pixels would have been randomly selected inside the water class of the CCI global map of open water bodies, and the other half would fall in the land class. Our proposed sampling scheme used three strata resulting from the combination of independent global water datasets: half of the samples have been selected in the error-prone areas (Stratum 3), while both areas with high confidence in correctly mapping land (Stratum 1) or water (Stratum 2) received one quarter of the samples.

Table 4.5: Probability, in percent (%), to sample correctly and incorrectly classified pixels depending on the sampling scheme.

Random sampling scheme	Land correct	Water correct	Water omission	Water commission	Water correct and incorrect
Simple	96.5	2.8	0.2	0.5	3.3
Class-based stratified	49.9	42.7	0.1	7.3	50
Confidence-based stratified	59.4	33.5	3.5	3.6	37.1

The probability to capture incorrectly classified pixels in any of the random sampling schemes was low when the overall accuracy was large (OA of 99%). Compared with a simple random sampling and a class-based stratified random sampling, the probability of 3.5% to sample cases of water omission allowed to verify a posteriori that the use of a confidence-based stratification improved the precision of the producer accuracy estimation. Indeed, while the class-based stratified sampling allowed sampling more in the marginal class (50%), it further reduced the probability to detect water omission. The stratification using confidence-based strata increased the probability to sample the two types of incorrectly classified pixels. The efficiency of sample distribution for water omission and commission was dependent on the datasets used in the stratification.

The proposed stratification relied on independent datasets that are not always available. This can be an obstacle for the assessment of individual maps, but in the case of a comparison between products, the area of discrepancy could also be derived from the difference between products. Congalton and Green (2009) also suggested that the rarity of one class could be compensated by strata defined by expert-based knowledge. For instance, in the validation of land cover change, they used a buffer surrounding the change mask or land cover classes where change was more likely to occur in order to stratify the sampling of a change/no change map.

4.4.2 Permanent versus temporary water bodies

According to the Food and Agriculture Organization (FAO) Land Cover Classification System (LCCS) (Di Gregorio, 2005), identified as the most appropriate land cover classification system (Herold *et al.*, 2008), non-perennial, *i.e.* temporary or seasonal, water corresponds to a surface covered with water during less than three months a year. While it is possible to access to several historical imagery of Google Earth through the time slider, a threshold of three months could not strictly be verified due to the lack of historical imagery, regularly spread along the year. However, the interpretation of the context enabled recording information on temporary water and, by visual interpretation, it was possible to identify water presence at the time of imaging, but also surfaces that can be seasonally flooded according to water availability.

Currently, no water body product provides an LCCS-compatible definition of the water status, *i.e.*, temporary or permanent. Yet, water body products, including the SAR-WBI, GIW v1.0 and the GFC-datamask, define water using thresholds on the water detection generated on multi-temporal series of images.

Differentiating permanent from temporary water bodies could not be achieved in the GIW v1.0 using the GLS data collection for the 2000 epoch only. Based on the 234 validation samples corresponding to temporary water, 11% were mapped as water in the GIW v1.0 (Section 4.3). This issue of water seasonality was already mentioned (Feng *et al.*, 2016), and the area of temporary water included in the GIW v1.0 was evaluated as 0.17 million km^2 (Yamazaki *et al.*, 2015). In addition, the number and time spread of the GLS images limited the GIW v1.0 completeness to 91% of the terrestrial surface.

Although both the GFC-datamask and the SAR-WBI relied on multi-temporal images over several years, the GFC-datamask was more representative of permanent water. The reason is that the GFC-datamask definition of water is based on a stricter threshold on the number of water detection in the image time series. Due to such a criteria, the GFC-datamask missed water bodies created towards the end of the time period covered by the Landsat data. These water bodies such as new dams are permanent, but have a minor contribution to the water frequency in the multi-temporal dataset.

Combining an inter-annual analysis of water occurrence using multi-temporal images over several years with an intra-annual analysis of water occurrence is key to a LCCS-compatible differentiation of permanent and temporary water bodies.

4.5 Conclusions

This research has proposed an original sampling scheme for a better documentation of the product quality and a better differentiation among them based on their quality. A confidence-based stratified random sampling was developed to avoid undersampling rarely occurring map classes such as "water". The stratification was based on the a priori confidence of correctly representing map classes as defined by independent water body maps. It resulted in 3 strata corresponding to land agreement between the maps (stratum 1), to water agree-

ment between the maps (stratum 2) and to discrepancies between the maps (stratum 3). The CCI global map of open water bodies and its constitutive inputs were thoroughly validated against an independent reference database of 2110 samples spread over all land masses excluding polar regions. Using all samples, overall accuracy was always very high among all products, between 98 and 100%. The CCI global map of open water bodies provided the best water class representation (F-score of 89%) compared to its constitutive inputs but it tended to slightly overestimate the water area (User Accuracy of 86%). When focusing on the challenging areas for water bodies mapping (stratum 3) such as shorelines, lakes and rivers banks, all products yielded substantially lower accuracy figures with overall accuracies ranging between 74% and 89%. The CCI global map of open water bodies producer accuracy for class water (75%) was higher than the producer accuracies of its constitutive inputs ranging between 23% and 67%. This indicated that the large omissions of its input products were effectively compensated for by their combination. The OA obtained based on the 234 samples corresponding to temporary water was 94% for the CCI global map of open water bodies. The method could be applied to other binary under-represented classes such as burned areas.

Conclusions and perspectives

Synthesis

Detailed maps of surface water are crucial for many studies of Earth sciences, however the global water body distribution has not been clearly described yet (Yamazaki and Trigg, 2016). Scientists have developed methods to map water bodies using satellite observation by detecting the characteristic reflectance of sunlight from water. However, this is a particularly challenging task because the water color varies greatly depending on depth, suspended sediments, dissolve chemicals, along with observation conditions and sensors used. In addition, some land surfaces have similar characteristics as water, which means that water-detection algorithm efficiency is frequently context limited. This thesis contributes to address the surface water mapping consistently across different spatial and temporal scales, in various environmental contexts and over time using different sensors and appropriated methods.

The frameworks developed in this thesis are summarized in Table 4.6 with their specificities as spatial resolution, observation sources, observation frequency, extent and finally their potential applications. The thesis objective was more specifically structured in three research questions that are addressed hereafter from the results obtained in the thesis.

Table 4.6: Thesis results by chapter along with their specificities for water mapping: spatial resolution, observation sources, observation frequency, extent and finally the water body specific type which could be mapped along with the potential applications.

Chapter	**1**	**2**	**3**	**4**
Achievement	Update hyperspatial WB map with heterogeneous data	Characterize minimum size WB detection of Sentinel-2	Monitor WB along the years with twice-daily data	Robust validation of global WB map
Spatial resolution	1 m	10 m	250 m	150 m
Observation sources	Aerial VIS-NIR & LiDAR	Product: existing products / Validation : VHR photo-interpretation	Multispectral satellite VIS-NIR-SWIR-THERMAL (MODIS)	Multispectral satellite VIS-NIR-SWIR (Sentinel-2, Landsat-8, SPOT5)
Observation frequency	1 / year	1 / 10 days (1/5 days with S-2B)	2 / day	1 time
Extent	Regional	Regional-Continental	Continental-Global	Global
Water body type	Small ponds, potholes, small rivers, streams.	Lakes, rivers, large ponds. Permanent and seasonal in not cloudy region.	Major lakes, rivers and reservoirs. Permanent and seasonal.	Permanent
Application	Baseline mapping, CAP, biodiversity, landscape ecology.	Mapping, monitoring, biodiversity, landscape ecology.	Long term monitoring, anomaly, flood, food security (pastoral zone).	Product comparison and improvement, improve area estimation.

How to map surface water consistently across time and spatial scales?

According to the FAO-LCCS (Di Gregorio, 2005), identified as the most appropriate land cover classification system (Herold *et al.*, 2008), the water body class is defined and described by 5 properties (physical status, persistence, depth, sediment load and salinity) which are difficult to estimate with current remote sensing systems especially over heterogeneous and large extents. This explains why, in the remote sensing literature, the water body definition is usually linked to the observation type and availability, the sensor limitation and the spatio-temporal scale of observation.

Through different time and spatial scales, this thesis addresses the inland surface water definition with mapping methodologies to reduce inherent limitations coming from the specific scales considered. At the end of this thesis, we stand for a surface water definition based on land-water delineation, water pixel fraction and temporal behavior.

First, the land-water delineation could vary according to the water observation and is influenced by its cover such as trees, hedges, buildings, bridge but also by the parallax, the floating objects and the neighboring cover. From a remote sensing point of view, the land-water delineation is either open to the sky (visible from above), either not. This difference is well depicted in the first chapter where the water bodies are detected with sub-meter resolution using visible NIR aerial photos and aerial LiDAR. We propose a land-water delineation definition not limited to what is visible from above but defined as the physical limit of the water bodies.

Second, water body should be defined in terms of sub-pixel water cover fraction. The results of chapter 2 show that for particular shape of water body, even a pixel fully covered by water may not be detected depending on the sensor and water body's neighborhood. This is caused by the high absorptance of the light by the water in comparison with other land surfaces. By studying the sub-pixel water detection potential for three sensors and tackling their limit depiction capabilities, we highlight that what a sensor is able to detect could be much influenced from its neighboring. This is particularly important for water bodies with a size close to the resolution of the sensor. However, in chapter 3 and 4, accuracy assessments were done by sampling of very high resolution photo interpretation pixel footprints. When at least half of the pixel footprint was covered by water, it was labelled as water. In the light of results from chapter 2 and in spite of the validation protocol, we stand for a water coverage definition corresponding to a pixel fully covered by water because of the intrinsic water reflectance properties in the optical domains.

A third component of the water definition is its temporal behavior: seasonal or permanent. In order to characterize the seasonality of a water body, the 10-day water states were smoothed on pluri-annual time series in chapter 3. Such seasonality definition provides a more robust characterization of the water content along time of a given location and permits to derive the mean annual water occurrence. Based on this study, we stand for a definition of seasonal

water when mean annual occurrence is smaller than 90% and for permanent water if it is greater than 90%.

We therefore conclude that, for the sake of consistency across scales, the water surface is defined by the physical limits of the water surface, whatever they are visible or not from above, during a decade or the year round with an extent within a pixel footprint corresponding to the pixel area.

Can water body mapping be consistent using different Earth observation sources?

In this thesis, a framework to update hyperspatial water map by handling multi-source and heterogeneous data is proposed and applied in chapter 1. The originality of this framework is its consideration for observation condition variability from sensors as well as from the contextual heterogeneity of each water body. Over large areas, data acquisition was done with different instruments in heterogeneous conditions over optically disparate water bodies. By proposing a framework removing those sources of large variability, it was demonstrated that methods could be applied over large extent resulting in consistent water map over large areas. The consistency and the accuracy of water map were improved by both sources of data – multispectral and LiDAR. Thanks to the multiple echoes, the LiDAR pulses could reach the soil while the passive imagery captures the overlapping elements such as the tree canopy. However, water bodies are only indirectly detected by LiDAR as the pulses are almost fully absorbed by water leading to large commission with other surfaces absorbing most of the pulses. The discrepancies between LiDAR and passive imagery are precisely used as two complementary sources and permit to better map surface water.

The method developed in chapter 2, which characterizes the minimum sub-pixel water feature detectable by a sensor, contributes to address the notion of mapping consistency between sensors. The framework combines a spectral separability analysis and an empirical PSF estimation. In this chapter, the generic proposed method is applied to compare the Landsat-8, SPOT-5 and Sentinel-2 limits for water sub-pixel detection. The results show that any of these sensors detect sub-pixel water consistently. More specifically, the results obtained with regards to water detection suggest that isolated sub-pixel ponds are detectable using 20-m Red-Edge and SWIR Sentinel-2 bands with a minimum size of 16.7 m and 19.5 m respectively but are not detectable using 10-m band such as NIR which is not able to detect ponds smaller than 12.5 m. If linear objects such as rivers are considered, the 10-m NIR band permits the detection of standing water of 6-m width thanks to the contributions of the neighboring water pixel PSF. Finally, by putting forward a method to assess the operational capability of a given sensor to detect sub-pixel water accurately, this result proposes methods to adjust a minimum mapping unit matching the pixel area for the water.

In chapter 3, the African water bodies were monitored twice-daily with two satellites (Aqua and Terra) and provided several indicators over 7 years. The

coherence in time and with other products based on SPOT-VGT, SRTM and MODIS are assessed. In addition, the seasonality information was also found consistent with the Köppen climatic classes. Finally, the transferability of the method to other sensors (PROBA-V and SPOT-VGT) is discussed and shows that in order to have consistent mapping of water, the Hue-Value thresholds should be adapted for each sensor to have a coherent water mapping.

Finally, thanks to the improvement of accuracy assessment method designed for surface water in chapter 4, coherence of water map from different sources could be better compared thanks to the proposed biased stratified sampling on error prone areas. In this study, a rigorous stratified random sampling designed for the quality assessment of a binary classification where one class is marginally distributed is used to compare products obtained from different sensors. It also allows evaluating to what extent the random sampling scheme is representative of the correctly and incorrectly classified pixels of the products.

In conclusion, a consistent mapping with different Earth observation sources is possible if the heterogeneity of the observation and of the sensor is taken into account. Even more interestingly, different Earth observation sources provide different components that permit to define water in terms of spatial limit, temporal behavior and water, matching the definition proposed in the first research question.

Can we map all the water bodies with similar performance despite their large optical properties diversity?

The chemical components and the morphology of the water body vary according to their surrounding neighborhood. Although efficient site-and-sensor specific water bodies mapping methods have been already developed, no generic approach providing a consensus among researchers and stakeholders offers an accurate mapping without local fine-tuning. This thesis contributes to develop several remote sensing mapping methods dealing with their surroundings and with landscape heterogeneity.

The results obtained in chapter 1 show that an unsupervised clustering of hyperspatial with a high number of clusters (500) on several spatial strata (36) permits to take into account the large spectral heterogeneity of water bodies. There were between 1 to 26 water clusters per stratum corresponding to water revealing the spectral reflectance diversity of water bodies. Over a large extent with heterogeneous biogeochemical concentration, one cluster of water is thus not sufficient to cover the spectral variability of water. The proposed framework detects 83% of the water bodies and more than 98% of those water bodies greater than 100 m^2, with an edge accuracy below 1 m.

In chapter 3, we demonstrate the usefulness of a colorimetric transformation to have temporal coherent detection across a continental scale and along time. However, to grasp the heterogeneous water body and limit false detections at global scale, we demonstrate that using single thresholds in the Hue-Value domain should be mitigated by adequate measures to limit false detection such

as a layer masking false detection on glaciers, high slopes, high altitudes and on systematic error of the algorithm.

Finally, by focusing validation on the challenging areas for water bodies mapping such as shorelines, lakes and rivers banks, the assessed products yield substantially lower accuracy figures with overall accuracies ranging between 74% and 89% whereas it was ranging between 98% and 100% when using all the samples. The proposed validation permits to better characterize the water maps by oversampling in challenging landscapes and disagreement regions.

Perspectives

Potential improvements to the water surface mapping and monitoring could be summarized in the five sections below. As described in the introduction, the Big Data challenges were a unifying thread in this thesis and are characterized by the 5 "V"s (volume, variety, velocity, veracity and value). However, some challenges remain for each "V".

Data availability and usability

One of the major limitations of water mapping and monitoring during the last decades was the limited data availability.

First, because most of the existing remote sensors were not designed as operational systems but dedicated to research or to technology demonstration. Therefore, acquisition was not often systematic. Over the very recent years, this has changed and will continue to change in particular thanks to the EU Copernicus program and the sentinel fleet. Recent high resolution sensors (such as Landsat-8, Sentinel-1, Sentinel-2) and medium resolution sensors (such as PROBA-V, Sentinel-3) were launched or will be launched soon and provide unprecedented sources of information about Earth. In addition, the Copernicus Data Policy (EU No 1159/2013) provides open and free access to Sentinel products for any user. In the current operations context, it is projected that the volume of Sentinel data available to users will increase at a rate of approximately 10 PB per year once the Sentinels missions will have reached their full operational capacity. This tsunami of data clearly corresponds to the *volume* feature of the Big Data and remains a challenge to address in the future.

The second reason of lack of data consists in the difficulties to exploit the data impacted by the atmospheric conditions, especially for optical sensors. As illustrated in this thesis, the cloudiness reduces drastically the effective valid acquisitions over certain areas of the world. Although this problem was clearly identified decades ago, removal of atmospheric effects to obtain top of canopy reflectance remains a major challenge for the Committee on Earth Observation Satellites (CEOS) community moving towards "analysis-ready data" thanks to the large amount of continuous acquisitions. This limitation corresponds to the *value* feature of the Big Data challenge and was defined as information to be provided clear and useful.

In addition to the data availability, the improvement of synergies between dataset could improve the water mapping substantially. Integration of similar data such as Landsat-8 and Sentinel-2 are currently being developed (Masek *et al.*, 2016) and could improve the data usability substantially.

Improving synergies

Another important feature of the Big Data is the *variety* of the data. This variety could come from different data sources, different spatial resolutions and different data types.

Synergies between complementary data sources such as SAR and optical, LiDAR and optical as well as thermal and optical are promising. Future missions, such as SAR altimetry of Sentinel-3 or like the Surface Water Ocean Topography (SWOT) mission – a SAR with an interferometry mode to be launched in 2020 – will provide the community with high spatial resolution and temporal sampling of the continental surface water (Prigent *et al.*, 2015). This SAR will provide the volume change over surface water in time and could therefore be used by hydrologists.

Furthermore, synergies between different spatial resolution, in particular between medium resolution and high resolution should be exploited systematically in the future because it could benefit from the high spatial resolution for delimitation and from higher temporal revisit frequency of the medium resolution for monitoring.

Another important data source to use with remote sensing are low-cost in-situ data that are needed to create accurate and well-validated environmental monitoring products. Building the citizen observatory network (Hemment *et al.*, 2016) for Land Use and Land Cover monitoring is thus a key for the future.

Scientific communities

The scientific communities linked to the inland water remote sensing are numerous and include remote sensing itself, climate science, oceanography, marine science, limnology, environment, biology, engineering, signal and image processing, as well as coastal, rivers, wetlands science.

Inland water remote sensing has historically been considered mainly locally or regionally while ocean is usually considered globally. Research on the remote sensing of inland water has been undertaken at the same time as that in ocean color science, but whereas satellite observations are used operationally to measure ocean color, their use for monitoring inland waters has made less progress (Palmer *et al.*, 2015). Inland water research faced many challenges in terms of science but has also suffered from the lack of funding, infrastructure as well as from a fragmented scientific community. Bukata (2013) proposes an introspection on remote sensing of inland water and described the isolationist chasm between oceanographers and limnologists. Most of the preponderant researches carried out by the limnologists between 1970 and 2000 addressing every issue linked to optically water complex were ignored by oceanographers whereas the lake researchers had limited understanding of remote sensing.

Nevertheless, Downing (2014) indicates that two irresistible forces are drawing limnology and oceanography back together because scientists now realize that many ecosystems function in similar ways and can share a common theoretical foundation. Moreover, most oceans are suffering from the same threats as inland waters have been for centuries.

To conclude, the fragmented nature of scientific community and its fractured funding have limited the development of inland water remote sensing despite their recently well recognized importance to global processes (Tranvik *et al.*, 2009). However, recent growing awareness from the scientific communities has

induced the beginning of integration of the different disciplines together for the study of surface waters by remote sensing (Downing *et al.*, 2006).

Synergies between scientific communities of land cover, limnology and oceanography could be beneficial to develop methods and systems able to retrieve parameters linked to water quality over a large scale. Approaches to obtain variables about water quality usually need to be calibrated from ground sensor and should therefore be organized on a global network.

Seasonal water validation

Furthermore, although seasonal water bodies products became available by the end of 2016 (Donchyts *et al.*, 2016; Pekel *et al.*, 2016), robust validation of seasonal water is still missing to properly address the *veracity* challenge of the Big Data. Assessment approach such as proposed by Boschetti *et al.* (2016) for burned areas could be an interesting way to integrate the time in the sampling design. This method could be used to validate medium resolution products and be adapted to take into account the missing or cloudy observations in the Landsat or Sentinel-2 archives which is currently not the case.

New processing capacities

In addition to new sensors, new processing capacities could improve the mapping capability and thus address the *volume* and *velocity* features of the Big Data. It is particularly well illustrated in two recent papers (Donchyts *et al.*, 2016; Pekel *et al.*, 2016) using the Landsat archive to map global surface water between 1984 and 2015. To handle this petabyte-scale data set, the authors used Google Earth Engine, a freely available cloud-computing platform for analyzing big data sets of satellite observations (Yamazaki and Trigg, 2016). Pekel *et al.* (2016) completed this important achievement and opened new perspectives for researchers. Nevertheless, a philosophical and legal issue about the intellectual properties of the code and the infrastructure dependence[‡] opens a lot of critical questions for scientific community as addressed by Inglada (2016a,b).

Recently, to address this challenge, the European Commission has envisaged the creation of the Copernicus Data and Information Access Services Operations (DIAS), making Copernicus data and information available to users through a cloud-based architecture. This is the reason why an ESA call named *Copernicus Data And Information Access Services Operations* was opened. This is the procurement of the Copernicus DIAS back-office operations as a service. This includes in particular the availability of Copernicus data and information for local use on the Copernicus DIAS platform by users and the establishment and operations of the interfaces enabling an efficient access to the Copernicus DIAS data offer.

To conclude, this should ensure the use of EO products for anybody but requires solving three challenging issues: (i) selection of the product types which

[‡] The Terms of Services (`https://earthengine.google.com/terms/`) indicate that "Google owns all Intellectual Property Rights in the Services and Software" and that "Google may discontinue any Services or any portion or feature for any reason at any time without liability to Customer".

enhance the EO exploitation, (ii) select the most appropriate algorithm for these products and (iii) not killing the SME sector.

Towards operational applications

This thesis provides general and specific contributions.

First, indirectly, this research participated to achieve SDG Goal 6, which includes a focus on preserving our freshwater resources. It also contributes to the System of Environmental-Economic Accounting (SEEA)-Water asset boundary of water resources as it includes all inland bodies of water, namely, surface water (rivers, lakes, artificial reservoirs, glaciers, snow and ice) (DESA, 2012). Indeed by improving water mapping methodologies and improving water surface estimation, this thesis provides methods to better quantify the water resource evolution and therefore achieve sustainable development goals.

Second, in addition to the scientific results and achievements, this thesis contributed to the building and implementation of specific operational systems from local to global scale.

The framework developed in chapter 1 permitted to update the Walloon region map of small water bodies for the Walloon administration in the framework of the *OrthoWatch* project. As summarized in Table 4.6, the small ponds, potholes, small rivers and streams can now be mapped and updated annually. This is particularly useful for topographic maps, to monitor the agri-environmental measures supported by the CAP and its greening aspects, but also for landscape ecology studies.

Furthermore, the results obtained in chapter 3 demonstrates a water monitoring approach in the *Geoland-2* project which evolved to *Global Monitoring for Environment and Security (GMES) Initial Operations* (Global Land - Water body Version 2) using PROBA-V. This approach was used on the field to set up a pastoral surveillance system by Action Contre la Faim (ACF) (Ham and Fillol, 2011). This approach is still evolving and should be used for Sentinel-3 in the future. As summarized in Table 4.6, this approach is dedicated to monitor globally the major lakes, rivers and reservoirs. It is used for anomaly monitoring, to study climate change, to monitor flood and also as a proxy for food security, *i.e.* availability of water for cattle in pastoral zones in Sahel.

Finally, the method developed in chapter 4 characterizes the global ESA CCI water body map developed by the *ESA-CCI Land Cover project* which is now used by the climate modeling community such as in Georgievski *et al.* (2016).

Epilogue

After having read this thesis, mapping and monitoring water body consistently across different spatio-temporal scales appears to become a reality even if reliable surface water measurements are not yet automatic and complete. The current time represents a unique momentum for the scientific community as Earth observing systems are moving from experimental to operational global capacity.

Therefore, it is now time to put the puzzle together between different sensor capacities and scientific communities to provide an unprecedented surface water monitoring capacity enabling us to watch the ecosystem functioning, monitor the environmental adjustment and face the climate changes. This is crucial to assure a sustainable use of precious water resources for the future generations.

References

Achanta, R., Shaji, A., Smith, K., Lucchi, A., Fua, P., and Süsstrunk, S. 2012. SLIC superpixels compared to state-of-the-art superpixel methods. IEEE transactions on pattern analysis and machine intelligence, 34(11):2274–2282.

Alsdorf, D. E. and Lettenmaier, D. P. 2003. Tracking fresh water from space. Science, 301(5639):1491–1494.

Alsdorf, D. E., Rodriguez, E., and Lettenmaier, D. P. 2007. Measuring surface water from space. Reviews of Geophysics, 45(2):1–24.

Arino, O., Bicheron, P., Achard, F., Latham, J., Witt, R., and Weber, J.-L. 2008. The most detailed portrait of Earth. Eur. Space Agency, 136:25–31.

Atzberger, C. and Eilers, P. H. 2011. Evaluating the effectiveness of smoothing algorithms in the absence of ground reference measurements. International Journal of Remote Sensing, 32(13):3689–3709.

Bargellini. 2016. Big Data from Space: the Copernicus contribution. Big Data from Space 2016 Conference. Santa Cruz de Tenerife, Spain, from 15 to 17 March 2016.

Bartholomé, E. 2008. Monitoring the environment in Africa: The VGT4Africa and the AMESD projects. Proceedings of the 2nd International Workshop on "Crop and Rangeland Monitoring in East Africa", Nairobi 27-29 March 2007.- Office for Official Publications of the European Commission, Luxembourg EUR 23546-2008, pages 303–319.

Bartholomé, E. and Belward, A. S. 2005. GLC2000: a new approach to global land cover mapping from Earth observation data. International Journal of Remote Sensing, 26(9):1959–1977.

Bartsch, A., Trofaier, A., Hayman, G., Sabel, D., Schlaffer, S., Clark, D., and Blyth, E. 2012. Detection of open water dynamics with ENVISAT ASAR in support of land surface modelling at high latitudes. Biogeosciences, 9(2):703–714.

Bates, B., Kundzewicz, Z. W., Wu, S., and Palutikof, J. 2008. *climate change and Water: technical Paper vi*. Intergovernmental Panel on Climate Change (IPCC).

Beyer, M. A. and Laney, D. 2012. The importance of 'big data': a definition. Stamford, CT: Gartner, pages 2014–2018.

Bigdeli, B. 2014. A decision fusion method based on multiple support vector machine system for fusion of hyperspectral and LIDAR data. ... of Image and Data Fusion.

Blaschke, T. 2010. Object based image analysis for remote sensing. ISPRS journal of photogrammetry and remote sensing, 65(1):2–16.

Bochow, M., Heim, B., Küster, T., Rogaß, C., Bartsch, I., Segl, K., Reigber, S., and Kaufmann, H. 2012. *On the use of airborne imaging spectroscopy data for the automatic detection and delineation of surface water bodies*. InTech.

Borges, A. V., Darchambeau, F., Teodoru, C. R., Marwick, T. R., Tamooh, F., Geeraert, N., Omengo, F. O., Guérin, F., Lambert, T., Morana, C., *et al.*. 2015. Globally significant greenhouse-gas emissions from African inland waters. Nature Geoscience, 8(8):637–642.

Bork, E. W. and Su, J. G. 2007. Integrating LIDAR data and multispectral imagery for enhanced classification of rangeland vegetation: A meta analysis. Remote Sensing of Environment, 111(1):11–24.

Boschetti, L., Stehman, S. V., and Roy, D. P. 2016. A stratified random sampling design in space and time for regional to global scale burned area product validation. Remote Sensing of Environment, 186:465–478.

Boucher, A. 2007. Downscaling of Satellite remote sensing data: application to land cover mapping. Stanford University, (August):143.

Brönmark, C. and Hansson, L.-A. 2002. Environmental issues in lakes and ponds: current state and perspectives. Environmental Conservation, 29(3):290–306.

Brzank, A. and Heipke, C. 2006. Classification of lidar data into water and land points in coastal areas. International Archives of Photogrammetry and Remote Sensing, 36(3):197–202.

Bukata, R. P. 2013. Retrospection and introspection on remote sensing of inland water quality:"Like Déjà Vu all over again". Journal of Great Lakes Research, 39:2–5.

Campagnolo, M. L. and Montano, E. L. 2014. Estimation of effective resolution for daily MODIS gridded surface reflectance products. Geoscience and Remote Sensing, IEEE Transactions on, 52(9):5622–5632.

Campbell, J. B. and Wynne, R. H. 2011. *Introduction to remote sensing*. Guilford Press.

Carbonneau, P. and Lane, S. 2006. Feature based image processing methods applied to bathymetric measurements from airborne remote sensing in fluvial environments. Earth Surface Processes.

Carbonneau, P. E., Lane, S. N., and Bergeron, N. E. 2004. Catchment-scale mapping of surface grain size in gravel bed rivers using airborne digital imagery. Water resources research, 40(7).

Carpenter, S. R., Stanley, E. H., and Vander Zanden, M. J. 2011. State of the world's freshwater ecosystems: physical, chemical, and biological changes. Annual review of Environment and Resources, 36:75–99.

Carroll, M., Townshend, J. R., DiMiceli, C. M., Noojipady, P., and Sohlberg, R. 2009. A new global raster water mask at 250 m resolution. International Journal of Digital Earth, 2(4):291–308.

Carvalho, L., McDonald, C., Hoyos, C., Mischke, U., Phillips, G., Borics, G., Poikane, S., Skjelbred, B., Solheim, A. L., Wichelen, J., *et al.*. 2013. Sustaining recreational quality of European lakes: minimizing the health risks from algal blooms through phosphorus control. Journal of Applied Ecology, 50(2):315–323.

Chen, J. M. 1999. Spatial scaling of a remotely sensed surface parameter by contexture. Remote Sensing of Environment, 69(1):30–42.

Chen, Y., Su, W., Li, J., and Sun, Z. 2009. Hierarchical object oriented classification using very high resolution imagery and LIDAR data over urban areas. Advances in Space Research, 43(7):1101–1110.

Clandillon, S., Fraipont, P., and Yésou, H. 1995. Assessment of the future SPOT 4 MIR for wetland monitoring and soil moisture analysis: simulation over the Ried Center Alsace (France). In *Satellite Remote Sensing II*, pages 102–111. International Society for Optics and Photonics.

Collen, B., Whitton, F., Dyer, E. E., Baillie, J. E., Cumberlidge, N., Darwall, W. R., Pollock, C., Richman, N. I., Soulsby, A.-M., and Böhm, M. 2014. Global patterns of freshwater species diversity, threat and endemism. Global Ecology and Biogeography, 23(1):40–51.

Congalton, R. and Green, K. 2009. *Assessing the Accuracy of Remotely Sensed Data: Principles and Practices*. Mapping Science Series. CRC Press/Taylor & Francis.

Congalton, R. G. 1988. A comparison of sampling schemes used in generating error matrices for assessing the accuracy of maps generated from remotely sensed data. Photogrammetric engineering and remote sensing (USA).

Congalton, R. G., Birch, K., Jones, R., and Schriever, J. 2002. Evaluating remotely sensed techniques for mapping riparian vegetation. Computers and Electronics in Agriculture, 37(1):113–126.

Crétaux, J.-F., Abarca-del Río, R., Berge-Nguyen, M., Arsen, A., Drolon, V., Clos, G., and Maisongrande, P. 2016. Lake Volume Monitoring from Space. Surveys in Geophysics, 37(2):269–305.

Csillik, O. 2017. Fast Segmentation and Classification of Very High Resolution Remote Sensing Data Using SLIC Superpixels. Remote Sensing, 9(3):243.

d'Andrimont, R., Pekel, J.-F., Van Bogaert, E., and Defourny, P. 2010. Monitoring water bodies over whole Africa in near real time: detection algorithms and preliminary results. In *Advances in Quantitative Remote Sensing (RAQRS) 3rd international symposium*.

d'Andrimont, R., Pekel, J.-F., and Defourny, P. 2011b. Monitoring African surface water dynamic using medium resolution daily data allows anomalies detection in nearly real time. In *Analysis of Multi-temporal Remote Sensing Images (Multi-Temp), 2011 6th International Workshop on the*, pages 241–244. IEEE.

Dare, P. M. 2005. Shadow analysis in high-resolution satellite imagery of urban areas. Photogrammetric Engineering & Remote Sensing, 71(2):169–177.

Davis, T. 1994. The Ramsar Convention manual: a guide to the convention on wetlands of international importance especially as waterfowl habitat.

De Lussy, F., Greslou, D., Dechoz, C., Amberg, V., Delvit, J. M., Lebegue, L., Blanchet, G., and Fourest, S. 2012. Pleiades HR in flight geometrical calibration: Location and mapping of the focal plane. Int. Arch. Photogramm. Remote Sens. Spat. Inf. Sci, 39:519–523.

Defourny, P., Vancutsem, C., Bicheron, P., Brockmann, C., Nino, F., Schouten, L., Leroy, M., *et al.*. 2006. GLOBCOVER: a 300 m global land cover product for 2005 using Envisat MERIS time series. In *Proceedings of the ISPRS Commission VII mid-term symposium, Remote sensing: from pixels to processes*, pages 8–11. Citeseer.

Defourny, P., Bicheron, P., Brockman, C., Bontemps, S., Van Bogaert, E., Vancutsem, C., Pekel, J.-F., Huc, M., Henry, C., Ranera, F., *et al.*. 2009. The first 300 m global land cover map for 2005 using ENVISAT MERIS time series: A product of the GlobCover system. In *The 33rd International Symposium on Remote Sensing of Environment*.

Defourny, P., Mayaux, P., Herold, M., and Bontemps, S. 2012. 14 Global Land-Cover Map Validation Experiences: Toward the Characterization of Quantitative Uncertainty.

DESA, U. 2012. System of Environmental-Economic Accounting for Water. Statistics Division, United Nations Department of Economic and Social Affairs, New York. UNESCO (2012f) Indicators, Retrieved June, 6:2012.

Desclée, B., Bogaert, P., and Defourny, P. 2006. Forest change detection by statistical object-based method. Remote Sensing of Environment, 102(1-2):1–11.

Devred, E., Turpie, K. R., Moses, W., Klemas, V. V., Moisan, T., Babin, M., Toro-Farmer, G., Forget, M.-H., and Jo, Y.-H. 2013. Future Retrievals

of Water Column Bio-Optical Properties using the Hyperspectral Infrared Imager (HyspIRI). Remote Sensing, 5(12):6812–6837.

Di Gregorio, A. 2005. *Land cover classification system: classification concepts and user manual: LCCS*. 8. Food & Agriculture Org.

Donchyts, G., Baart, F., Winsemius, H., Gorelick, N., Kwadijk, J., and van de Giesen, N. 2016. Earth's surface water change over the past 30 years. Nature Climate Change, 6(9):810–813.

Dörnhöfer, K. and Oppelt, N. 2016. Remote sensing for lake research and monitoring–Recent advances. Ecological Indicators, 64:105–122.

Downing, J., Prairie, Y., Cole, J., Duarte, C., Tranvik, L., Striegl, R., McDowell, W., Kortelainen, P., Caraco, N., Melack, J., *et al.*. 2006. The global abundance and size distribution of lakes, ponds, and impoundments. Limnology and Oceanography, 51(5):2388–2397.

Downing, J. A. 2014. Limnology and oceanography: two estranged twins reuniting by global change. Inland Waters, 4(2):215–232.

Drusch, M., Del Bello, U., Carlier, S., Colin, O., Fernandez, A., Gascon, F., Hoersch, C., B. and. Isola, Laberinti, P., Martimort, P., Meygret, A., Spotoa, F., Sy, O., Marchese, F., and Bargellini, P. 2012. Sentinel-2: ESA's Optical High-Resolution Mission for GMES Operational Services. Remote Sensing of Environment, 120:25–36.

Du, Y., Zhang, Y., Ling, F., Wang, Q., Li, W., and Li, X. 2016. Water Bodies' Mapping from Sentinel-2 Imagery with Modified Normalized Difference Water Index at 10-m Spatial Resolution Produced by Sharpening the SWIR Band. Remote Sensing, 8(4):354.

Dudgeon, D., Arthington, A. H., Gessner, M. O., Kawabata, Z.-I., Knowler, D. J., Lévêque, C., Naiman, R. J., Prieur-Richard, A.-H., Soto, D., Stiassny, M. L. J., and Sullivan, C. A. 2006. Freshwater biodiversity: importance, threats, status and conservation challenges. Biological Reviews, 81:163–182.

Duveiller, G., Baret, F., and Defourny, P. 2011. Crop specific green area index retrieval from MODIS data at regional scale by controlling pixel-target adequacy. Remote Sensing of Environment, 115(10):2686–2701.

Eilers, P. H. C. 2003. A perfect smoother. Analytical Chemistry, 75(14):3631–3636.

Elaksher, A. F. 2008. Fusion of hyperspectral images and lidar-based dems for coastal mapping. Optics and Lasers in Engineering, 46(7):493–498.

Ernst, J., Dewals, B., Archambeau, P., Detrembleur, S., Erpicum, S., and Pirotton, M. 2008. Integration of accurate 2D inundation modelling, vector land use database and economic damage evaluation. In *Proceedings of the European Conference on Flood Risk Management-FloodRisk 2008*, pages 1643–1653. Balkema.

ESRI. 2016. ArcGIS Desktop - Version 13 - CA: Environmental Systems Research Institute.

Estes, J. E. and Simonett, D. S. 1975. Fundamentals of image interpretation. Manual of remote sensing, pages 869–1076.

Europa-Technologies. 2014. Europa Technologies Global Insight.

Famiglietti, J., Cazenave, A., Eicker, A., Reager, J., Rodell, M., and Velicogna, I. 2015. Satellites provide the big picture. Science, 349(6249).

Farr, T. G., Rosen, P. A., Caro, E., Crippen, R., Duren, R., Hensley, S., Kobrick, M., Paller, M., Rodriguez, E., Roth, L., *et al.*. 2007. The shuttle radar topography mission. Reviews of geophysics, 45(2).

Fedorov, A. A., Barbosa, S. P., and Berberan-Santos, M. N. 2006. Radiation propagation time broadening of the instrument response function in time-resolved fluorescence spectroscopy. Chemical physics letters, 421(1):157–160.

Feng, L., Hu, C., Chen, X., Li, R., Tian, L., and Murch, B. 2011. MODIS observations of the bottom topography and its inter-annual variability of Poyang Lake. Remote sensing of environment, 115(10):2729–2741.

Feng, M., Sexton, J. O., Channan, S., and Townshend, J. R. 2016. A global, high-resolution (30-m) inland water body dataset for 2000: First results of a topographic–spectral classification algorithm. International Journal of Digital Earth, 9(2):113–133.

Foody, G. M. 2004. Thematic map comparison. Photogrammetric Engineering & Remote Sensing, 70(5):627–633.

Foody, G. M., Muslim, A. M., and Atkinson, P. M. 2005. Super-resolution mapping of the waterline from remotely sensed data. International Journal of Remote Sensing, 26(24):5381–5392.

Fox, A., Herbert, D., Fretwell, P., and Fleming, A. 2013. SCAR Antarctic Digital Database V 6.0.

Frey, R. A., Ackerman, S. A., Liu, Y., Strabala, K. I., Zhang, H., Key, J. R., and Wang, X. 2008. Cloud detection with MODIS. Part I: Improvements in the MODIS cloud mask for collection 5. Journal of Atmospheric and Oceanic Technology, 25(7):1057–1072.

Gallant, A. 2015. The Challenges of Remote Monitoring of Wetlands. Remote Sensing, 7(8):10938–10950.

Gao, B.-C. 1996. NDWI—A normalized difference water index for remote sensing of vegetation liquid water from space. Remote sensing of environment, 58(3):257–266.

Gardelle, J., Hiernaux, P., Kergoat, L., and Grippa, M. 2010. Less rain, more water in ponds: a remote sensing study of the dynamics of surface waters from 1950 to present in pastoral Sahel (Gourma region, Mali). Hydrology and Earth System Sciences, 14(2):309–324.

Gascon, F., Thépaut, O., Jung, M., Francesconi, B., Louis, J., Lonjou, V., Lafrance, B., Massera, S., Gaudel-Vacaresse, A., Languille, F., Alhammoud, B., Viallefont, F., Bieniarz, J., Pflug, B., Clerc, S., Pessiot, L., Trémas, T., Cadau, E., Bonis, R. D., Isola, C., Martimort, P., and Fernandez, V. 2016. Copernicus Sentinel-2 Calibration and Products Validation Status.

GCOS. 2011. Systematic Observation Requirements for Satellite-based Products for Climate - 2011 Update - Supplemental details to the satellite-based component of the "Implementation Plan for the Global Observing System for Climate in Support of the UNFCCC (2010 Update)". Report, GCOS secretariat,WMO-Geneva.

Geldsetzer, T., Sanden, J. v. d., and Brisco, B. 2010. Monitoring lake ice during spring melt using RADARSAT-2 SAR. Canadian journal of remote sensing, 36(sup2):S391–S400.

Geng, L., Ma, M., Wang, X., Yu, W., Jia, S., and Wang, H. 2014. Comparison of eight techniques for reconstructing multi-satellite sensor time-series NDVI data sets in the Heihe river basin, China. Remote Sensing, 6(3):2024–2049.

Georgievski, G., Hartley, A., MacBean, N., and Hagemann, S. 2016. Evaluation of the uncertainty due to land cover observation and conversion into plant functional types. In *EGU General Assembly Conference Abstracts*, volume 18, page 10349.

Giardino, C., Brando, V. E., Dekker, A. G., Strömbeck, N., and Candiani, G. 2007. Assessment of water quality in Lake Garda (Italy) using Hyperion. Remote Sensing of Environment, 109(2):183–195.

Gond, V., Bartholomé, E., Ouattara, F., Nonguierma, A., and Bado, L. 2004. Surveillance et cartographie des plans d'eau et des zones humides et inondables en régions arides avec l'instrument VEGETATION embarqué sur SPOT-4. International Journal of Remote Sensing, 25(5):987–1004.

Gond, V., Bernard, J., Brognoli, C., Brunaux, O., Coppel, A., Demenois, J., Engel, J., Galarraga, D., Gaucher, P., Guitet, S., *et al.*. 2005. Analyse multi-echelles de la caracterisation des ecosystèemes forestiers guyanais et des impacts humains à partir de la télédétection. In *Conseil Général de la Martinique, Colloque sur les Ecosystèmes Forestiers des caraïbes-Martinique*, pages 5–10.

Goodchild, M. F. and Quattrochi, D. A. 1997. Scale, multiscaling, remote sensing, and GIS.

Goovaerts, P. 2002. Geostatistical incorporation of spatial coordinates into supervised classification of hyperspectral data. Journal of Geographical Systems, 4(1):99–111.

Gordon, H. R. and Wang, M. 1994. Retrieval of water-leaving radiance and aerosol optical thickness over the oceans with SeaWiFS: a preliminary algorithm. Applied optics, 33(3):443–452.

Graitson, E. 2009. Elaboration d'un référentiel et de documents de vulgarisation sur les mares agricoles en Région wallonne : rapport final - Partie 2.

Greenberg, J., Dobrowski, S., and Ustin, S. 2005. Shadow allometry: Estimating tree structural parameters using hyperspatial image analysis. Remote Sensing of Environment.

Grosse, G., Romanovsky, V., Walter, K., Morgenstern, A., Lantuit, H., and Zimov, S. 2008. Distribution of thermokarst lakes and ponds at three yedoma sites in Siberia. Ninth International Conference On Permafrost, pages 551–556.

Guo, H., Liu, Z., Jiang, H., Wang, C., Liu, J., and Liang, D. 2017. Big Earth Data: a new challenge and opportunity for Digital Earth's development. International Journal of Digital Earth, 10(1):1–12.

Haas, E. M. 2010. Temporary water bodies as ecological indicators in West African drylands. Thesis. Université Catholique de Louvain. Available at `http://hdl.handle.net/2078.1/32210` on 2016-12-01.

Haas, E. M., Bartholomé, E., and Combal, B. 2009. Time series analysis of optical remote sensing data for the mapping of temporary surface water bodies in sub-Saharan western Africa. Journal of Hydrology, 370(1):52–63.

Haas, E. M., Bartholomé, E., Lambin, E. F., and Vanacker, V. 2011. Remotely sensed surface water extent as an indicator of short-term changes in ecohydrological processes in sub-Saharan Western Africa. Remote Sensing Of Environment.

Hagolle, O., Huc, M., Villa Pascual, D., and Dedieu, G. 2015. A Multi-Temporal and Multi-Spectral Method to Estimate Aerosol Optical Thickness over Land, for the Atmospheric Correction of FormoSat-2, LandSat, VENμS and Sentinel-2 Images. Remote Sensing, 7(3):2668–2691.

Hagolle, S., Olivier ; Sylvander, Behague, M., Hoersch, B., Koetz, B., Huc, M., Clesse, D., Desjardins, C., and Rodriguez, K. 2016. Lessons Learned from the SPOT (Take5) Experiments: Simulations of Sentinel-2 Time Series on 195 Sites. ESA.

Hallot, P. and Billen, R. 2013. Rapport final Reengineering PICC S0. 04.01-11PNSP-01.

Ham, F. and Fillol, E. 2011. 10. Pastoral surveillance system and feed inventory in the Sahel. National Feed Assessments, page 83.

Hamilton, S. K., Melack, J. M., Goodchild, M. F., and Lewis, W. 1992. Estimation of the fractal dimension of terrain from lake size distributions. Lowland floodplain rivers: Geomorphological perspectives. Wiley, pages 145–163.

Hansen, M. C., Potapov, P. V., Moore, R., Hancher, M., Turubanova, S., Tyukavina, A., Thau, D., Stehman, S., Goetz, S., Loveland, T., *et al.*. 2013. High-resolution global maps of 21st-century forest cover change. Science, 342(6160):850–853.

Haran, T., Bohlander, Scambos, Painter, and Fahnestock. 2005. MODIS Mosaic of Antarctica 2003-2004 (MOA2004) Image Map, Version 1.

Hardisky, M., Klemas, V., and Smart, R. M. 1983. The influence of soil salinity, growth form, and leaf moisture on the spectral radiance of Spartina alterniflora canopies. Photogrammetric Engineering and Remote Sensing, 49:77–83.

Hefting, M. M., van den Heuvel, R. N., and Verhoeven, J. T. 2013. Wetlands in agricultural landscapes for nitrogen attenuation and biodiversity enhancement: Opportunities and limitations. Ecological Engineering, 56:5–13.

Helder, D., Choi, T., and Rangaswamy, M. 2004. In-flight characterization of spatial quality using point spread functions. In *Proc. Int. Workshop Radiometric Geometric Calibration—In Post-Launch Calibration Satellite Sensors*, pages 151–170.

Helder, D., Choi, J., and Anderson, C. 2006. On-orbit modulation transfer function (MTF) measurements for IKONOS and QuickBird. In *Proceedings of the JACIE 2006 Civil Commercial Imagery Evaluation Workshop*, pages 14–16. sponsored by NASA/NGA/USGS (CD-ROM) Laurel, MD, USA.

Hemment, D., Amditis, A., Fritz, S., Wehn, U., Moorthy, I., and Tsertou, A. 2016. The Next Generation Citizen Observatories.

Herold, M., Mayaux, P., Woodcock, C., Baccini, A., and Schmullius, C. 2008. Some challenges in global land cover mapping: An assessment of agreement and accuracy in existing 1 km datasets. Remote Sensing of Environment, 112(5):2538–2556.

Hodgson, M. E., Jensen, J. R., Tullis, J. a., Riordan, K. D., and Archer, C. M. 2003. Synergistic Use of Lidar and Color Aerial Photography for Mapping Urban Parcel Imperviousness. Photogrammetric Engineering & Remote Sensing, 69(9):973–980.

Hofle, B., Vetter, M., Pfeifer, N., Mandlburger, G., and Stotter, J. 2009. Water surface mapping from airborne laser scanning using signal intensity and elevation data. Earth Surface Processes and Landforms, 34(12):1635.

Holgerson, M. A. and Raymond, P. A. 2016. Large contribution to inland water CO2 and CH4 emissions from very small ponds. Nature Geoscience.

Huang, C., Thomas, N., Goward, S. N., Masek, J. G., Zhu, Z., Townshend, J. R., and Vogelmann, J. E. 2010. Automated masking of cloud and cloud shadow for forest change analysis using Landsat images. International Journal of Remote Sensing, 31(20):5449–5464.

Huang, X. and Zhang, L. 2012. Morphological building/shadow index for building extraction from high-resolution imagery over urban areas. IEEE Journal of Selected Topics in Applied Earth Observations and Remote Sensing, 5(1):161–172.

Huang, X., Xie, C., Fang, X., and Zhang, L. 2015. Combining pixel-and object-based machine learning for identification of water-body types from urban high-resolution remote-sensing imagery. IEEE Journal of Selected Topics in Applied Earth Observations and Remote Sensing, 8(5):2097–2110.

Inglada, J. 2016a. Is Google Earth Engine Evil? Available at `http://jordiinglada.net/wp/2016/05/12/is-google-earth-engine-evil-2/`, Accessed 2016-12-16.

Inglada, J. 2016b. Sympathy for the Evil: let's help improve Google Earth Engine. Available at `http://jordiinglada.net/wp/2016/05/23/sympathy-for-the-evil-lets-help-improve-google-earth-engine-2/{#}fn.2`, Accessed 2016-12-16.

Inglada, J. and Christophe, E. 2009. The Orfeo Toolbox Remote Sensing Image Processing Software. IGARSS (4).

Irons, J. R., Markham, B. L., Nelson, R. F., Toll, D. L., Williams, D. L., Latty, R. S., and Stauffer, M. L. 1985. The effects of spatial resolution on the classification of Thematic Mapper data. International Journal of Remote Sensing, 6(8):1385–1403.

James, S., Michael, C., and Kenton, L. 2014. Landsat 8 Operational Land Imager On-Orbit Geometric Calibration and Performance. Remote Sensing, 6(11):11127–11152.

Jarvis, A., Reuter, H. I., Nelson, A., and Guevara, E. 2008. Hole-filled SRTM for the globe Version 4. Available from the CGIARCSI SRTM 90m Database (http://srtm.csi.cgiar.org).

Jensen, J. R. and Cowen, D. C. 1999. Remote sensing of urban/suburban infrastructure and socio-economic attributes. Photogrammetric engineering and remote sensing, 65:611–622.

Jiménez Cisneros, B. E., Fischer, T., Barros, R., Dokken, D., Mach, K., Bilir, T., Chatterjee, M., Ebi, K., Estrada, Y., Genova, R., Girma, B., Kissel, E., Levy, A., and MacCracken, S. 2014. 3 Freshwater Resources Coordinating Lead Authors: Contributing Authors. Shinjiro Kanae (Japan), pages 229–269.

Jones, K., Lanthier, Y., van der Voet, P., van Valkengoed, E., Taylor, D., and Fernández-Prieto, D. 2009. Monitoring and assessment of wetlands using Earth Observation: The GlobWetland project. Journal of Environmental Management, 90(7):2154–2169.

Joseph, G. 2000. How well do we understand Earth observation electro-optical sensor parameters? ISPRS journal of photogrammetry and remote sensing, 55(1):9–12.

Justice, C., Giglio, L., Korontzi, S., Owens, J., Morisette, J., Roy, D., Descloitres, J., Alleaume, S., Petitcolin, F., and Kaufman, Y. 2002. The MODIS fire products. Remote Sensing of Environment, 83(1):244–262.

Kay, S., Hedley, J. D., and Lavender, S. 2009. Sun glint correction of high and low spatial resolution images of aquatic scenes: A review of methods for visible and near-infrared wavelengths. Remote Sensing, 1(4):697–730.

Khlopenkov, K. V. and Trishchenko, A. P. 2007. SPARC: New cloud, snow, and cloud shadow detection scheme for historical 1-km AVHHR data over Canada. Journal of Atmospheric and Oceanic technology, 24(3):322–343.

Klein, I., Dietz, A., Gessner, U., Dech, S., and Kuenzer, C. 2015. Results of the Global WaterPack: a novel product to assess inland water body dynamics on a daily basis. Remote Sensing Letters, 6(1):78–87.

Knight, E. and Kvaran, G. 2014. Landsat-8 Operational Land Imager Design, Characterization and Performance. Remote Sensing, 6(11):10286–10305.

Kobayashi, H. and Dye, D. G. 2005. Atmospheric conditions for monitoring the long-term vegetation dynamics in the Amazon using normalized difference vegetation index. Remote Sensing of Environment, 97(4):519–525.

Kottek, M., Grieser, J., Beck, C., Rudolf, B., and Rubel, F. 2006. World map of the Koppen-Geiger climate classification updated. Meteorologische Zeitschrift, 15(3):259–263.

Kristensen, P. and Globevnik, L. 2014. European small water bodies. In *Biology and Environment: Proceedings of the Royal Irish Academy*, volume 114, pages 281–287. JSTOR.

Kuenzer, C., Guo, H., Huth, J., Leinenkugel, P., Li, X., and Dech, S. 2013. Flood mapping and flood dynamics of the Mekong Delta: ENVISAT-ASAR-WSM based time series analyses. Remote Sensing, 5(2):687–715.

Kugler, Z. and De Groeve, T. 2007. The global flood detection system. Office for Official Publications of the European Communities, Luxembourg.

Laanen, M. L. 2007. Yellow matters: improving the remote sensing of coloured dissolved organic matter in inland freshwaters. Thesis. Amsterdam: Vrije Universiteit.

Lacaux, J., Tourre, Y., Vignolles, C., Ndione, J., and Lafaye, M. 2007. Classification of ponds from high-spatial resolution remote sensing: Application to Rift Valley Fever epidemics in Senegal. Remote Sensing of Environment, 106(1):66–74.

Lacaze, R., Balsamo, G., Baret, F., Andrew, B., Calvet, J.-C., Camacho, F., D'Andrimont, R., Philippe, P., Smets, B., Poilvé, H., *et al.*. 2010. Geoland2-Towards an operational GMES land monitoring core serviceand First results of the biogeophysical parameter core mapping service.

Lacaze, R., Baret, F., Camacho, F., d'Andrimont, R., Freitas, S., Pacholczyk, P., Poilvé, H., Smets, B., Tansey, K., Wagner, W., *et al.*. 2011. geoland2–towards an operational GMES land monitoring core service: the biogeophysical parameter core mapping service. In *Proceedings of the 34th International Symposium on Remote Sensing of Environment*.

Lacaze, R., Balsamo, G., Baret, F., Calvet, J.-C., Camacho, F., d'Andrimont, R., Coelho y Freitas, S., Kidd, R., Pacholczyk, P., Polivé, H., Smets, B., and Tansey, K. 2012. The GMES Land Monitoring Service: achievements and continuity. In *AGU Fall Meeting Abstracts*, volume 1, page 1100.

Lacaze, R., Smets, B., Baret, F., Weiss, M., Ramon, D., Wandrebeck, L., Montersleet, B., Calvet, J.-C., Roujean, J.-L., Camacho, F., Trigo, I. F., Freitas, S. C., Jann, A., Paulik, C., Tansey, K., d'Andrimont, R., and Verger, A. 2014a. The operational 333M biophysical products of the Copernicus Global Land service. In *The 4th International Symposium on Recent Advances in Quantitative Remote Sensing RAQR'IV*.

Lacaze, R., Smets, B., Trigo, I. F., Freitas, S. C., Jann, A., Calvet, J.-C., Camacho, F., Baret, F., Weiss, M., de Montera, L., Roujean, J.-L., Paulik, C., d'Andrimont, R., Waldner, F., Tansey, K., Pacholczyk, P., Balsamo, G., Bousetta, S., and Sinztai, B. 2014b. Towards an operational production of 300m resolution biophysical products in the Copernicus Global Land Service. In *GV2M: Global Vegetation Monitoring and Modeling*.

Lacaze, R., Smets, B., Baret, F., Weiss, M., Ramon, D., Montersleet, B., Wandrebeck, L., Calvet, J.-C., Roujean, J.-L., and Camacho, F. 2015. Operational 333m Biophysical Products of the Copernicus Global Land Service for Agriculture Monitoring. ISPRS - International Archives of the Photogrammetry, Remote Sensing and Spatial Information Sciences, XL-7/W3(May):53–56.

Lamarche, C., Bontemps, S., Verhegghen, A., Radoux, J., Vanbogaert, E., Kalogirou, V., Seifert, F. M., Arino, O., and Defourny, P. 2013. Characterizing The Surface Dynamics For Land Cover Mapping: Current Achievements Of The ESA CCI Land Cover. In *ESA Special Publication*, volume 722, page 79.

Lamarche, C., Santoro, M., Bontemps, S., D'Andrimont, R., Radoux, J., Giustarini, L., Brockmann, C., Wevers, J., Defourny, P., and Arino, O. 2017. Compilation and Validation of SAR and Optical Data Products for a Complete and Global Map of Inland/Ocean Water Tailored to the Climate Modeling Community. Remote Sensing, 9(1):36.

Lang, M., Kuusk, A., Mõttus, M., Rautiainen, M., and Nilson, T. 2010. Canopy gap fraction estimation from digital hemispherical images using sky radiance models and a linear conversion method. Agricultural and Forest Meteorology, 150(1):20–29.

Lang, M. W. and McCarty, G. W. 2009. Lidar intensity for improved detection of inundation below the forest canopy. Wetlands, 29(4):1166–1178.

Lausch, A. and Herzog, F. 2002. Applicability of landscape metrics for the monitoring of landscape change: issues of scale, resolution and interpretability. Ecological indicators, 2(1):3–15.

Lechner, A. M., Stein, A., Jones, S. D., and Ferwerda, J. G. 2009. Remote sensing of small and linear features: quantifying the effects of patch size and length, grid position and detectability on land cover mapping. Remote Sensing of Environment, 113(10):2194–2204.

Lehner, B. and Döll, P. 2004. Development and validation of a global database of lakes, reservoirs and wetlands. Journal of Hydrology, 296(1):1–22.

Lejot, J., Delacourt, C., and Piégay, H. 2007. Very high spatial resolution imagery for channel bathymetry and topography from an unmanned mapping controlled platform. Earth Surface.

Li, D., Gong, J., and Shan, J. 2009. *Geospatial technology for earth observation*.

Li, L., Chen, Y., Yu, X., Liu, R., and Huang, C. 2015. Sub-pixel flood inundation mapping from multispectral remotely sensed images based on discrete particle swarm optimization. ISPRS Journal of Photogrammetry and Remote Sensing, 101:10–21.

Lichvar, R. W., Finnegan, D. C., Newman, S., and Ochs, W. 2006. Delineating and Evaluating Vegetation Conditions of Vernal Pools Using Spaceborne and Airborne Remote Sensing Techniques, Beale Air Force Base, CA. Technical report, DTIC Document.

Ma, B., Wu, L., Zhang, X., Li, X., Liu, Y., and Wang, S. 2014. Locally adaptive unmixing method for lake-water area extraction based on MODIS 250m bands. International Journal of Applied Earth Observation and Geoinformation, 33:109–118.

Mahalanobis, P. C. 1936. On the generalized distance in statistics. Proceedings of the National Institute of Sciences (Calcutta), 2:49–55.

Malenovsky, Z., Rott, H., Cihlar, J., Schaepman, M. E., Garcia-Santos, G., Fernandes, R., and Berger, M. 2012. Sentinels for science: potential of Sentinel-1, -2, and -3 missions for scientific observations of ocean, cryosphere, and land. Remote Sensing of Environment, 120:91–101.

Manakos, I., Chatzopoulos-Vouzoglanis, K., Petrou, Z., Filchev, L., and Apostolakis, A. 2014. Globalland30 Mapping Capacity of Land Surface Water in Thessaly, Greece. Land, 4(1):1–18.

Marceau, D. J., Gratton, D. J., Fournier, R. A., and Fortin, J.-P. 1994. Remote sensing and the measurement of geographical entities in a forested environment. 2. The optimal spatial resolution. Remote Sensing of Environment, 49(2):105–117.

Marcus, W. A. and Fonstad, M. A. 2008. Optical remote mapping of rivers at sub-meter resolutions and watershed extents. Earth Surface Processes and Landforms, 33(1):4–24.

Marcus, W. A., Crabtree, R., Aspinall, R. J., Boardman, J. W., Despain, D., Minshall, W., and Peel, J. 2000. Validation of high-resolution hyperspectral data for stream and riparian habitat analysis. NASA EOCAP Final Phase, 2.

Marcus, W. A., Legleiter, C. J., Aspinall, R. J., Boardman, J. W., and Crabtree, R. L. 2003. High spatial resolution hyperspectral mapping of in-stream habitats, depths, and woody debris in mountain streams. Geomorphology, 55(1):363–380.

Markham, B. and Townshend, J. 1981. Land cover classification accuracy as a function of sensor spatial resolution. XV International Symposium on Remote Sensing of Environment, Ann Arbor.

Martinis, S., Twele, A., and Voigt, S. 2011. Unsupervised extraction of flood-induced backscatter changes in SAR data using Markov image modeling on irregular graphs. Geoscience and Remote Sensing, IEEE Transactions on, 49(1):251–263.

Martinis, S., Twele, A., Strobl, C., Kersten, J., and Stein, E. 2013. A Multi-Scale Flood Monitoring System Based on Fully Automatic MODIS and TerraSAR-X Processing Chains. Remote Sensing, 5(11):5598–5619.

Marton, J. M., Creed, I. F., Lewis, D. B., Lane, C. R., Basu, N. B., Cohen, M. J., and Craft, C. B. 2015. Geographically Isolated Wetlands are Important Biogeochemical Reactors on the Landscape. BioScience, 65(4):408–418.

Masek, J., Vermote, E., Franch, B., Roger, J.-C., Skakun, S., Claverie, M., and Dungan, J. 2016. Harmonizing Landsat and Sentinel-2 Reflectances for Better Land Monitoring.

Masek, J. G., Vermote, E. F., Saleous, N. E., Wolfe, R., Hall, F. G., Huemmrich, K. F., Gao, F., Kutler, J., and Lim, T.-K. 2006. A Landsat surface reflectance dataset for North America, 1990-2000. IEEE Geoscience and Remote Sensing Letters, 3(1):68–72.

Mason, P., Zillman, J., Simmons, A., Lindstrom, E., Harrison, D., Dolman, H., Bojinski, S., Fischer, A., Latham, J., and Rasmussen, J. 2010. Implementation plan for the global observing system for climate in support of the UNFCCC (2010 Update).

Matgen, P., Hostache, R., Schumann, G., Pfister, L., Hoffmann, L., and Savenije, H. 2011. Towards an automated SAR-based flood monitoring system: Lessons learned from two case studies. Physics and Chemistry of the Earth, Parts A/B/C, 36(7):241–252.

Matton, N., Canto, G. S., Waldner, F., Valero, S., Morin, D., Inglada, J., Arias, M., Bontemps, S., Koetz, B., and Defourny, P. 2015. An automated method

for annual cropland mapping along the season for various globally-distributed agrosystems using high spatial and temporal resolution time series. Remote Sensing, 7(10):13208–13232.

Maxa, M. and Bolstad, P. 2009. Mapping northern wetlands with high resolution satellite images and LiDAR. Wetlands, 29(1):248–260.

Mayaux, P., Bartholomé, E., Fritz, S., and Belward, A. 2004. A new land-cover map of Africa for the year 2000. Journal of Biogeography, 31(6):861–877.

McCloy, K. R. 2005. *Resource management information systems: Remote sensing, GIS and modelling*. CRC Press.

McFeeters, S. K. 1996. The use of the Normalized Difference Water Index (NDWI) in the delineation of open water features. International Journal of Remote Sensing, 17(7):1425–1432.

McNemar, Q. 1947. Note on the sampling error of the difference between correlated proportions or percentages. Psychometrika, 12(2):153–157.

Milly, P. C. D., Wetherald, R. T., Dunne, K., and Delworth, T. L. 2002. Increasing risk of great floods in a changing climate. Nature, 415(6871):514–517.

Mouw, C. B., Greb, S., Aurin, D., DiGiacomo, P. M., Lee, Z., Twardowski, M., Binding, C., Hu, C., Ma, R., Moore, T., *et al.*. 2015. Aquatic color radiometry remote sensing of coastal and inland waters: Challenges and recommendations for future satellite missions. Remote Sensing of Environment, 160:15–30.

Müller-Wilm, U. 2015. Sentinel-2 MSI-Level-2A Prototype Processor Installation and User Manual. Telespazio VEGA Deutschland GmbH: Darmstadt, Germany.

Muster, S., Heim, B., Abnizova, A., and Boike, J. 2013. Water body distributions across scales: a remote sensing based comparison of three arctic tundra wetlands. Remote Sensing, 5(4):1498–1523.

Nakajima, T., Tao, G., and Yasuoka, Y. 2002. Simulated recovery of information in shadow areas on IKONOS image by combing ALS data. In *Proceeding of Asian Conference on Remote Sensing (ACRS)*.

NASA-JPL. 2014. Wetland Web-site. Global monitoring of wetland extend and dynamics. Available at `http://wetlands.jpl.nasa.gov/science/index.html`, Accessed in 2014.

Nath, R. and Deb, S. 2010. Water-Body Area Extraction From High Resolution Satellite Images-An Introduction, Review, and Comparison. International Journal of Image Processing (IJIP), 3(3):353–372.

Nativi, S., Mazzetti, P., Santoro, M., Papeschi, F., Craglia, M., and Ochiai, O. 2015. Big data challenges in building the global earth observation system of systems. Environmental Modelling & Software, 68:1–26.

OGC, G. D. T. 2015. GDAL - Geospatial Data Abstraction Library.

Oki, T. and Kanae, S. 2006. Global hydrological cycles and world water resources. Science, 313(5790):1068–1072.

Olofsson, P., Foody, G. M., Herold, M., Stehman, S. V., Woodcock, C. E., and Wulder, M. A. 2014. Good practices for estimating area and assessing accuracy of land change. Remote Sensing of Environment, 148:42 – 57.

Oxford Dictionary. 2016. Oxford dictionaries. Language Matters.

Ozdogan, M. and Woodcock, C. E. 2006. Resolution dependent errors in remote sensing of cultivated areas. Remote Sensing of Environment, 103(2):203–217.

Ozesmi, S. L. and Bauer, M. E. 2002. Satellite remote sensing of wetlands. Wetlands Ecology and Management, 10(5):381–402.

Pagnutti, M., Blonski, S., Cramer, M., Helder, D., Holekamp, K., Honkavaara, E., and Ryan, R. 2010. Targets, methods, and sites for assessing the in-flight spatial resolution of electro-optical data products. Canadian Journal of Remote Sensing, 36(5):583–601.

Palmer, S. C., Kutser, T., and Hunter, P. D. 2015. Remote sensing of inland waters: Challenges, progress and future directions. Remote Sensing of Environment, 157:1–8.

Pardo-Pascual, J. E., Almonacid-Caballer, J., Ruiz, L. A., and Palomar-Vázquez, J. 2012. Automatic extraction of shorelines from Landsat TM and ETM+ multi-temporal images with subpixel precision. Remote Sensing of Environment, 123:1–11.

Pekel, J.-F., Vancutsem, C., Bastin, L., Clerici, M., Vanbogaert, E., Bartholomé, E., and Defourny, P. 2014. A near real-time water surface detection method based on HSV transformation of MODIS multi-spectral time series data. Remote Sensing of Environment, 140:704–716.

Pekel, J.-F., Cottam, A., Gorelick, N., and Belward, A. S. 2016. High-resolution mapping of global surface water and its long-term changes. Nature, 540(7633):418–422.

Pettorelli, N., Vik, J. O., Mysterud, A., Gaillard, J.-M., Tucker, C. J., and Stenseth, N. C. 2005. Using the satellite-derived NDVI to assess ecological responses to environmental change. Trends in ecology & evolution, 20(9):503–510.

Pfeffer, W., Arendt, A., Bliss, A., and Bolch, T. 2014. The Randolph Glacier Inventory: a globally complete inventory of glaciers. Journal of Glaciology, 60(221):537–552.

Pitt, A. L., Baldwin, R. F., Lipscomb, D. J., Brown, B. L., Hawley, J. E., Allard-Keese, C. M., and Leonard, P. B. 2012. The missing wetlands: Using local ecological knowledge to find cryptic ecosystems. Biodiversity and Conservation, 21(1):51–63.

Pontius, R. G., Millones, M., Pontius, Robert, Gilmore, J., Millones, M., Pontius, R. G., and Millones, M. 2011. Death to Kappa: birth of quantity disagreement and allocation disagreement for accuracy assessment. International Journal of Remote Sensing, 32(15):4407–4429.

Potapov, P. V., Turubanova, S. a., Hansen, M. C., Adusei, B., Broich, M., Altstatt, A., Mane, L., and Justice, C. O. 2012. Quantifying forest cover loss in Democratic Republic of the Congo, 2000–2010, with Landsat ETM+ data. Remote Sensing of Environment, 122:106–116.

Potes, M., Costa, M. J., and Salgado, R. 2012. Satellite remote sensing of water turbidity in Alqueva reservoir and implications on lake modelling. Hydrology and Earth System Sciences, 16(6):1623–1633.

Price, J. C. 1977. Thermal inertia mapping: a new view of the earth. Journal of Geophysical Research, 82(18):2582–2590.

Prigent, C., Lettenmaier, D. P., Aires, F., and Papa, F. 2015. Toward a High-Resolution Monitoring of Continental Surface Water Extent and Dynamics, at Global Scale: from GIEMS (Global Inundation Extent from Multi-Satellites) to SWOT (Surface Water Ocean Topography). Surveys in Geophysics, pages 1–17.

Pulvirenti, L., Pierdicca, N., Chini, M., and Guerriero, L. 2011. An algorithm for operational flood mapping from Synthetic Aperture Radar (SAR) data based on the fuzzy logic. Natural Hazard and Earth System Sciences.

Radoux, J. and Defourny, P. 2010b. Automated image-to-map discrepancy detection using iterative trimming. Photogrammetric Engineering & Remote Sensing, 76(2):173–181.

Radoux, J., Chomé, G., Jacques, D. C., Waldner, F., Bellemans, N., Matton, N., Lamarche, C., d'Andrimont, R., and Defourny, P. 2016. Sentinel-2's Potential for Sub-Pixel Landscape Feature Detection. Remote Sensing, 8(6):488.

Radoux, J. *et al.*. 2010. *Updating land cover maps by GIS-driven analysis of very high spatial resolution satellite images*. Ph.D. thesis, UCL.

Raptis, V., Vaughan, R., and Wright, G. 2003. The effect of scaling on land cover classification from satellite data. Computers & Geosciences, 29(6):705–714.

Raymond, P. A., Hartmann, J., Lauerwald, R., Sobek, S., McDonald, C., Hoover, M., Butman, D., Striegl, R., Mayorga, E., Humborg, C., *et al.*. 2013. Global carbon dioxide emissions from inland waters. Nature, 503(7476):355–359.

Richards, J. A. 2013. *Remote Sensing Digital Image Analysis*, volume 4. Springer, Berlin Heidelberg, Berlin, Heidelberg.

Ritchie, J. C., Zimba, P. V., and Everitt, J. H. 2003. Remote sensing techniques to assess water quality. Photogrammetric Engineering & Remote Sensing, 69(6):695–704.

Rocchini, D., Balkenhol, N., Carter, G. A., Foody, G. M., Gillespie, T. W., He, K. S., Kark, S., Levin, N., Lucas, K., Luoto, M., Nagendra, H., Oldeland, J., Ricotta, C., Southworth, J., and Neteler, M. 2010. Remotely sensed spectral heterogeneity as a proxy of species diversity: Recent advances and open challenges. Ecological Informatics, 5(5):318–329.

Rodríguez-Cuenca, B. and Alonso, M. 2014. Semi-Automatic Detection of Swimming Pools from Aerial High-Resolution Images and LIDAR Data. Remote Sensing, 6(4):2628–2646.

Ron, M., Julia, B., Raviv, L., Brian, M., Esad, M., Lawrence, O., Pat, S., and Kelly, V. 2015. Landsat-8 Operational Land Imager (OLI) Radiometric Performance On-Orbit. Remote Sensing, 7(2):2208–2237.

Rousseau, C., Radoux, J., De Maet, T., Lamarche, C., Defourny, P., *et al.*. 2015. Snow cover anomalies from 2000 to 2014: highlight of two exceptional years over Europe. In *IGARSS 2015*.

Roy, D. P., Ju, J., Kline, K., Scaramuzza, P. L., Kovalskyy, V., Hansen, M., Loveland, T. R., Vermote, E., and Zhang, C. 2010. Web-enabled Landsat Data (WELD): Landsat ETM+ composited mosaics of the conterminous United States. Remote Sensing of Environment, 114(1):35–49.

Ruiz, C. P. and Lopez, F. A. 2002. Restoring SPOT images using PSF-derived deconvolution filters. International Journal of Remote Sensing, 23(12):2379–2391.

Sakthivel, S. P., Genitha C., H., V. Sivalingam, J., and Shanmugam, S. 2014. Super-resolution mapping of hyperspectral images for estimating the water-spread area of Peechi reservoir, southern India. Journal of Applied Remote Sensing, 8(1):083510.

Sala, O. E., Chapin, F. S., Armesto, J. J., Berlow, E., Bloomfield, J., Dirzo, R., Huber-Sanwald, E., Huenneke, L. F., Jackson, R. B., Kinzig, A., *et al.*. 2000. Global biodiversity scenarios for the year 2100. Science, 287(5459):1770–1774.

Santoro, M. and Wegmuller, U. 2014. Multi-temporal synthetic aperture radar metrics applied to map open water bodies. Selected Topics in Applied Earth Observations and Remote Sensing, IEEE Journal of, 7(8):3225–3238.

Santoro, M., Wegmüller, U., Lamarche, C., Bontemps, S., Defourny, P., and Arino, O. 2015a. Strengths and weaknesses of multi-year Envisat ASAR backscatter measurements to map permanent open water bodies at global scale. Remote Sensing of Environment, 171:185–201.

Sathyendranath, S., Watts, L., Devred, E., Platt, T., Caverhill, C., and Maass, H. 2004. Discrimination of diatoms from other phytoplankton using ocean-colour data. Marine ecology progress series, 272:59–68.

Schowengerdt, A. R. 2007. Remote sensing: Models and methods for image processing. By Elsevier Inc. All rights reserved,, pages p300–304.

Schowengerdt, R. A., Archwamety, C., and Wrigley, R. 1985. Landsat thematic mapper image-derived MTF. Photogrammetric engineering and remote sensing, 51:1395–1406.

Seekell, D. A., Pace, M. L., Tranvik, L. J., and Verpoorter, C. 2013. A fractal-based approach to lake size-distributions. Geophysical Research Letters, 40(3):517–521.

Sethre, P. and Rundquist, B. 2005. Remote detection of prairie pothole ponds in the Devils Lake Basin, North Dakota. GIScience & Remote.

Shahbazi, M., Théau, J., and Ménard, P. 2014. Recent applications of unmanned aerial imagery in natural resource management. GIScience & Remote Sensing, 51(4):339–365.

Shahtahmassebi, A., Yang, N., Wang, K., Moore, N., and Shen, Z. 2013. Review of shadow detection and de-shadowing methods in remote sensing. Chinese Geographical Science, 23(4):403–420.

Shuchman, R. and Leshkevich, G. 2013. Foreword for Special Issue of JGLR on Remote Sensing. Journal of Great Lakes Research, 39:1.

Simis, S. G. H. *et al.*. 2006. Blue-green catastrophe: remote sensing of mass viral lysis of cyanobacteria. Thesis, Vrije University, Amsterdam, Instituut voor Milieuvraagstukken.

Slater, J. A., Garvey, G., Johnston, C., Haase, J., Heady, B., Kroenung, G., and Little, J. 2006. The SRTM data "finishing" process and products. Photogrammetric Engineering & Remote Sensing, 72(3):237–247.

Smets, B., Lacaze, R., Freitas, S., Jann, A., Calvet, J., Camacho, F., Baret, F., Paulik, C., d'Andrimont, R., Tansey, K., *et al.*. 2013. Operating The Copernicus Global Land Service. In *ESA Special Publication*, volume 722, page 66.

Smith, A. R. 1978. Color gamut transform pairs. ACM Siggraph Computer Graphics, 12(3):12–19.

Snyder, W. C., Wan, Z., Zhang, Y., and Feng, Y. Z. 1998. Classification-based emissivity for land surface temperature measurement from space. International Journal of Remote Sensing, 19(14):2753–2774.

SPW. 2006. Service Public Wallonie - PICEA, projet du Gouvernement wallon, Direction Générale de l'Agriculture des Ressources Naturelles et de l'Environnement. GW VIII(Doc.4188 23.11 B.L.).

SPW. 2012. Les subventions agro-environnmentales: vade-mecum. Service public de Wallonie, Direction générale opérationnelle de l'Agriculture des Ressources naturelles et de l'Environnement. Département des Aides Direction des Surfaces agricoles. Available at `http://agriculture.wallonie.be/apps/spip_wolwin/IMG/pdf/Vademecum_MAE_2012_version_13_02_2012.pdf`, Accessed on 2016-03-01.

SPW. 2013. Service Public Wallonnie - Orthophotos 2012-2013 Rapport de production Orthophotos Couleur Numériques d'une Résolution de 25 cm. pages 1–21. Report.

Stadelman, W. 1994. Contaminants of liquid egg products. In *Microbiology of the Avian Egg*, pages 139–151. Springer.

Stendera, S., Adrian, R., Bonada, N., Cañedo-Argüelles, M., Hugueny, B., Januschke, K., Pletterbauer, F., and Hering, D. 2012. Drivers and stressors of freshwater biodiversity patterns across different ecosystems and scales: a review. Hydrobiologia, 696(1):1–28.

Sterckx, S., Knaeps, S., Kratzer, S., and Ruddick, K. 2015. SIMilarity Environment Correction (SIMEC) applied to MERIS data over inland and coastal waters. Remote Sensing of Environment, 157:96–110.

Strahler, A. H., Boschetti, L., Foody, G. M., Friedl, M. A., Hansen, M. C., Herold, M., Mayaux, P., Morisette, J. T., Stehman, S. V., and Woodcock, C. E. 2006. Global land cover validation: Recommendations for evaluation and accuracy assessment of global land cover maps. European Communities, Luxembourg, Volume 51.

Subin, Z. M., Riley, W. J., and Mironov, D. 2012. An improved lake model for climate simulations: model structure, evaluation, and sensitivity analyses in CESM1. Journal of Advances in Modeling Earth Systems, 4(1).

Sun, D., Yu, Y., and Goldberg, M. D. 2011. Deriving water fraction and flood maps from MODIS images using a decision tree approach. IEEE Journal of Selected Topics in Applied Earth Observations and Remote Sensing, 4(4):814–825.

Tan, B., Woodcock, C. E., Hu, J., Zhang, P., Ozdogan, M., Huang, D., Yang, W., Knyazikhin, Y., and Myneni, R. B. 2006. The impact of gridding artifacts on the local spatial properties of MODIS data: Implications for validation, compositing, and band-to-band registration across resolutions. Remote Sensing of Environment, 105(2):98–114.

Teng, W., Loew, E., Ross, D. I., Zsilinszky, V., Lo, C., Philippson, W. R., Philpot, W. D., and Morain, S. A. 1997. Fundamentals of photographic Interpretation. American Society of Photogrammetry, (2 nd):49–116.

Thornton, M., Atkinson, P., and Holland, D. 2006. Sub-pixel mapping of rural land cover objects from fine spatial resolution satellite sensor imagery using super-resolution pixel-swapping. International Journal of Remote Sensing, 27(3):473–491.

Townshend, J. R. and Justice, C. 1986. Analysis of the dynamics of African vegetation using the normalized difference vegetation index. International Journal of Remote Sensing, 7(11):1435–1445.

Tranvik, L. J., Downing, J. A., Cotner, J. B., Loiselle, S. A., Striegl, R. G., Ballatore, T. J., Dillon, P., Finlay, K., Fortino, K., Knoll, L. B., *et al.*. 2009. Lakes and reservoirs as regulators of carbon cycling and climate. Limnology and Oceanography, 54(6part2):2298–2314.

Triggs, B., Mclauchlan, P., Hartley, R., and Fitzgibbon, A. 2000. Bundle Ajustment – A Modern Synthesis. Lecture Notes in Computer ScienceLNCS), 1883:298–372.

Tucker, C. J. 1979. Red and photographic infrared linear combinations for monitoring vegetation. Remote Sensing of Environment, 8(2):127–150.

UNESCO. 2009. World water assessment program 2009: the 3rd United Nations World Water Development Report: water in a changing world (WWDR-3). Report, UNESCO.

Vancutsem, C., Bicheron, P., Cayrol, P., and Defourny, P. 2007a. An assessment of three candidate compositing methods for global MERIS time series. Canadian Journal of Remote Sensing, 33(6):492–502.

Vancutsem, C., Pekel, J. F., Bogaert, P., and Defourny, P. 2007b. Mean Compositing, an alternative strategy for producing temporal syntheses. Concepts and performance assessment for SPOT VEGETATION time series. International Journal of Remote Sensing, 28(22):5123–5141.

Vanhellemont, Q. and Ruddick, K. 2015. Advantages of high quality SWIR bands for ocean colour processing: Examples from Landsat-8. Remote Sensing of Environment, 161:89–106.

Verhegghen, A., Bontemps, S., and Defourny, P. 2014. A global NDVI and EVI reference data set for land-surface phenology using 13 years of daily SPOT-VEGETATION observations. International Journal of Remote Sensing, 35(7):2440–2471.

Verhoeven, J. T. 2014. Wetlands in Europe: Perspectives for restoration of a lost paradise. Ecological Engineering, 66:6–9.

Vermote, E., Justice, C., Claverie, M., and Franch, B. 2016. Preliminary analysis of the performance of the Landsat 8/OLI land surface reflectance product. Remote Sensing of Environment.

Vermote, E. F., El Saleous, N. Z., and Justice, C. O. 2002. Atmospheric correction of MODIS data in the visible to middle infrared: first results. Remote Sensing of Environment, 83(1):97–111.

Verpoorter, C., Kutser, T., Seekell, D. A., and Tranvik, L. J. 2014. A global inventory of lakes based on high-resolution satellite imagery. Geophysical Research Letters, 41(18):6396–6402.

Vörösmarty, C. J., McIntyre, P. B., Gessner, M. O., Dudgeon, D., Prusevich, A., Green, P., Glidden, S., Bunn, S. E., Sullivan, C. A., Liermann, C. R., *et al.*. 2010. Global threats to human water security and river biodiversity. Nature, 467(7315):555–561.

Vörösmarty, C. J., Green, P., Salisbury, J., and Lammers, R. B. 2000. Global Water Resources: Vulnerability from Climate Change and Population Growth. Science, 289(5477):284–288.

Wallin, M., Wiederholm, T., and Johnson, R. 2003. Guidance on establishing reference conditions and ecological status class boundaries for inland surface waters. CIS Working Group, 2(3):93.

Wan, Z., Zhang, Y., Zhang, Q., and Li, Z.-l. 2002. Validation of the land-surface temperature products retrieved from Terra Moderate Resolution Imaging Spectroradiometer data. Remote sensing of Environment, 83(1):163–180.

Wang, M. 2010. Atmospheric correction for remotely-sensed ocean-colour products. Reports and Monographs of the International Ocean-Colour Coordinating Group, International Ocean-Colour Coordinating Group (IOCCG): Dartmouth. 78 pp.

Wenny, B. N., Helder, D., Hong, J., Leigh, L., Thome, K. J., and Reuter, D. 2015. Pre-and post-launch spatial quality of the Landsat 8 Thermal Infrared Sensor. Remote Sensing, 7(2):1962–1980.

Whitcraft, A., Becker-Reshef, I., Killough, B., and Justice, C. 2015. Meeting Earth Observation Requirements for Global Agricultural Monitoring: An Evaluation of the Revisit Capabilities of Current and Planned Moderate Resolution Optical Earth Observing Missions. Remote Sensing, 7(2):1482–1503.

Wolfe, R. E., Roy, D. P., and Vermote, E. 1998. MODIS Land Data Storage, Gridding, and Compositing Methodology: Level 2 Grid. Geoscience and Remote Sensing, IEEE Transactions on, 36:1324–1338.

Woodcock, C. E. and Strahler, A. H. 1987. The factor of scale in remote sensing. Remote sensing of Environment, 21(3):311–332.

Wu, Q., Lane, C., and Liu, H. 2014. An effective method for detecting potential woodland vernal pools using high-resolution LiDAR data and aerial imagery. Remote Sensing, 6(11):11444–11467.

Xie, H., Luo, X., Xu, X., Pan, H., and Tong, X. 2016. Automated Subpixel Surface Water Mapping from Heterogeneous Urban Environments Using Landsat 8 OLI Imagery. Remote Sensing, 8(7):584.

Xu, H. 2006. Modification of normalised difference water index (NDWI) to enhance open water features in remotely sensed imagery. International Journal of Remote Sensing, 27(14):3025–3033.

Yamazaki, D. and Trigg, M. A. 2016. Hydrology: The dynamics of Earth's surface water. Nature, 540(7633):348–349.

Yamazaki, D., Trigg, M. A., and Ikeshima, D. 2015. Development of a global˜ 90m water body map using multi-temporal Landsat images. Remote Sensing of Environment, 171:337–351.

Zhan, Q., Shi, W., and Xiao, Y. 2005. Quantitative analysis of shadow effects in high-resolution images of urban areas. International Archives of Photogrammetry and Remote Sensing, 36(8/W27).

Zhang, J. 2010. Multi-source remote sensing data fusion: status and trends. International Journal of Image and Data Fusion, 1(1):5–24.

Zhou, C., Luo, J., Yang, C., Li, B., Wang, S., *et al.*. 2000. Flood monitoring using multi-temporal AVHRR and RADARSAT imagery. Photogrammetric engineering and remote sensing, 66(5):633–638.

Zhu, X., Chen, J., Gao, F., Chen, X., and Masek, J. G. 2010. An enhanced spatial and temporal adaptive reflectance fusion model for complex heterogeneous regions. Remote Sensing of Environment, 114(11):2610–2623.

Zhu, Z. and Woodcock, C. E. 2012. Object-based cloud and cloud shadow detection in Landsat imagery. Remote Sensing of Environment, 118:83–94.

Zhu, Z., Wang, S., and Woodcock, C. E. 2015. Improvement and expansion of the Fmask algorithm: Cloud, cloud shadow, and snow detection for Landsats 4–7, 8, and Sentinel 2 images. Remote Sensing of Environment, 159:269–277.

List of Publications

Publications in peer-reviewed journals

d'Andrimont, R. and Defourny, P. 2017. Monitoring African water bodies from twice-daily MODIS observation. Under review in *GIScience & Remote Sensing*.

d'Andrimont, R., Marlier, C., and Defourny, P. 2017. Hyperspatial and Multi-Source Water Body Mapping: A Framework to Handle Heterogeneities from Observations and Targets over Large Areas. Remote Sensing, 9(3):211.

Faux, A.-M., Draye, X., Lambert, R., d'Andrimont, R., Raulier, P., and Bertin, P. 2013. The relationship of stem and seed yields to flowering phenology and sex expression in monoecious hemp (Cannabis sativa L.). European Journal of Agronomy, 47:11–22.

Jacques, D. C., Marinho, E., d'Andrimont, R., Waldner, F., Radoux, J., and Defourny, P. 2017. Modeling millet prices in Senegal: a trade flow approach. Under review in Science Advances.

Lamarche, C., Santoro, M., Bontemps, S., d'Andrimont, R., Radoux, J., Giustarini, L., Brockmann, C., Wevers, J., Defourny, P., and Arino, O. 2017. Compilation and Validation of SAR and Optical Data Products for a Complete and Global Map of Inland/Ocean Water Tailored to the Climate Modeling Community. Remote Sensing, 9(1):36.

Radoux, J., Chomé, G., Jacques, D. C., Waldner, F., Bellemans, N., Matton, N., Lamarche, C., d'Andrimont, R., and Defourny, P. 2016. Sentinel-2's Potential for Sub-Pixel Landscape Feature Detection. Remote Sensing, 8(6):488.

Other publications

d'Andrimont, R., Pekel, J.-F., Van Bogaert, E., and Defourny, P. 2010. Monitoring water bodies over whole Africa in near real time: detection algorithms and preliminary results. In *Advances in Quantitative Remote Sensing (RAQRS) 3rd international symposium*.

d'Andrimont, R., Duveiller, G., and Defourny, P. 2011a. Exploring the capacity to grasp multi-annual seasonal variability of winter wheat in Continental Climates with MODIS. In *Analysis of Multi-temporal Remote Sensing Images (Multi-Temp), 2011 6th International Workshop on the*, pages 221–224. IEEE.

d'Andrimont, R., Pekel, J.-F., and Defourny, P. 2011b. Monitoring African surface water dynamic using medium resolution daily data allows anomalies detection in nearly real time. In *Analysis of Multi-temporal Remote Sensing Images (Multi-Temp), 2011 6th International Workshop on the*, pages 241–244. IEEE.

d'Andrimont, R., Bartalev, S., Plotnikov, D., and Defourny, P. 2012a. Annual large-scale winter crops mapping from MERIS in Russia to prepare Sentinel-2. In *Sentinel-2 Preparatory Symposium, 23-23 April 2012- ESA-ESRIN, Frascati (Rome), Italy*.

d'Andrimont, R., Pekel, J.-F., Bartholomé, E., and Defourny, P. 2012b. 8 years water bodies monitoring analysis using MODIS over the African continent. In *EGU General Assembly Conference Abstracts*, volume 14, page 12905.

d'Andrimont, R., Waldner, F., Bartalev, S., Plotnikov, D., Kleschenko, A., Virchenko, O., Roerink, G., de Wit, A., and Defourny, P. 2013. Biophysical variables retrieval over Russian winter wheat fields using medium resolution as a precursor of Sentinel-2. In *ESA Living Planet Symposium 2013, 9 - 13 September, 2013 Edinburgh, United Kingdom*.

d'Andrimont, R., Marlier, C., Defourny, P., *et al.*. 2015a. Annual mapping of water surfaces at 25 cm in a regional monitoring context. In *The 36th International Symposium on Remote Sensing of Environment, Berlin (Germany)*.

d'Andrimont, R., Marlier, C., Defourny, P., *et al.*. 2015b. Annual mapping of water surfaces at submetric resolution in a regional monitoring context. In *Conference Mapping Water Bodies From Space (MWBS) (ESA-Esrin, Frascati,Rome (Italy)*.

Defacqz, O., Defourny, P., Fan, J., Fan, X., and d'Andrimont, R. 2014. NDVI and GAI retrieval during the winter wheat growing season in the North China Plain with remote sensing images. In *Dragon 3 Symposium*.

Jacques, D., Waldner, F., d'Andrimont, R., Radoux, J., *et al.*. 2014. Genesis of millet prices in Senegal: the role of production, markets and their failures. In *Netmob 2015*.

Lacaze, R., Balsamo, G., Baret, F., Andrew, B., Calvet, J.-C., Camacho, F., D'Andrimont, R., Philippe, P., Smets, B., Poilvé, H., *et al.*. 2010. Geoland2-Towards an operational GMES land monitoring core serviceand First results of the biogeophysical parameter core mapping service.

Lacaze, R., Baret, F., Camacho, F., d'Andrimont, R., Freitas, S., Pacholczyk, P., Poilvé, H., Smets, B., Tansey, K., Wagner, W., *et al.*. 2011. geoland2–towards

an operational GMES land monitoring core service: the biogeophysical parameter core mapping service. In *Proceedings of the 34th International Symposium on Remote Sensing of Environment*.

Lacaze, R., Balsamo, G., Baret, F., Calvet, J.-C., Camacho, F., d'Andrimont, R., Coelho y Freitas, S., Kidd, R., Pacholczyk, P., Polivé, H., Smets, B., and Tansey, K. 2012. The GMES Land Monitoring Service: achievements and continuity. In *AGU Fall Meeting Abstracts*, volume 1, page 1100.

Lacaze, R., Smets, B., Baret, F., Weiss, M., Ramon, D., Wandrebeck, L., Montersleet, B., Calvet, J.-C., Roujean, J.-L., Camacho, F., Trigo, I. F., Freitas, S. C., Jann, A., Paulik, C., Tansey, K., d'Andrimont, R., and Verger, A. 2014a. The operational 333M biophysical products of the Copernicus Global Land service. In *The 4th International Symposium on Recent Advances in Quantitative Remote Sensing RAQR'IV*.

Lacaze, R., Smets, B., Trigo, I. F., Freitas, S. C., Jann, A., Calvet, J.-C., Camacho, F., Baret, F., Weiss, M., de Montera, L., Roujean, J.-L., Paulik, C., d'Andrimont, R., Waldner, F., Tansey, K., Pacholczyk, P., Balsamo, G., Bousetta, S., and Sinztai, B. 2014b. Towards an operational production of 300m resolution biophysical products in the Copernicus Global Land Service. In *GV2M: Global Vegetation Monitoring and Modeling*.

Smets, B., Lacaze, R., Freitas, S., Jann, A., Calvet, J., Camacho, F., Baret, F., Paulik, C., d'Andrimont, R., Tansey, K., *et al.*. 2013. Operating The Copernicus Global Land Service. In *ESA Special Publication*, volume 722, page 66.

Waldner, F., d'Andrimont, R., and Defourny, P. 2013. High Resolution Crop Mapping Along The Growing Season: Methodological Developments Towards An Operational Exploitation Of Sentinel-1, 2 And 3. In *ESA Special Publication*, volume 722, page 72.